

11-2021

**PREPARATION AND EVALUATION OF CROCETIN-COATED
BIODEGRADABLE POLYMER ON TOP OF MAGNETITE
NANOPARTICLES FOR THEIR ANTICANCER EFFECTS**

Sulafa Saeed Abdelhalim Ibrahim

Follow this and additional works at: https://scholarworks.uaeu.ac.ae/all_theses

 Part of the [Chemistry Commons](#)

United Arab Emirates University

College of Science

Department of Chemistry

**PREPARATION AND EVALUATION OF CROCETIN-COATED
BIODEGRADABLE POLYMER ON TOP OF MAGNETITE
NANOPARTICLES FOR THEIR ANTICANCER EFFECTS**

Sulafa Saeed Abdelhalim Ibrahim

This thesis is submitted in partial fulfillment of the requirements for the degree of
Master of Science in Chemistry

Under the Supervision of Professor Yaser E. Greish

November 2021

Declaration of Original Work

I, Sulafa Saeed Abdelhalim Ibrahim, the undersigned, a graduate student at the United Arab Emirates University (UAEU), and the author of this thesis entitled "*Preparation and Evaluation of Crocetin-Coated Biodegradable Polymer on Top of Magnetite Nanoparticles for Their Anticancer Effects*" hereby, solemnly declare that this thesis is my own original research work that has been done and prepared by me under the supervision of Professor Yaser E. Greish, in the College of Science at UAEU. This work has not previously been presented or published or formed the basis for the award of any academic degree, diploma, or a similar title at this or any other university. Any materials borrowed from other sources (whether published or unpublished) and relied upon or included in my thesis have been properly cited and acknowledged in accordance with appropriate academic conventions. I further declare that there is no potential conflict of interest with respect to the research, data collection, authorship, presentation, and/or publication of this thesis.

Student's Signature: _____



Date: __07.12.2021__

Copyright © 2021 by Sulafa Saeed Abdelhalim Ibrahim
All Rights Reserved

Advisory Committee

1) Advisor: Yaser E. Greish

Title: Professor

Department of Chemistry

College of Science

2) Co-advisor: Amr Amin

Title: Professor

Department of Biology

College of Science

3) Co-advisor: Soleiman Hisaindee

Title: Associate Professor

Department of Chemistry

College of Science

Approval of the Master Thesis

This Master Thesis is approved by the following Examining Committee Members:

- 1) Advisor (Committee Chair): Yaser E. Greish

Title: Professor

Department of Chemistry

College of Science

Signature 


Date 16/11/2011

- 2) Member (Internal Examiner): Ahmed Al-Shamsi

Title: Assistant Professor

Department of Chemistry

College of Sciences

Signature 

Date 16/11/2021

- 3) Member (External Examiner): Eisa A. Al Matroushi

Title: Associate Professor

Department of Chemical Engineering

American University of Ras Al Khaimah, UAE

Signature 

Date 16/11/2021

This Master Thesis is accepted by:

Dean of the College of Science: Professor Maamar Benkraouda

Signature maamar Benkraouda Date Jan. 28, 2022

Dean of the College of Graduate Studies: Professor Ali Hassan Al-Marzouqi

Signature Ali Hassan Date Jan. 28, 2022

Copy ____ of ____

Abstract

Liver cancer is still one of the leading causes of cancer-related deaths worldwide. This is due to many reasons including lack of effective drugs, late diagnosis of this type of cancer due to the overlapping of symptoms with many other liver diseases, and lack of effective screening tests. Targeted drug delivery systems offer many promising advantages compared to conventional chemotherapy. Targeted delivery will mitigate the bad side effects of chemotherapy such as drug resistance, low therapeutic value since the drug mostly will be administered through an IV affecting healthy and cancer cells alike, and that leads us to an important point that is patient wellbeing and a promise to a kinder treatment with milder side effects. Iron oxide nanoparticles (MNP) are one of the most researched materials in nanoscience. This is due to its unique chemical and physical characteristics including low toxicity, good biodegradability, good colloidal stability, high surface area, and relatively easy, rapid, and inexpensive production. Within a certain size MNP only show a magnetic behavior in the presence of an external magnetic field. To maintain the nanosized structure of MNP a polymeric coat is necessary to keep the nanoparticles dispersed in solution. The polymer functional groups will also serve as a carrier of drug molecules on its surface. Crocetin is an extract of Saffron a well-known spice in the region. Crocetin showed promising anticancer effects in many studies. This work will focus on the design of a drug delivery system constituted of MNPs. Two types of polymeric coatings were tested including chitosan (CS) and polyethylene glycol (PEG) both polymers known for their use in the medical field. Crocetin was added to both PEG-MNPs and CS-MNPs. Both systems were assessed for their physical and chemical properties and their kinetic release of the drug and finally their effect on the HepG2 liver cancer cell line.

Keywords: Magnetite Nanoparticles, Chitosan, PEG, Crocetin.

Title and Abstract (in Arabic)

تحضير وتقييم البوليمر القابل للتحلل الحيوي المغطى بالكروسياتين على الجزء العلوي من الجسيمات النانوية المغناطيسية لتأثيراتها المضادة للسرطان

الملخص

لا يزال سرطان الكبد أحد الأسباب الرئيسية للوفيات المرتبطة بالسرطان في جميع أنحاء العالم. ويرجع ذلك إلى العديد من الأسباب منها نقص الأدوية الفعالة، والتشخيص المتأخر لهذا النوع من السرطان بسبب تداخل الأعراض مع العديد من أمراض الكبد الأخرى، ونقص اختبارات الفحص المبكر الفعالة. توفر أنظمة توصيل الأدوية المستهدفة العديد من المزايا الواعدة مقارنة بالعلاج الكيميائي التقليدي. سيخفف ذلك الآثار الجانبية السيئة للعلاج الكيميائي مثل مقاومة الأدوية، والقيمة العلاجية المنخفضة حيث يتم إعطاء الدواء في الغالب من خلال الوريد الذي يؤثر على الخلايا السليمة والسرطانية على حد سواء، وهذا يقودنا إلى نقطة مهمة وهي رفاهية المريض والوعد إلى علاج ألطف مع آثار جانبية أكثر اعتدالاً. جسيمات النانو لأكسيد الحديد هي واحدة من أكثر المواد التي يتم البحث عنها في علم النانو. ويرجع ذلك إلى خصائصه الكيميائية والفيزيائية الفريدة بما في ذلك السمية المنخفضة وقدرته الجيدة على التحلل البيولوجي، ومساحة السطح العالية، والإنتاج السهل نسبياً والسريع وغير المكلف. ضمن حجم معين، تظهر جسيمات النانو لأكسيد الحديد سلوكاً مغناطيسياً فقط في وجود مجال مغناطيسي خارجي. للحفاظ على الهيكل النانوي للجسيمات من الضروري وجود طبقة بوليمرية للحفاظ على تشتت جسيمات النانو في المحلول. ستعمل مجموعات البوليمر الوظيفية أيضاً كحامل لجزيئات الدواء على سطحه. كروستين هو مستخرج من الزعفران وهو من التوابل المعروفة في منطقتنا. أظهر تأثيرات واعدة مضادة للسرطان في العديد من الدراسات. في هذا العمل، قمنا بتصميم نظام توصيل الأدوية المكون من جسيمات النانو لأكسيد الحديد. اختبرنا نوعين من الطلاءات البوليمرية بما في ذلك الكيتوزان والبولي إيثيلين جلايكول كلاهما من البوليمرات المعروفة للاستخدام في المجال الطبي. تمت إضافة الكروسياتين على سطح كل من البوليمرات ثم تم تقييم كلا النظامين لخصائصهما الفيزيائية والكيميائية وإطلاقهما الحركي للدواء وأخيراً تأثيرهما على خلايا سرطان الكبد.

مفاهيم البحث الرئيسية: الجسيمات النانوية لأكسيد الحديد، كيتوزان، البولي إيثيلين جلايكول، كروسياتين.

Acknowledgments

Special gratitude to my advisor Prof. Yaser E. Garish for his support and patience throughout this journey. Through his guidance, I learned how to appreciate and love chemistry and material science. I learned teamwork and leadership. I truly enjoyed the time I spent in your lab. From the bottom of my heart, I would like to say thank you. Many thanks to Dr. Soleiman Hisaindee and Dr. Hesham Abdelrehim for offering their help and guidance whenever needed. Thank you to Dr. Mohamed Alnaqbi and Ms. Afra al Bloushi our neighboring lab for their generosity and kindness. Thank you to Mr. Bassam Al-Hindawi for being like a caring father figure to all students working in F2. Many thanks to an old friend Badriya Baig and Prof. Amr Amin from the biology department. Thank you to Ms. Khadega Al-Maqdi and Ms. Lamia Ali. Thank you to all the members of the chemistry department that I interacted with professors and lab instructors for being kind and supportive throughout both my Bachelor's and Master's degree.

Special thanks go to my parents, brothers, and sisters who helped me along the way. Thank you to my husband and his family for their patience. Special thanks to my son's second mother Mawada for taking care of him while I was in the lab.

Dedication

To my Mother Rashida and my Son Khalid

Table of Contents

Title	i
Declaration of Original Work	ii
Copyright	ii
Advisory Committee	iv
Approval of the Master Thesis	v
Abstract	vii
Title and Abstract (in Arabic)	viii
Dedication	x
Table of Contents	xi
List of Tables.....	xiii
List of Figures	xiv
List of Abbreviations.....	xvii
Chapter 1: Introduction	1
1.1 Cancer	1
1.1.1 Hepatocellular Carcinoma (HCC).....	2
1.2 Nanoparticles Used for HCC	4
1.2.1 Classification of Nanoparticles Based on their Origin.....	7
1.2.2 Based on their Chemical Composition.....	9
1.3 Magnetite Nanoparticles (MNPs)	13
1.3.1 Synthesis Methods of MNP's.....	14
1.3.2 Unique Properties and Supermagnetization of MNPs	19
1.3.3 Surface Modification of MNP's.....	21
1.3.4 Surface Functionalization for HCC.....	23
1.4. Aim of the Study	25
Chapter 2: Materials and Methods	27
2.1 Pure MNPs	27
2.2 Surface modification of MNPs.....	28
2.2.1 Modification of MNPs with PEG.....	28
2.2.2 Modification of MNPs with Chitosan.....	29
2.3 Functionalization of MNPs with Crocetin	29
2.3.1 Calculation of the Crocetin Loading	30

2.4 Characterization Techniques	31
2.5 Kinetic Release Study of Crocetin	32
2.6 In Vitro Cytotoxicity	32
2.6.1 MTT Assay	33
Chapter 3: Results and Discussion	34
3.1 Characterization of Pure Magnetite NPs	34
3.2 Characterization of Different Surface Coating Materials	40
3.2.1 Characterization of PEG-Coated MNPs	41
3.2.2 Characterization of Chitosan-coated MNPs	51
3.3 Crocetin Loading Characterization	60
3.3.1 Characterization of Cro-Functionalized PEG-Coated MNPs	61
3.3.2 Characterization of Cro-Functionalized CS-Coated MNPs	66
3.4 Kinetic Release Study of Crocetin	70
3.5 Preliminary In-Vitro Cytotoxicity	76
Chapter 4: Conclusion	80
Chapter 5: Future Work and Limitations	81
References	82

List of Tables

Table 1: Loading capacity of Crocetin functionalized PEG-MNPs	65
Table 2: Loading capacity of Crocetin functionalized CS-MNPs	70

List of Figures

Figure 1: The exponential growth of the number of publications addressing HCC and nanoparticles	6
Figure 2: Structure of various types of macromolecular nanoparticles used for HCC treatment	8
Figure 3: The different crystal structures of the different types of iron oxide	14
Figure 4: Illustrates the before and after-effects of an external magnetic field on the bulk magnetite (top), compared to Fe ions (middle), and supermagnetic MNPs (bottom).....	20
Figure 5: Chemical structure of crocin, crocetin, picrocrocin, and safranal	24
Figure 6: Pourbaix diagram showing the phase composition as a function of pH of the aqueous medium.....	35
Figure 7: XRD pattern of the as-prepared magnetite nanoparticles (MNPs).....	37
Figure 8: FTIR spectrum of the as-prepared magnetite nanoparticles (MNPs)	37
Figure 9: TGA thermogram of the as-prepared magnetite nanoparticles (MNPs)	38
Figure 10: TEM micrograph of the as-prepared magnetite nanoparticles (MNPs)	38
Figure 11: Magnetization hysteresis of the as-prepared magnetite nanoparticles (MNPs).....	39
Figure 12: XRD patterns of the PEG-coated MNPs as a function of the concentration of PEG.....	42
Figure 13: FTIR spectra of the PEG-coated MNPs as a function of the concentration of PEG.....	43
Figure 14: TGA thermograms of the PEG-coated MNPs as a function of the concentration of PEG.....	45
Figure 15: TGA thermogram of a pure PEG powder sample	45
Figure 16: A schematic diagram showing the formation of PEG and hydrated layers onto MNPs surfaces	46
Figure 17: The extent of coating of MNPs with PEG as depicted from their TGA thermograms.....	46
Figure 18: TEM micrographs of PEG-coated MNPs as a function of [PEG].....	49
Figure 19: Magnetization hysteresis of the as-prepared PEG-coated MNPs as a function of the concentration of PEG	50
Figure 20: XRD patterns of the chitosan-coated MNPs as a function of the concentration of chitosan.....	52
Figure 21: FTIR spectra of the chitosan-coated MNPs as a function of the concentration of chitosan.....	53
Figure 22: TGA thermograms of the chitosan-coated MNPs as a function of the concentration of chitosan.....	55

Figure 23: TGA thermogram of pure chitosan.....	55
Figure 24: A schematic diagram showing the formation of Chitosan and hydrated layers onto MNPs surfaces	56
Figure 25: The extent of coating of MNPs with CS as depicted from their TGA thermograms	57
Figure 26: TEM micrographs of CS-coated MNPs as a function of [CS]	58
Figure 27: Magnetization hysteresis of the chitosan-coated MNPs as a function of the concentration of chitosan	59
Figure 28: FTIR spectra of the crocetin-functionalized PEG-coated MNPs as a function of the concentration of crocetin.....	63
Figure 29: TGA thermograms of the crocetin-functionalized PEG-coated MNPs as a function of the concentration of crocetin	64
Figure 30: TGA thermograms of pure PEG and pure crocetin	64
Figure 31: Schematic representation of the possible binding mechanism of crocetin to PEG-MNPs.....	65
Figure 32: FTIR spectra of the crocetin-functionalized chitosan-coated MNPs as a function of the concentration of crocetin	67
Figure 33: TGA thermograms of the crocetin-functionalized chitosan-coated MNPs as a function of the concentration of crocetin	68
Figure 34: TGA thermograms of pure chitosan and pure crocetin	68
Figure 35: Schematic representation of the possible binding mechanism of crocetin to Chitosan-MNPs	70
Figure 36: Cumulative release study of crocetin (5x) from crocetin-functionalized PEG-coated MNPs at different pH values	72
Figure 37: Cumulative release study of crocetin (10x) from crocetin-functionalized PEG-coated MNPs at different pH values	72
Figure 38: Cumulative release study of crocetin (20x) from crocetin-functionalized PEG-coated MNPs at different pH values	75
Figure 39: Cumulative release study of crocetin (5x) from crocetin-functionalized chitosan-coated and PEG-coated MNPs at pH 5.6	75
Figure 40: Cumulative release study of crocetin (5x) from crocetin-functionalized chitosan-coated and PEG-coated MNPs at pH 7.0	76
Figure 41: Cell viability of HepG2 cells against pure crocetin as a function of the concentration of crocetin after 24 hours of culture at 37°C	77
Figure 42: Cell viability of HepG2 cells against pure crocetin as a function of the concentration of crocetin after 72 hours of culture at 37°C	78
Figure 43: Cell viability of HepG2 cells against crocetin-functionalized PEG-coated MNPs as a function of the concentration of crocetin after 24 hours of culture at 37°C.....	78

Figure 44: Cell viability of HepG2 cells against crocetin-functionalized PEG-coated MNPs as a function of the concentration of crocetin after 72 hours of culture at 37°C.....	79
--	----

List of Abbreviations

CS	Chitosan
Cro	Crocetin
HCC	Hepatocellular Carcinoma
MNP	Magnetite Nanoparticles
NP	Nanoparticles
PEG	Polyethylene Glycol

Chapter 1: Introduction

1.1 Cancer

Cancer remains a top leading illness to death and a significant obstacle to enhancing life expectancy globally. Based on a study done by the World Health Organization (WHO) in 2019, cancer is in the top two causes of death before the age of 70 years in 112 countries and the top 4 in another 23 countries. While the medical field continues to make advances in other leading causes of death such as stroke and coronary heart diseases leading to a decrease in their mortality rate. The complex nature of cancer compared to other illnesses makes it a leading cause of death in many countries (Sung et al., 2021).

Scientists are still far away from understanding the full nature of cancer tumors and how to effectively cure it. This is due to many difficulties including the lack of effective diagnostic tools, difficulty in targeting cancer stem cells, and drug resistance of cancer cells (Chakraborty & Rahman, 2012). Tumor development and metastasis are closely related to the structure and function of the tumor microenvironment (Yang et al., 2021). By understanding the tumor microenvironment and considering it in the design of diagnostic and treatment methods only then there will be a better chance to find a cure. The tumor microenvironment has more special characteristics than the normal cells (Brigger et al., 2012) A heterogeneous endothelial cells structure is formed in the inner surface of the tumor vasculature due to the chronic wound-healing process that promotes inflammatory conditions, resulting in tumor angiogenesis, and enhanced blood supply to the tumor tissues (Kim et al., 2021). Angiogenesis will result in characteristic tumor vasculature, uneven blood flow distribution, heterogeneous

leakiness, and high interstitial fluid pressure (Liu et al., 2021). Which will lead to elevating the tumor metabolic activity via an increased supply of oxygen and nutrients. Tumor cells induce progression through abnormal metabolic activity, which results in an acidic and hypoxic environment with increased formation of reactive oxygen species (ROS) and reduced glucose concentration (Dudley, 2012; Kim et al., 2021). The hypoxic conditions in the tumor could change the gene expression of tumor cells, thereby increasing cell survival and resistance to apoptosis induction (Wu & Dai, 2017). The permeable leaky tumor vessels and the reduced lymphatic drainage system aid in the accumulation of nanosized drugs. This effect is called the enhanced permeability and retention (EPR) effect (Nakamura et al., 2016). The pore size limit of the tumor bed has been reported to range between 380 and 780 nm (Brigger et al., 2012). The EPR effect is commonly used for delivering nanosized materials ranging from 10–400 nm (Kang et al., 2018).

1.1.1 Hepatocellular Carcinoma (HCC)

Statistics in 2020 show that 75%-85% of primary liver cancer cases are due to Hepatocellular Carcinoma (HCC) (Sung et al., 2021). HCC is characterized by its late appearance, fast progression, limited response to therapy, and a very poor survival rate (6%) (Limeres et al., 2019). Multiple liabilities are known to contribute to HCC. The main risk factors include cirrhosis, chronic infection from both hepatitis B (HBV) and hepatitis C (HCV) virus, toxicity caused by alcohol and aflatoxins exposure, metabolic diseases such as diabetes and obesity, non-alcoholic fatty liver disease, and hereditary hemochromatosis (Baig et al., 2019; Sharma, 2020). Due to the lack of clear symptoms of HCC which often overlaps with other diseases, HCC is diagnosed in late stages (Bialecki & Di Bisceglie, 2005). More than 60% of patients are diagnosed with the

late-stage disease after metastasis has occurred, resulting in an overall 5-year survival rate of less than 16% of the cases. Consequently, patients with advanced HCC are left with palliative care options only. This explains why the number of every year new cases of HCC is very close to its number of annual death cases (Sung et al., 2021).

The treatment options available for HCC is greatly dependent on the stage of the disease and the individual patients' profiles (Baig et al., 2019). Surgical resection, ablation, liver transplantation, embolization methods including bland embolization, transarterial chemoembolization (TACE), chemoembolization with drug-eluting beads (DEBs), and radioembolization, as well radiotherapy, chemotherapy, and combination therapy are the most common treatment options available for HCC (Maluccio & Covey, 2012). These treatments are not feasible in most cases and even when possible, they offer 5 years survival rate at best and a very high chance of HCC recurrence.

Furthermore, in 60% to 80% of patients with liver cancer, the treatment is complicated by underlying liver cirrhosis and hepatic dysfunction (Limeres et al., 2019). Alongside the severe side effects of untargeted therapy attacking healthy and tumor cells alike, growing resistance toward chemotherapy, surgical interventions mistakenly facilitating cancer metastasis and irritating lifelong immunosuppressive therapy due to transplantation are only a few of the setbacks of the current treatment methods (Baig et al., 2019).

If the HCC is diagnosed early, the patient has better survival rates with surgical resection and transplantation as the primary curative treatment technique (Gans et al., 2019). For patients with moderate HCC, the aim is to use all other possible treatment methods to reach the point where surgical removal of the tumor is possible.

For the advanced stage HCC patients, the drug Sorafenib was the first approved US Food and Drug Administration (FDA) for the treatment of HCC. Sorafenib improves the overall survival of advanced HCC for about 3 months. Sorafenib is a small molecule inhibitor of serine-threonine tyrosine protein kinases (Raf-1, B-Raf) involved in the angiogenesis, including vascular endothelial growth factor receptor and platelet-derived growth factor receptor beta (Gans et al., 2019). Sorafenib's anticancer activity works by blocking tumor growth by inhibiting cell proliferation and angiogenesis. Side effects of Sorafenib include hand-foot skin reactions, hypertension, diarrhea, and fatigue (Baig et al., 2019; Gans et al., 2019). Sorafenib is however not beneficial for all patients with advanced HCC. Major tumor regressions are rare, and few patients experience long-term cancer control. Moreover, Sorafenib has not been effective at preventing liver cancer recurrence after TACE or surgical resection. In recent years, the landscape of systematic treatment has changed, with newer agents FDA approved and clinically available. Several multikinase inhibitors (including sunitinib, brivanib, erlotinib, and linifanib) were tested against sorafenib in large randomized clinical trials and failed to prove superior (Gans et al., 2019). The drawbacks of the current treatments call for the need for more innovative and effective treatment methods for HCC treatment and diagnosis.

1.2 Nanoparticles Used for HCC

Nano-drug delivery systems have become a research focus in the field of drug delivery due to the advantages it has over conventional treatment methods (Fang et al., 2020). These advantages include large loading capacity, the ability to protect the payload from degradation, specific targeting, and controlled or sustained release. The nano-drug delivery system can be enhanced by changing its properties such as size,

shape, payload, and surface features for a customized treatment (Nakamura et al., 2016). The newly emerging field of chemotherapeutic engineering, or cancer nanotechnology or nanomedicine not only promises a more effective targeted cancer therapy but also a chance to administrate cancer drugs orally at home (Mei et al., 2013).

There is a growing mass of scientific research linking HCC with nanoparticles Figure 1 (Baig et al., 2019). Despite a growing number of research done on nanomedicine, unmet medical demands in cancer diagnosis and therapy remain substantial (Parvavian et al., 2017). This is due to several factors that hinder the infiltration of the nano-drug delivery system deep into the tumor bed. Despite the EPR effect, only 2 folds of the nano drugs reach the tumor compared with critical normal organs (Nakamura et al., 2016).

Due to the irregular tumor vasculature permeability and hyperperfusion, also the lack of a fluid drainage system that normally regulates fluid balance. This leads the tumor microenvironment to have an increased interstitial fluid pressure and high osmotic pressure that hinders the delivery of nano-drug delivery systems from the bloodstream to the tumor (Nakamura et al., 2016). Furthermore, the high level of abundant extracellular matrix and the substantial stroma cells, like tumor-associated fibroblasts and tumor-associated macrophages, constitute the binding site barrier. The binding site barrier limits deep penetration of nano drugs within the solid tumors, leading most nano-drugs to accumulate and be retained around blood vessels and even unintendedly internalized by stroma cells through an off-targeted effect (Liu et al., 2021)

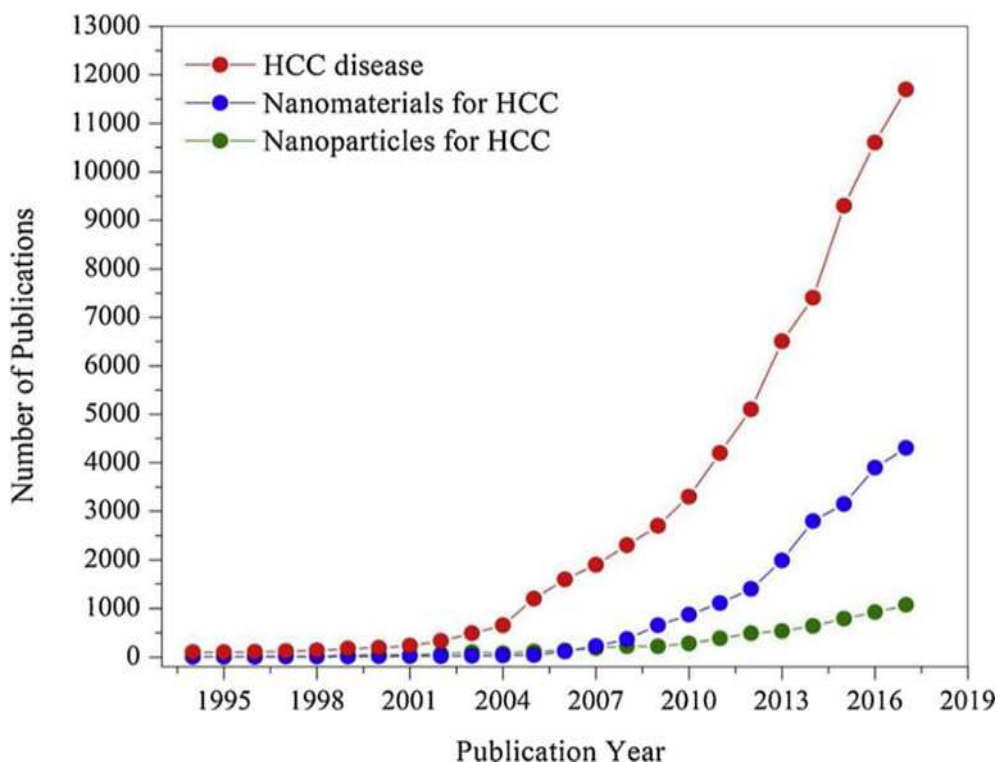


Figure 1: The exponential growth of the number of publications addressing HCC and nanoparticles

That's why to translate the research in nanomedicines into clinical practice successfully, several issues need to be taken under consideration, including the physiological behavior of the NP's drug carrier system with minimal off-target effects, effective clearance from the human organism, and minimal or no toxicity to healthy tissues in living organisms. More specifically, hydrodynamic diameter, surface charge, and hydrophobic/hydrophilic balance are important physicochemical properties that can affect the *in vivo* biodistribution and clearance of administered nanoparticles (Gonzalez-valdivieso et al., 2021; Massaro & Lorenzoni, 2021; Sanna et al., 2014).

1.2.1 Classification of Nanoparticles Based on their Origin

1.2.1.1 Natural Nanoparticles

Nanoparticles from a natural origin will have the advantage of biocompatibility and biodegradability. Two very important characteristics in drug delivery systems. An example of natural polymers is Silk fibroin (SF) is a natural polymer obtained by a variety of species including silkworms (the domesticated silkworm *Bombyxmori*) and spiders (Virilan et al., 2016). Organic polymers such as polysaccharides include dextran, cellulose, Chitin, and chitosan can be extracted from natural sources Figure 2 (Baig et al., 2019). Inorganic nanoparticles are present in nature such as Fe_3O_4 and MnO , but they are polydisperse and lack uniform shape and composition. However, they can be produced naturally with the aid of plants extracts to convert metals from their ionic state to elemental state. This biosynthesis method is frequently used to produce nanoparticles such as Ag, Au, Fe_3O_4 , and ZnO (Griffin et al., 2018). Inorganic nanoparticles used in drug delivery are mostly biocompatible and bioinert.

1.2.1.2 Synthetic (Engineered) Nanoparticles

Synthetic nanoparticles offer the advantage of customizing the properties of the nanoparticles based on the application. They have better-controlled morphology, composition, and size distribution. Synthetic polymers in most cases have better mechanical properties and lower degradation rates compared to natural polymers. Examples of synthetic polymers include poly (ethylene glycol) (PEG), poly (vinyl alcohol) (PVA), and poly (DL-lactic-co-glycolic acid) (PLGA). These synthetic polymers are biodegradable and biocompatible, therefore they are used in drug delivery applications (Rahimi et al., 2021; Shende & Gupta, 2020).

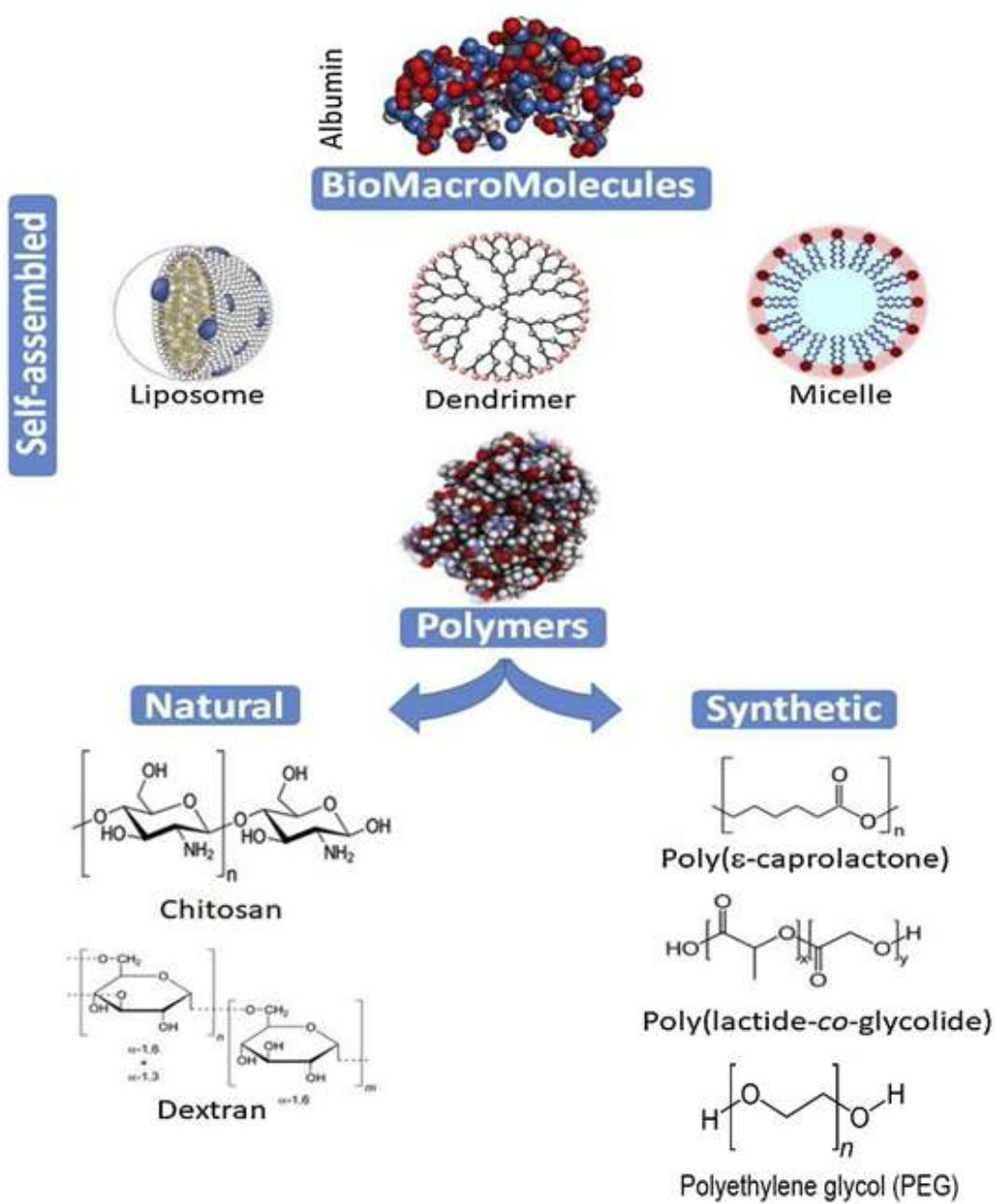


Figure 2: Structure of various types of macromolecular nanoparticles used for HCC treatment

1.2.2 Based on their Chemical Composition

1.2.2.1 Metal and Metal Oxides Nanoparticles

Metal NPs, such as gold, iron, silver, and metal oxides such as TiO₂, Fe₃O₄, Al₂O₃, ZnO, and SiO₂ have been extensively studied due to their special chemical and physical properties compared to their bulk material (Saleh, 2020). These nanoparticles have a high active surface area and are known for their biocompatibility. The surface of these NPs can easily be modified by several methods such as attaching a polymer chain, coupling agent, or doping metal ions (Qi et al., 2019). Using an organic capping agent will offer functional groups on the surface for an opportunity to add multifunctional molecules, such as targeting molecules, therapeutic molecules quantum dots, and dyes. By fine-tuning the NP's preparation method, we can obtain custom-made physical and chemical properties that serve the application well.

Pancreatic cancer progression depends on the nerve microenvironment. Previous research used gold nanoparticles to make nanoclusters for the delivery of siRNA to silence the nerve growth factor (NGF) for the treatment of pancreatic cancer. The gold nanoclusters–siRNA complex (GNC-siRNA) increased the stability of siRNA in serum, prolonged its circulation lifetime in blood, and enhanced the cellular uptake and tumor accumulation of siRNA. Moreover, the GNC–siRNA complex downregulated the NGF expression in Panc-1 cells and pancreatic tumors and effectively inhibited the tumor progression in three pancreatic tumor models without adverse effects (Lei et al., 2017). In another research quercetin, a bioactive flavonoid derived from plant sources was added to zinc-oxide NPs. Zinc oxide- quercetin exhibited excellent anticancer activity against MCF-7 breast cancer cells compared to quercetin and ZnO nanoparticles, which confirms that the solubility and bioavailability

of quercetin have been greatly improved and successfully reached the target site when loaded on ZnO nanoparticles (Sathishkumar et al., 2021).

1.2.2.2 Silica-based Nanoparticles

Crystalline silica NPs were found toxic since they induce chronic obstructive pulmonary disease (Meijer et al., 2001). However amorphous silica is safe and commonly used in biomedical applications and this is what will be described in this section (Baig et al., 2019). Silica is an inert inorganic material that is known to be chemically stable with size-selective porosity and biocompatibility. Silica is hydrophilic material with a silanol (Si-OH) functional group which allows it to disperse well in water or polar solvents. More so, the Si-OH can be modified with other functional groups or provide a binding site for bio-conjugation (Sodipo & Aziz, 2016). The synthesis of Mesoporous silica NPs, to obtain a pore diameter of 2–50 nm, is possible in both basic and acidic media by manipulation of several factors including the concentration, pH of the solution, and the incorporation of hydrophobic compounds (Kumar et al., 2018).

Doxorubicin a well-known anticancer drug has severe side effects related to heart failure and arrhythmia that limit its use. In research done to reduce the side effects of the drug mesoporous silica NPs (MSP) were made and capped with folic acid then loaded with doxorubicin to make a pH-responsive treatment for breast cancer (Tonbul et al., 2021).

1.2.2.3 Polymeric Nanoparticles

Polymeric NPs are widely used in pharmaceutical and medical applications (Saleh, 2020). Polymer-based NPs can be categorized mainly into natural polymers and synthetic polymers. Examples of natural polymers include albumin a natural protein found in abundance in the human body and polysaccharides, such as chitosan, and dextran. The advantage of natural polymers is due to their excellent biocompatibility, biodegradability, and multifunctionality due to the functional groups in their surface (Baig et al., 2019).

Curcumin is known for its anticancer effect but has limited clinical application due to its low solubility in an aqueous medium. In a research done to enhance the solubility of curcumin CCM-loaded human serum albumin (HSA) nanoparticles (CCM-HSA-NPs) were synthesized for intravenous administration using albumin-bound technology. The solubility of curcumin in the nanoparticles was improved 300 times than free curcumin. Furthermore, CCM-HSA-NPs have 14 times better accumulation in tumor cells than free curcumin. In vivo, the nanoparticles showed 66% tumor growth inhibition compared with 18% for free curcumin (Kim et al., 2011). In another research, curcumin was added to dextran nanoparticles for the same reasons of enhancing solubility of Curcumin (Anirudhan & Binusreejayan, 2016).

Synthetic polymeric NPs, which are generally composed of biocompatible and biodegradable polymers. These materials are widely used in drug delivery applications (Saleh, 2020). Examples of synthetic polymers include Poly (hydroxy acids) such as PLGA, PCL, and PHB, as well as their copolymers. They are classified as polyesters with minor variation in their structure but a major difference in their rates of degradation (Baig et al., 2019). In a study aimed to fabricate a NP system composed

of the drug paclitaxel embedded in PLGA and coated with hyaluronic acid (HA-PTX-PLGA) to actively target breast cancer cells. The NP's system showed a controlled release and enhanced drug cytotoxicity (Cerqueira et al., 2017).

1.2.2.4 Lipid-based Nanoparticles

Lipid-based nanoparticles including liposomes and micelles have valuable properties, such as physical and chemical stability, site-specific targeting, low cost, lack of toxicity, and the possible control of both hydrophilic and hydrophobic molecules (Magesh et al., 2006; Sonju et al., 2021). Liposomes are constituted from cholesterol and phospholipids compounds with a size range of 50–100 nm. These are suitable for drug delivery, especially for cytotoxic drugs, due to their reduced toxicity and enhanced bioavailability (Mei et al., 2013; Saleh, 2020). In a study where 5-Fluorouracil (5FU) a known anticancer drug is encapsulated inside the liposomal NPs and targeted with folic acid. The targeted liposomes exhibited higher cytotoxicity than the free drug (Handali et al., 2018).

Micelles belong to the amphiphilic colloidal family with a size range within 5–100 nm. Hydrophilic and hydrophobic groups are the two well-defined building blocks of the amphiphilic/lipid molecules that form the micelles. Both groups display the complete opposite polarities hence exhibiting the opposite affinities toward a given solvent. The hydrophobic interior of micelles protects against drug degradation, and the hydrophilic exterior prevents its elimination by the immune system. Micellar carriers are considered as potential materials for enhancing the solubility of lipophilic moieties with increased circulation time in the body (Baig et al., 2019; Capek, 2019). To overcome the poor aqueous solubility of 3,4-Difluorobenzylidene curcumin (CDF), self-assembling nano-micelles of amphiphilic styrene-maleic acid copolymer (SMA)

with CDF by non-covalent hydrophobic interactions were made for the treatment of pancreatic cancer. The nano-micelles possess a favorable size and surface characteristics promoting efficient intracellular trafficking, yielding pronounced antitumor response in pancreatic cancer cells in vitro (Kesharwani et al., 2015).

1.3 Magnetite Nanoparticles (MNPs)

MNPs (Fe_3O_4) a type of iron oxides nanoparticles have attracted researchers from different fields such as biology, medicine, and physics, due to their multifunctional properties such as small size hence high surface area, superparamagnetism, and low toxicity (Majidi et al., 2016). Especially in biomedical applications, MNPs have been extensively utilized for different applications, including molecular imaging, hyperthermia, cell/protein separation, drug/gene delivery, tissue repair, and stem cell tracking (Trabulo et al., 2017). There are three main types of iron oxides they are maghemite ($\gamma\text{-Fe}_2\text{O}_3$), hematite ($\alpha\text{-Fe}_2\text{O}_3$), and magnetite (Fe_3O_4) (Samrot et al., 2021). The three have different crystal structures presented in Figure 3 and as a result, they also have different magnetic properties (Kuchma et al., 2018). Magnetite the focus of this thesis exhibits the strongest magnetism among all the transition metal oxide (Teja & Koh, 2009). When oxidized magnetite turns to maghemite and if maghemite is further oxidized hematite is formed.

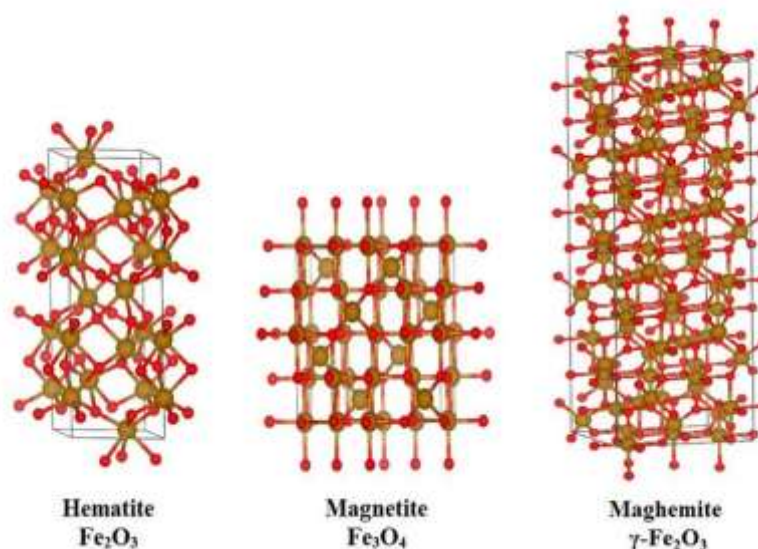


Figure 3: The different crystal structures of the different types of iron oxide

1.3.1 Synthesis Methods of MNP's

MNPs can be synthesized by different methods including physical, chemical, and biological methods. The choice of method of synthesis helps in producing MNPs of the desired shape, size, structure, colloidal stability, and magnetic properties (Samrot et al., 2021). The physical methods follow the top-down synthesis approach. Starting from a large unit, into smaller units and then these units are converted into suitable in size MNPs (Khan et al., 2019). Physical methods include gas phase deposition, electron beam lithography, Pulsed laser ablation, Laser-induced pyrolysis, power ball milling, and combustion (Samrot et al., 2021). Both biological and chemical methods follow the bottom-up approach where MNPs are formed from relatively simpler substances (Khan et al., 2019). Biological methods are mediated by the use of biological entities such as bacteria, fungi, plant extracts, and proteins. Although biological methods are more environmentally friendly, the particles produced might be less stable, non-uniform with less homogeneity, and more agglomeration (Samrot

et al., 2021). Among all the synthesis methods, chemical methods are the most utilized due to their relative simplicity. For that reason, the most common chemical methods will be viewed in more detail.

1.3.1.1 Chemical Co-Precipitation

In this method, MNPs are prepared from aqueous salt solutions, by the addition of a base under an inert atmosphere at room temperatures or high temperatures (Ferreira et al., 2016). The reaction is simply as presented in Equation 1:



Several factors will dictate the size and morphology of the MNP's formed. These factors include the type of salts used, such as chlorides, sulfates, nitrates, perchlorates, etc., the ratio of ferric to ferrous ions, the PH value, the reaction temperature, the ionic strength of the media, and the other reaction parameters (such as stirring rate and dropping speed of basic solution). The pH ranging between 8 and 14 is the expected range for complete precipitation with a stoichiometric ratio of 2/1 ($\text{Fe}^{3+}/\text{Fe}^{2+}$) (Majidi et al., 2016). Pourbaix diagram aid in the understanding of the electrochemical stability of iron oxide NPs as a function of the pH of the solution (Fu et al., 2021). In a paper by Sun and his team, they prepared supermagnetic iron oxide nanoparticles by mixing 1:1.75 ferrous to ferric ions at 80°C and under inert conditions. Using ammonia solution, the pH of the solution was brought up to above 10. After 1-hour oleic acid was added and the solution was left to stir for another 3 hours. The MNPs had a size of 12 nm and the oleic acid – MNPS had a hydrodynamic size of around 100nm (Sun et al., 2014). In another research, iron oxide nanoparticles were prepared by adding drop-wise sodium hydroxide to a mixture of 1:2 ferrous to

ferric iron ions under vigorous stirring at 2000 rpm. The obtained MNP has a size of 11 nm and exhibited supermagnetization (Nkurikiyimfura et al., 2020).

1.3.1.2 Thermal Decomposition

Highly monodispersed MNPs with controlled size and high crystallinity can be achieved by high-temperature decomposition of organometallic iron precursors in high boiling organic solvent and the presence of various stabilizing surfactants. The temperature of the reaction ranges from 100-320°C. Examples of iron precursors are acetylacetonates, acetates, oleates, carbonyl, oxalates, or ferrocene, for the boiling organic solvent benzyl ether or octadecene are usually used. The surfactants include alcohol, oleic acid, and organic amines, they play an important role in the size and monodispersity of the produced MNPs. The size of the nanoparticles can be controlled by adjusting the temperature and the duration of the reaction (Majidi et al., 2016; Pang et al., 2016). The thermal decomposition of the precursor can either be done in a solvent or solvent-free environment. However, due to the limitation of most of the surfactant's boiling temperature, there is a disadvantage to going with a solvent-free environment leading to a difficulty to control and adjust the particles' size. To have control over the size, size distribution, and magnetic properties of the synthesized iron oxide nanoparticles via thermal decomposition, the right selection of the precursor and surfactant chemical nature, the ratio of iron precursor to surfactant, and reaction time will play an important role (Sodipo & Aziz, 2016).

$\text{Fe}(\text{acac})_3$ was used as the starting material at a constant concentration. Different heating rates and different solvents were used to study the effect on the MNP's size formed. The produced MNP's had a size from 7 to 12 nm, where the heat of the reaction was the main factor to control the size (Jović Orsini et al., 2018). In

another research paper zinc doped magnetite was prepared via thermal decomposition of zinc and iron acetylacetonates in the presence of oleic acid and oleylamine. The temperature used was in the range of 200-290°C producing surfactant-coated MNPs with narrow size distribution and the mean diameter of 15 nm (Kubíčková et al., 2020).

1.3.1.3 Microemulsions

The water-in-oil (W/O) microemulsion has been widely used to synthesize uniform-sized MNPs. This method is composed of three components: water, oil, and an amphiphilic surfactant molecule. Together they form a single-phase isotropic system that is thermodynamically stable. The surfactant molecule lowers the interfacial tension between water and oil resulting in the formation of a transparent solution. The water nanodroplets contain reagents, as a nanoreactor. Undergo rapid coalescence allowing for mixing, precipitation reaction, and aggregation processes for the synthesis of MNPs. The shape of the water pool is spherical, and the surfactant molecules surround the nanodroplet wall forming a cage-like structure to allow the growth of the particles within. As a result, the NP's formed to have a controlled size and average size during the collision and aggregation process. Thus, the size of the spherical nanoparticles can be controlled by changing the size of the water pool. Generally, the higher the water-to-surfactant molar ratio the larger is the particle size (Faraji et al., 2010; Wongwailikhit & Horwongsakul, 2011).

In a previous study, iron oxide nanoparticles were prepared from ferrous chloride salt. Hexadecyltrimethyl ammonium bromide (HTAB) was dissolved in n-Octane and mixed first 1-butanol then ferrous chloride aqueous solution to make the first microemulsion. The second emulsion was made the same way but with sodium hydroxide instead of an iron solution. MNPs with a size below 10 nm are formed when

the two microemulsions are mixed (Chin & Yaacob, 2007). In another research, Fe/Fe₃O₄ core-shell nanoparticles were synthesized through the reduction of aqueous FeCl₃ by aqueous NaBH₄ via a combination of two water-in-oil microemulsion solutions. Each microemulsion solution contains cetyl trimethyl ammonium bromide (CTAB) as a surfactant and n-butanol as a co-surfactant. The oil phase contains n-octane, and the water phase mentioned earlier. They produced iron-MNP that had a size range from 8-20nm based on the O/W ratio. Particle size decreases with increasing O/W ratio (Zhang et al., 2010).

1.3.1.4 Hydrothermal Synthesis

The hydrothermal synthesis of MNP results in better crystallinity than the other methods. These reactions are performed in an aqueous media in reactors or autoclaves where the pressure can be higher than 2000 psi and temperatures higher than 200°C (Faraji et al., 2010). This technique can be processed through either hydrolysis and oxidation or neutralization of mixed metal hydroxides which can lead to ferrite formation. Synthesis of iron oxide by hydrolysis and oxidation of ferrous salts in an aqueous medium is more ordinary and common. During this process, parameters as temperature, solvent, and reaction time normally play key roles in the formation of final products. For instance, larger sizes of Fe₃O₄ particles were produced when higher water content exists in the reaction set up. In the hydrothermal procedure, the particle size can be controlled mostly by the rate of nucleation vs. crystal growth. These rates are based upon the reaction temperature while other conditions are kept constant. If the nucleation rate is faster than grain growth at higher temperatures, it causes a reduction in particle size. However, prolonging the reaction time would favor grain growth (Ramimoghadam et al., 2014).

In a study MNPs coated with tartaric acid and/or ascorbic acid were prepared by hydrothermal process. Briefly, ammonia solution was added to ferric and ferrous chloride solution mixture (1:1). Then surfactant is added to the previous reaction mixture and then transferred to Teflon-sealed autoclave at 160°C. This method resulted in MNPs with a size of around 8 nm (Köçkar et al., 2019). In another research surface-modified, MNPs were synthesized in an aqueous phase by heating an aqueous solution of either n-decanoic acid or n-decylamine with iron sulfate at 245°C. At high temperatures the miscibility of both n-decanoic acid or n-decylamine improved in response to the decrease of the dielectric constant of water as a result the formed MNPs were capped with either organic coatings resulting in better dispersity. The average size of the particles was 28 nm for n-decanoic-MNPs and 21 nm for n-decylamine-MNPs (Takami et al., 2007).

1.3.2 Unique Properties and Supermagnetization of MNPs

Superparamagnetic Iron Oxide Nanoparticles (SPIONs) are usually crystalline in nature. Those nanoparticles only show a magnetic behavior in the presence of an external magnetic field and return to the unmagnetized condition when the external magnetic field is removed. This phenomenon is called superparamagnetism and it's one of the qualities that make MNPs promising to be used in biological systems. This phenomenon is illustrated in Figure 4 (Samrot et al., 2021; Stephen et al., 2011). MNPs can be guided by an external magnetic field to be absorbed to an organ, tissue, or tumor for targeted therapy or can be heated by an alternating magnetic field for use in hyperthermia and capable of magnetic resonance imaging (MRI) (Majidi et al., 2016). It's true that iron in its pure metal form poses higher magnetization than iron oxide but it's also very sensitive in that form to oxidization and has high characteristic toxicity.

However, iron oxides are less sensitive to oxidation and less toxic with a more stable magnetic response (Pang et al., 2016). Other unique characteristics of MNPs include their low toxicity, good biodegradability, good colloidal stability, high surface area, and relatively easy, rapid, and inexpensive production (Arachchige et al., 2017; Trabulo et al., 2017).

Another important property is dispersion, as the naked nanoparticles have a larger surface to volume ratio they get easily oxidized and form aggregates in the aqueous system (Samrot et al., 2021). MNPs tend to self-aggregate and form large agglomerates due to their dipole-dipole attraction. These large agglomerates have their own net polarization/dipole without an external magnetic field. This means that aggregated MNPs lose their superparamagnetism. The nanosized dimensions also increase the chemical reactivity of these particles, resulting in much faster degradation in biological systems. This lack of stability tends to restrict the application of bare MNPs in biomedical applications (Ferreira et al., 2016; Ramimoghdam et al., 2014).

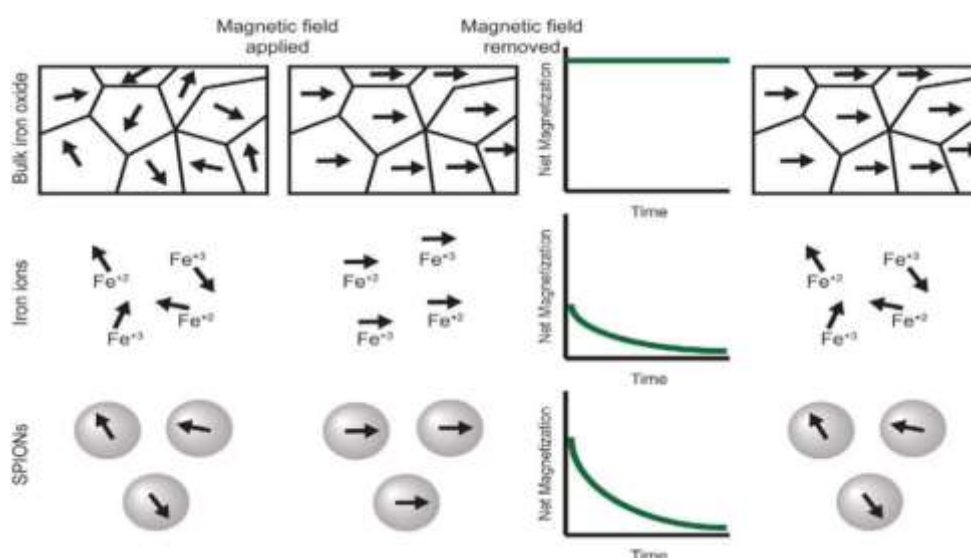


Figure 4: Illustrates the before and after-effects of an external magnetic field on the bulk magnetite (top), compared to Fe ions (middle), and supermagnetic MNPs (bottom).

1.3.3 Surface Modification of MNP's

Colloidal stability refers to the ability to resist clumping/agglomeration and remain monodispersed in a suspension/solution as a colloid (Samrot et al., 2021). To prevent the agglomeration of MNP's, the surface of the nanoparticles must be modified with biopolymers, ligands, or surfactants (Li et al., 2017). The coating must be biodegradable and biocompatible to be used in medical applications (Zhao et al., 2009). The coating gives many advantages such as an increase in the colloidal stability of the MNPs system, reduce the size of MNPs as a result of reducing the agglomeration, reducing the toxicity of MNPs, offering binding sites for further functionalization with a therapeutic molecule or/and targeting ligand, controlling the surface charge and solubility (Moros et al., 2012; Ramimoghadam et al., 2014). Furthermore, the coated MNPs demonstrate better conjugation/interaction with other bioactive molecules compared to bare NPs (Dyawanapelly et al., 2017).

1.3.3.1 PEG

PEG, is a long linear or branched polymeric chain of polyether terminated with hydroxyl groups known as polyethylene oxide or polyoxyethylene, depending on its molecular weight. It is widely used for biomedical applications as a surface coating material for NPs due to its biocompatibility and ability to reduce nonspecific protein adsorption and clearance by RES macrophages (Sarkar et al., 2016). This is because a dense layer of PEG gives hydrophilicity to the surface of MNPs, which gives the NP's better water dispersity and steric stability than in bare MNPs. In addition, functionalized PEG would provide the functional groups for conjugation with a targeting ligand (Moros et al., 2012; Yallapu et al., 2010). Furthermore, the use of PEG during the synthesis of MNPs provides stability between the particles via steric

repulsion (Park et al., 2014). This will prevent the unnecessary agglomeration observed with bare MNPs, subsequently smaller particles size of MNPs with better dispersion will be obtained. A research study was done to fabricate PEG-coated MNPs as contrast agents for real-time long-lasting monitoring of the tumor evolution. The stability of such MNPs system is key for the extended application time. This was achieved by optimizing the suitable molecular weight of PEG, and by studying the biocompatibility of the fabricated PEG-MNPs in vivo and in-vitro (Lazaro-Carrillo et al., 2020).

1.3.3.2 Chitosan

Chitosan is a naturally occurring polysaccharide biomolecule (Han et al., 2020). This biopolymer is an alkaline deacetylated product of chitin, which is derived from the exoskeleton of crustaceans. It is non-toxic, hydrophilic, biocompatible, biodegradable, and antibacterial. It has several applications in medicine; one of the most important is the controlled release of drugs (Escobar Zapata et al., 2012). Chitosan is polycationic with several functional groups that serve as binding sites including amino ($-NH_2$), primary and secondary hydroxyl ($-OH$) groups (Khmara et al., 2020). In a research study, chitosan-coated MNPs and loaded with methotrexate an anticancer drug was made to improve the drug delivery system and targeting agent to treat human breast cancer MCF-7 cell line. The synthesized system with the drug had a size of 150 nm and a drug loading of 74.15%. The drug delivery system has an increased efficacy of 5 times the free drug when tested in vitro (Ali et al., 2018).

1.3.4 Surface Functionalization for HCC

Surface functionalization of the outer layer of the MNPs system will depend on the purpose of the designed nano-carrier system. Different molecules that serve different purposes can be added including targeting agents, tracking molecules, peptides, DNA molecules, chemotherapeutic, radioactive, and hyperthermic drugs (Mahmoudi et al., 2011). By incorporating different functioning molecules, we design a multifunctional delivery system.

1.3.4.1 Crocetin

Growing numbers of research are being done on the therapeutic effects of natural herbs because of their low or no toxicity (Li et al., 2015). *Crocus sativus* L. (*C. sativus*), is a plant commonly known as Saffron, a well-known spice that grows in mild to dry climates and is cultivated in various places around the world such as Switzerland, Morocco, India, and Australia. Saffron is mostly used as a food additive or food colorant, perfume ingredient and it has many applications in traditional medicine for the treatment of various diseases such as respiratory and gastrointestinal diseases (Boskabady & Farkhondeh, 2016). There are four main biologically active components that studies showed possess anticancer (Tseng et al., 1995), anti-microbial (Yousefi et al., 2014), antimutagenic (Bhandari, 2015), and anti-genotoxic properties (Premkumar et al., 2006). Those biologically active components are crocin, crocetin, picrocrocin (responsible for the taste), and Safranal (responsible for the aroma of saffron). Figure 5, shows the chemical structure of the four compounds (Samarghandian & Borji, 2014). Crocin is a mono-glycosyl or di-glycosyl polyene ester and Crocetin that is a dicarboxylic acid precursor of crocin, both are carotenoids responsible for the pigment of saffron (Melnik et al., 2010). Although crocin and

crocetin are structurally related, the difference in the end groups makes crocetin more soluble than crocetin. Moreover, in a study comparing the cytotoxic effect of crocetin and crocetin on five human cancer lines (A549, HepG2, HCT-116, SK-OV-3, and HeLa cells), crocetin had a 5 to 18 folds' higher cytotoxicity than crocetin. It was attributed due to the larger number of productions of oxygen reactive species produced by crocetin than crocetin. This indicates that although the two are structurally related and similar they have different mechanisms for their cytotoxic effect (S. H. Kim et al., 2014).

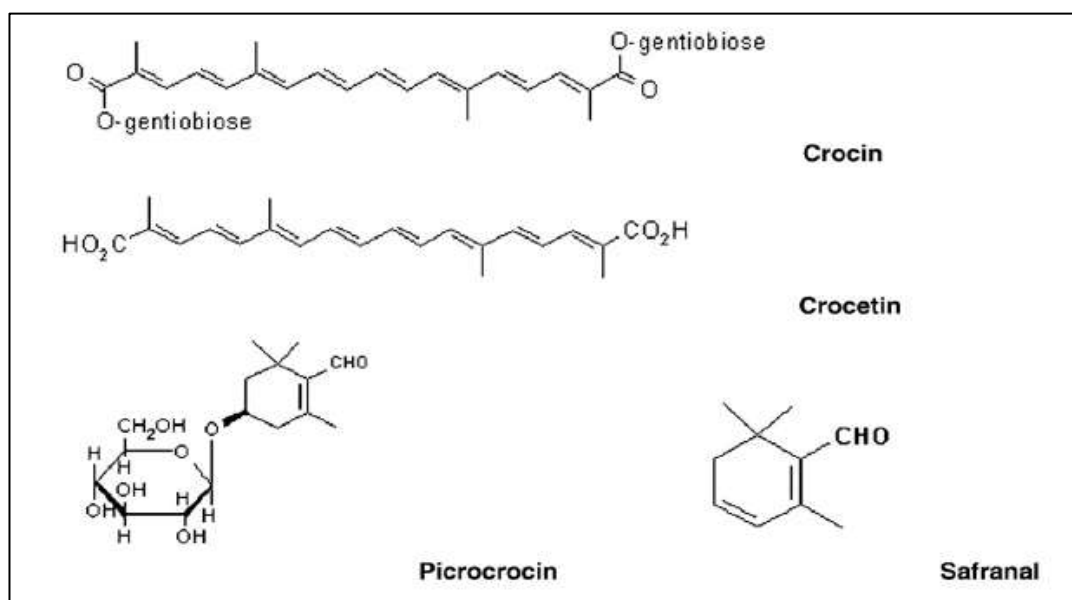


Figure 5: Chemical structure of crocin, crocetin, picrocrocin, and safranal

In another study looking at the anticancer effect of crocetin on human esophageal squamous cell carcinoma KYSE-150 cells. They found that crocetin affected the cell proliferation, migration, and induced apoptosis of the cell line (Li et al., 2015). In another study the effect of crocetin against induced lung cancer in mice model in pre-initiation and post-initiation periods, the study showed a strong antitumor activity against lung cancer proven by the levels of lipid peroxide (LPO) and marker enzymes that were considerably high in cancer-affected mice and returned to normal

rates after treatment with crocetin (Magesh et al., 2006). In a study done on cervical cancer cell line HeLa, non-small cell lung cancer cell line A549 and ovarian cancer cell line SKOV3 treated with crocetin alone (60-40 $\mu\text{mol/L}$ for 48 h) to study its cytotoxic effect and with crocetin (60 $\mu\text{mol/L}$) combined with vincristine a chemotherapeutic drug to see its synergistic effect. It was found that treatment with crocetin in the three types of cancer cell lines inhibited cancer proliferation depending on the concentration of crocetin. Crocetin concentrations from 120 to 240 $\mu\text{mol/L}$ caused cytotoxicity in the three lines by enhancing apoptosis depending on the time of exposure. When crocetin (60 $\mu\text{mol/L}$) was introduced with vincristine the treatment showed a significantly enhanced cytotoxic effect in all the three cell lines than by vincristine alone (Zhong et al., 2011). Furthermore, a study was done on sarcoma 180 tumor-bearing mice to test the effect of cyclophosphamide (CX) a chemotherapeutic drug used to treat several cancers. The long-term use of CX can cause bladder cancer. Crocetin was used to test for any chemo-protective properties that will reduce the undesirable toxic effect of the drug. It was shown that crocetin can ameliorate the urotoxic outcome of CX without compromising its therapeutic effect (Nair et al., 1993). All these studies suggest that crocetin might be a promising candidate as an anticancer agent to fight HCC.

1.4. Aim of the Study

Many studies show the effect of crocetin against different types of cancer models including HepG2 liver cancer cells. Magnetite nanoparticles have many applications in cancer therapy, including hyperthermia, MRI, and growing research for its use in targeted therapy. By functionalizing MNPs surface with crocetin with the aid of organic coating in the middle, we overcome many challenges facing

current chemotherapeutic drugs. MNPs targeted therapy will give crocetin a longer circulation time, higher concentration of the drug to land in the tumor environment, less contact of the drug with healthy cells which all leads to better therapeutic effect compared to free crocetin.

The current study aims at the development of crocetin-coated functionalized magnetite (Fe_3O_4) nanoparticles for the evaluation of their efficiency towards hepatic cancer cells in vitro. The main objectives of this study are summarized in the following points:

1. Prepare monodispersed magnetite nanoparticles and evaluate their composition, morphology, and particle size distribution.
2. Coat MNPs with two organic coatings, polyethylene glycol (PEG) and Chitosan.
3. Characterize the functionalized nanoparticles in terms of their composition, particle size distribution, and morphology.
4. Optimize the process of decorating the polymer-coated magnetite NPs with crocetin.
5. Evaluate the crocetin-decorated magnetite NPs for their kinetic release and towards hepatic cells in vitro.

Chapter 2: Materials and Methods

2.1 Pure MNPs

Chemicals used to prepare pure MNPs included iron (II) chloride tetrahydrate ($\text{FeCl}_2 \cdot 4\text{H}_2\text{O}$), iron (III) chloride (FeCl_3), sodium hydroxide (NaOH), and ammonia solution (NH_4OH). All reagents were analytical-grade and were purchased from Sigma-Aldrich (USA). Aqueous solutions of 0.3 M ferrous and 0.6 M of ferric (1:2 ratio) were separately prepared by dissolving the respective amounts of $\text{FeCl}_2 \cdot 4\text{H}_2\text{O}$ and FeCl_3 in de-ionized water.

The following revised preparation procedure was carried out (El-Kharrag et al., 2017). A 5 M aqueous solution of sodium hydroxide was prepared by dissolving the equivalent amount of NaOH in de-ionized water. A 50 ml aqueous NaOH solution was heated at 60°C . A mixture containing equal volumes of Fe^{2+} (0.3 M) and Fe^{3+} (0.6 M) was injected into the NaOH solution at a feeding rate of 40 ml/hr using a syringe pump with vigorous stirring. A brownish-black precipitate representing the magnetite phase was formed. The whole solution was vigorously stirred for 60 minutes at a constant temperature of 60°C . The ferrofluid was then centrifuged at 3000 rpm for 15 minutes following that a successive decantation/washing with 25% ammonia solution 3 times to maintain high basic conditions. After final decantation, MNPs deposits were collected and dried at 60°C for 24 hrs. Dried powders were finely ground to be characterized for their composition, morphology, thermal and magnetic properties.

2.2 Surface modification of MNPs

The surfaces of MNPs were modified by applying organic coatings onto their surfaces. Two types of biocompatible organic coatings were considered: poly(ethylene glycol) (PEG), with a molecular weight of 3350 Da, and chitosan (CS), with a molecular weight range of 50,000-190,000 Da, as per the manufacturer's data sheet. Both chemicals were obtained as high purity (> 99.9%) from Sigma-Aldrich (USA). In the following section, the method of applying each of the coatings will be explained.

2.2.1 Modification of MNPs with PEG

To prepare PEG-coated MNPs, MNPs were first prepared as mentioned in the previous section. After MNPs are formed and left to stir for 60 minutes at 60°C. The product was then centrifuged for 15 minutes and washed 3 times with deionized water. MNPs were then re-suspended in 50 ml deionized water and left under sonication for 90 minutes. Separately different amounts of PEG (1 g, 2 g, 3 g, 4 g, 6 g, 8 g & 12 g) were dissolved in 15 ml DW. These amounts represent weight percentages of 1.5, 3.0, 4.5, 6.2, 9.0, 12.0 and 18.5%, respectively. The PEG solution was then added to the suspended ferrofluid and left to stir overnight with an overhead mechanical stirrer. The PEG-coated MNPs were washed 3 times using the centrifuge and Ethanol and De ionized Water (50:50) mixture. The PEG-MNPs were then dried in the oven at 60°C overnight. The final product was then grounded to a fine powder for further characterization for its composition, morphology, thermal and magnetic properties.

2.2.2 Modification of MNPs with Chitosan

To prepare chitosan-coated MNPs, chitosan solutions containing 0.1, 0.5, 0.7, and 1.0% by weight were prepared by dissolving the corresponding weight of chitosan in a 0.2% acetic acid solution. An equal volume of each of the chitosan solutions (around 50 ml) was vigorously blended with 0.3 M of Fe^{2+} and 0.6 M of Fe^{3+} solutions and then injected into 5 M NaOH solution at a feeding rate of 40 ml/hr at 60°C in a normal atmosphere. At the end of the addition, a brownish precipitate was formed. The whole solution was vigorously stirred at a constant temperature of 60°C for 1hr. Suspensions of chitosan-coated MNPs were then left to cool to room temperature. The suspension was then decanted and centrifuged at 3000 rpm for 15 minutes followed by a successive decantation/washing with deionized water 3 times. After washing out the un-attached chitosan, samples were dried in the oven at 60°C for 24 hrs. Completely dried powders were finely ground and characterized for their composition, morphology, thermal and magnetic properties.

2.3 Functionalization of MNPs with Crocetin

Based on the characterization of the structure, morphology, thermal and magnetic properties of the PEG- and CS-coated MNPs, optimum coating conditions were selected for further functionalization by crocetin (Fisher Scientific, Finland). The amount of crocetin added depended on the available binding sites on the surface of the polymeric coating. Based on that, 1-ethyl-3-(3-dimethylaminopropyl) carbodiimide hydrochloride (EDCI.HCl) (Sigma-Aldrich, USA) was added as a linker and crocetin in excess of 5, 10, and 20 times the available binding sites of both PEG and CS. First EDC was added to crocetin dissolved in 1 ml dimethyl sulfoxide (DMSO) (Sigma-Aldrich, USA) and left to stir for 30 minutes in a dark closed environment. Then a pre-

calculated amount of PEG- or CS-coated MNPs was added and left to stir overnight. Then the crocetin-functionalized PEG- and CS-coated MNPs were centrifuged at 6000 rpm for 15 minutes. The supernatant was taken out to measure the amount of unbound crocetin. The NPs were washed 3 times using DW and centrifuge. The NP's were then re-suspended in deionized water and a representative sample was dried for compositional analysis. At the end of this process, six (6) samples were made; 5X-Cro-CS-MNPs, 10X-Cro-CS-MNPs, 20X-Cro-CS-MNPs, 5X-Cro-PEG-MNPs, 10X-Cro-PEG-MNPs, and 20X-Cro-PEG-MNPs.

2.3.1 Calculation of the Crocetin Loading

Crocetin Loading was measured by the indirect method. The amount of unbound crocetin was collected from the aliquot in section 3 and its absorbance was measured for it at 430 nm using a UV/Visible spectrophotometer. The amount of bound crocetin was measured by the difference between the amount of crocetin added to functionalize the PEG- and CS-coated MNPs and the amount of free crocetin in the aliquot of the binding process. Equation 2 shown below was used to calculate the efficiency of crocetin coating:

$$\text{Loading Efficiency (\%)} = \frac{\text{Amount of Loaded Crocetin}}{\text{Amount of Initially Added Crocetin}} \times 100 \quad (\text{Equation 2})$$

2.4 Characterization Techniques

Neat and coated MNPs were characterized for their composition, morphology, and properties using various characterization techniques. The composition was studied by X-ray diffraction (XRD), Fourier-transform infrared spectroscopy (FTIR), and thermogravimetric analysis (TGA). An automated Phillips X-ray diffractometer (Phillips, Amsterdam, Netherland), with a step size of 0.02° , a scan rate of 2° per min, and a scan range from $2\theta = 10^\circ$ – 70° was used on a dry sample. FTIR analysis was conducted using a Nicolet Nexus 470 infrared spectrophotometer (Massachusetts, USA), where samples were pre-pressed with KBr, then scanned over the normal range of 4000 – 400 cm^{-1} . Thermogravimetric analysis (TGA) was carried out using a TGA-50 Shimadzu thermogravimetric analyzer (Kyoto, Japan), where pre-weighed powder samples were heated to 600°C at a heating rate of $20^\circ\text{C}/\text{min}$ using an aluminum pan in air, and the percent weight loss was followed and correlated with the original composition of the NPs. A detailed description of the morphology of the NPs was examined by Transmission electron microscopy (TEM; CM10-Phillips Amsterdam, Netherland). Samples were prepared for imaging by spreading drops of NPs diluted dispersion on a copper grid that was coated with a thin layer of carbon and then air-dried. Magnetic properties of the neat and coated NPs were measured as a function of the applied magnetic field at room temperature and were measured using a vibrating sample magnetometer (VSM, Quantum Design Inc, San Diego, CA, USA) instrument.

2.5 Kinetic Release Study of Crocetin

The release kinetics of crocetin from the crocetin-functionalize PEG- and CS-coated MNPs were studied in physiological pH (7.4) as well as in acidic media at pH 5.6. In a typical experiment, 0.1 mg/ml of each sample of 5X, 10X, and 20X crocetin-functionalized NPs was dosed in phosphate-buffered saline (PBS) (Sigma Aldrich, USA) at pH 7. Another set of samples was made with PBS adjusted pH to 5.6, using a 0.1 M HCl solution, to mimic the acidic medium of the cancer microenvironment. The solution was then kept in the incubator at 37°C under constant mixing. At a fixed time, interval 1.5 ml was taken out and replaced by fresh PBS with the same pH. Then the NPs were maintained back at 37°C after being mixed and re-suspended properly. The concentration of drug released was determined by UV–Visible spectrophotometry at 430 nm and using a calibration curve of free crocetin (Hafezi Ghahestani et al., 2017; Soltani et al., 2017). The percentage of crocetin released was calculated as in the following Equation 3:

$$\text{Release (\%)} = \frac{(\text{Amount of Free Crocetin After Kinatic Release})}{(\text{Amount of Crocetin Loaded in Polymer-MNPs})} \times 100 \quad (\text{Equation 3})$$

2.6 In Vitro Cytotoxicity

Hepatocellular carcinoma cell line, HepG2, was purchased from American Type Culture Collection (ATCC, USA). Cells were maintained in 75 cm² culture flasks using Roswell Park Memorial Institute Medium (RPMI) (Life Technologies, USA), supplemented with 10% fetal bovine serum (Life Technologies, USA) and 1% penicillin/streptomycin (Life Technologies, USA). Cells were grown in 5% CO₂ at 37°C and 100% humidity.

2.6.1 MTT Assay

HepG2 cells were seeded at a density of 6000 cells/well in a 96-well plate and allowed to attach for 24 hours. After attachment, the complete growth medium was replaced by a fresh medium with the following treatments. Different concentrations of crocetin including 0.05, 0.5, 3, 5 mg/ml were tested. As well as different samples of MNP were tested with concentrations including 0.05, 0.07, 0.09 or 0.1 mg /ml. Incubation was done over two-time points of 24 hrs and 72 hrs. After incubation, 10 μ l of MTT (5 mg/ml) was added to each well and then incubated at 37°C for 3 hr. After 3hrs, the content is discarded and 100 μ l of dimethyl sulfoxide (DMSO) was added to each well. The 96-well plate was wrapped with foil and placed in the shaker for 15 mins at low speed. The plate was allowed to incubate for 15 minutes. Afterward, the absorbance was measured at 570 nm.

$$\text{Cell viability (\%)} = \frac{(\text{Absorbance of tested compound})}{(\text{Absorbance of control})} \times 100$$

Chapter 3: Results and Discussion

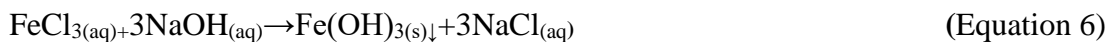
3.1 Characterization of Pure Magnetite NPs

The synthesis method of magnetite nanoparticles (MNPs) used in this study was developed in our research group (El-Kharrag et al., 2017). Magnetite (Fe_3O_4) is considered a combined structure of FeO and Fe_2O_3 within a unified crystal lattice. The majority of the published research following the co-precipitation method to prepare MNPs recommends an inert atmosphere to avoid the formation of phase impure MNPs and add a base to the Fe^{2+} and Fe^{3+} ions mixture to form MNP. Equation 4 shows that when the synthesis is prepared in the presence of air, FeO gets oxidized to Fe_2O_3 , leaving a phase pure Fe_3O_4 .



A Pourbaix diagram; Figure 6, is used to estimate the most thermodynamically stable phases under various pH conditions (Perry et al., 2019). It also allows determining the corrosion behavior of a metal in water solutions i.e. the direction of electro-chemical processes and the equilibrium state of the metal at a certain electrode potential in a water solution at a certain value of pH. In a solution with pH 10 to 14 several species of iron oxide can be present including FeO_4^{2-} , Fe_2O_3 , $\text{Fe}(\text{OH})_2$, and HFeO^{2-} . Oxidation reactions are shown in Equations 4 and 5 explain why synthesis of MNPs in alkaline media in presence of air is risky if we want to avoid the formation of iron oxides other than the magnetite (Fe_3O_4) phase. However, if solutions were pre-adjusted to be highly alkaline before the addition of Fe^{2+} and Fe^{3+} ions then MNPs would be spontaneously precipitated as the highest thermodynamically stable phase.

Equation 6 will take place first then Equation 4. Even though all preparations were carried out in presence of air phase pure Fe_3O_4 will be the end product.



In the current study, aqueous media used for the preparation of MNPs were pre-adjusted to a pH 13 using NaOH to avoid the formation of other non-magnetite iron oxides. To determine the phase purity of the precipitated MNPs, XRD, FT-IR, and TGA analyses were conducted.

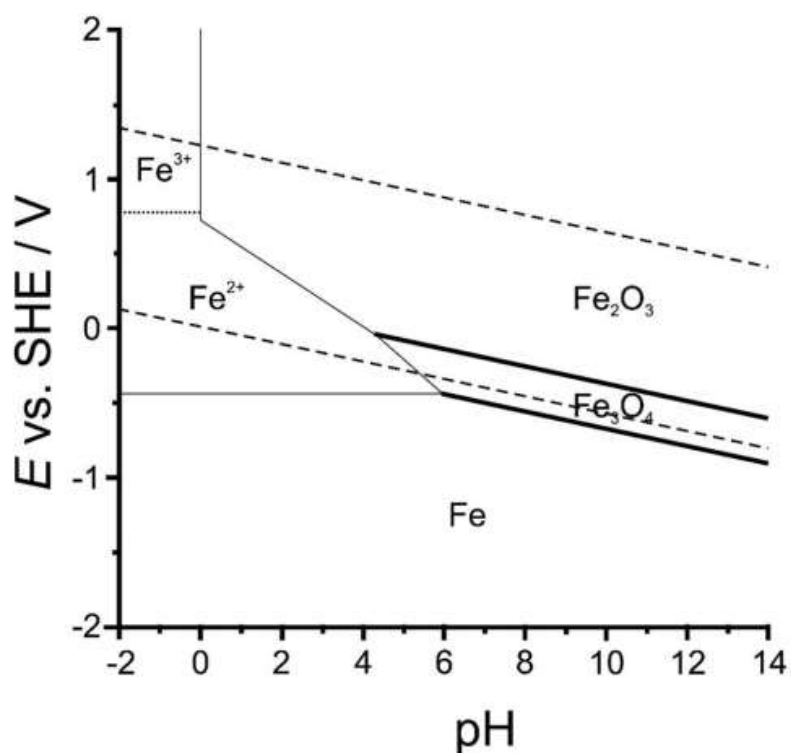


Figure 6: Pourbaix diagram showing the phase composition as a function of pH of the aqueous medium

The XRD pattern in Figure 7 shows the phase purity and crystallinity of the as-prepared MNPs. The peaks formed align with the JCPDS (00-019-0629) pattern of pure magnetite phase including the characteristic peaks at 2θ values are 29.9° (220), 35.2° (311), and 43.1° (400) (Santos et al., 2016). The relative broadness of the XRD peaks indicates that the as-prepared MNPs are in the nanoscale. The absence of hematite or other hydroxides in the XRD patterns of the MNPs prepared in the current study confirms the phase purity of the prepared MNPs. However, possible surface oxidation of the precipitated MNPs may result in the formation of a thin layer of maghemite ($\gamma\text{-Fe}_2\text{O}_3$), where all Fe^{2+} ions are oxidized to Fe^{3+} ions. Both magnetite and maghemite phases share the same crystal structure and XRD pattern, hence cannot be distinguished from each other upon the analysis of their XRD patterns.

Figure 8 shows the FTIR spectrum of the as-prepared MNPs. Bands at wavenumbers of 430, 584, and 622 cm^{-1} are characteristic of the Fe-O stretching mode of absorption of the magnetite phase, while the broad band around 3400 cm^{-1} is characteristic of the stretching mode of absorption of the O-H bond, which is attributed to the presence of physically adsorbed water molecules. This has been further confirmed in the TGA thermogram of the as-prepared MNPs shown in Figure 9. The TGA thermogram showed weight loss values of about 6% taking place at around 100°C . This is attributed to the evaporation of the physically adsorbed water. This loss continued to take place at a slower rate as the temperature increased. This could be attributed to the presence of multi-layers of water of hydration onto the surfaces of the NPs. Furthermore, we expect high agglomeration between the magnetite NPs which

could result in water molecules getting trapped in between that is later lost in TGA at temperatures higher than 100°C.

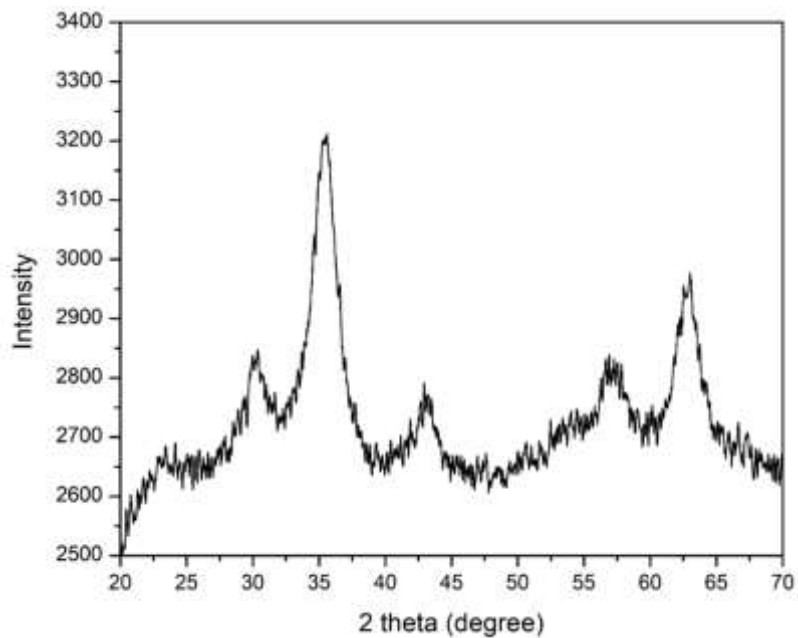


Figure 7: XRD pattern of the as-prepared magnetite nanoparticles (MNPs)

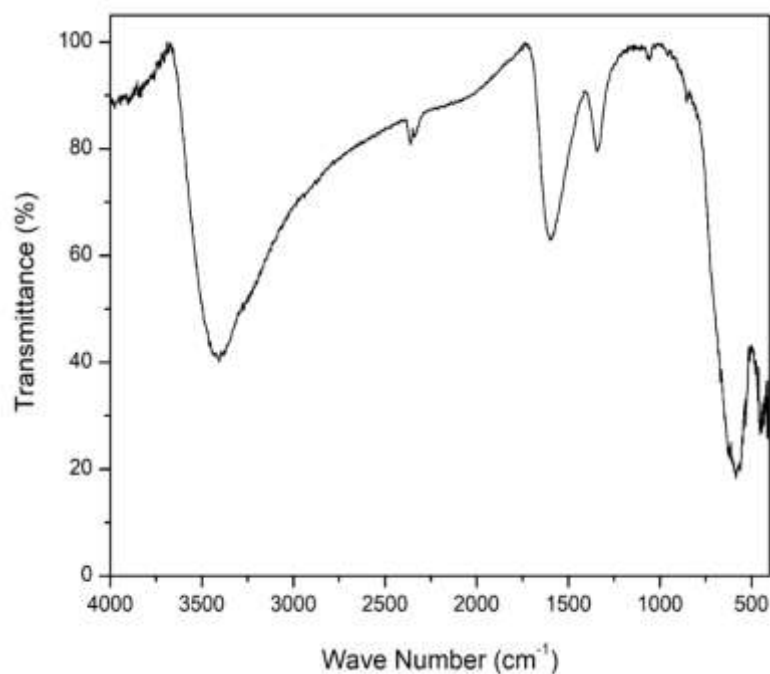


Figure 8: FTIR spectrum of the as-prepared magnetite nanoparticles (MNPs)

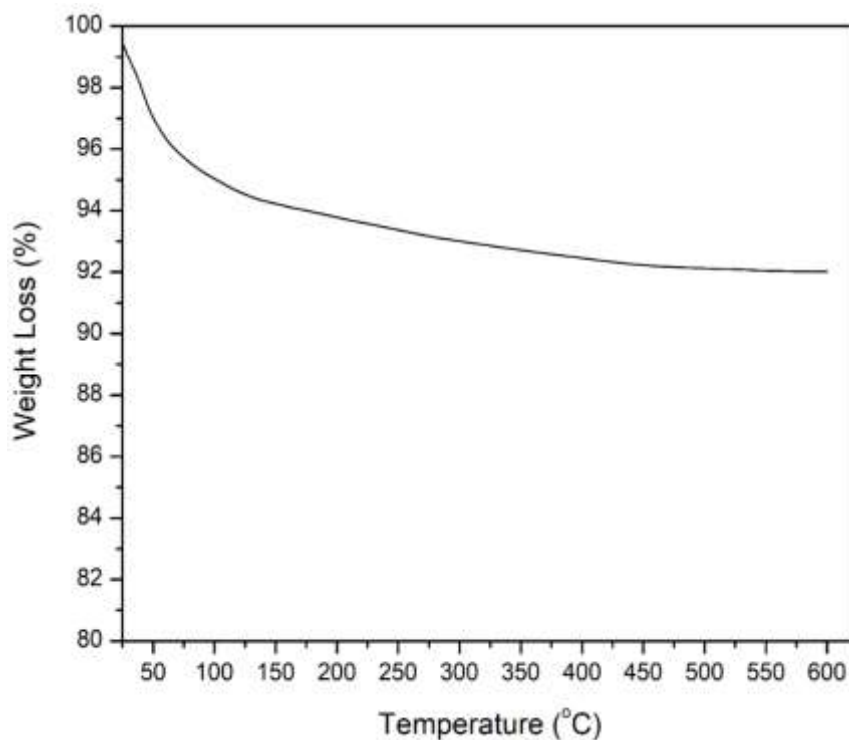


Figure 9: TGA thermogram of the as-prepared magnetite nanoparticles (MNPs)

Figure 10 shows a TEM micrograph of the as-prepared MNPs, where a high extent of agglomeration is shown. The micrograph indicates the formation of rounded NPs with homogeneous size distribution. The average sizes of the individual NPs were 6 nm.

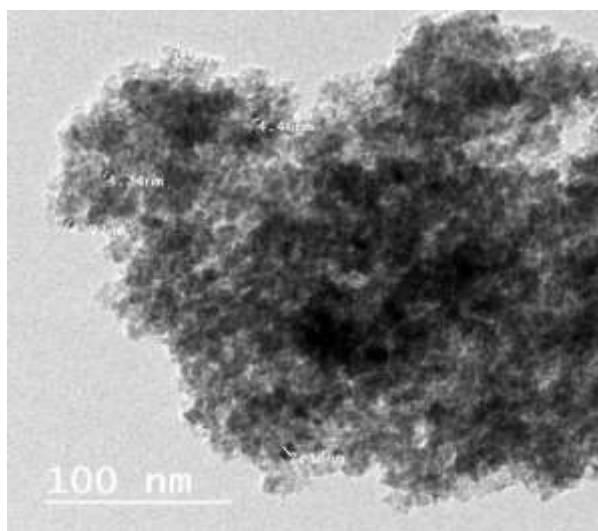


Figure 10: TEM micrograph of the as-prepared magnetite nanoparticles (MNPs)

The magnetic hysteresis of pure MNP is illustrated in Figure 11. The results of the magnetization measurements of pure MNPs as a function of applied field at room temperature showed a maximum magnetization of 31.6 emu/g which is lower than what's reported in the literature (Nkurikiyimfura et al., 2020). This could be attributed to the high agglomeration of the NPs which lowers the surface area and hence gives lower magnetization. This could be also attributed to the possible formation of an oxidized layer onto the surfaces of the as-prepared MNPs. Moreover, the absence of coercivity in the magnetization hysteresis of the as-prepared MNPs indicates its super paramagnetic nature. Considering the characterization of the as-prepared MNPs, no signs of non-magnetite phases were found. These findings further support their eventual application as a drug delivery vehicle for cancer treatment.

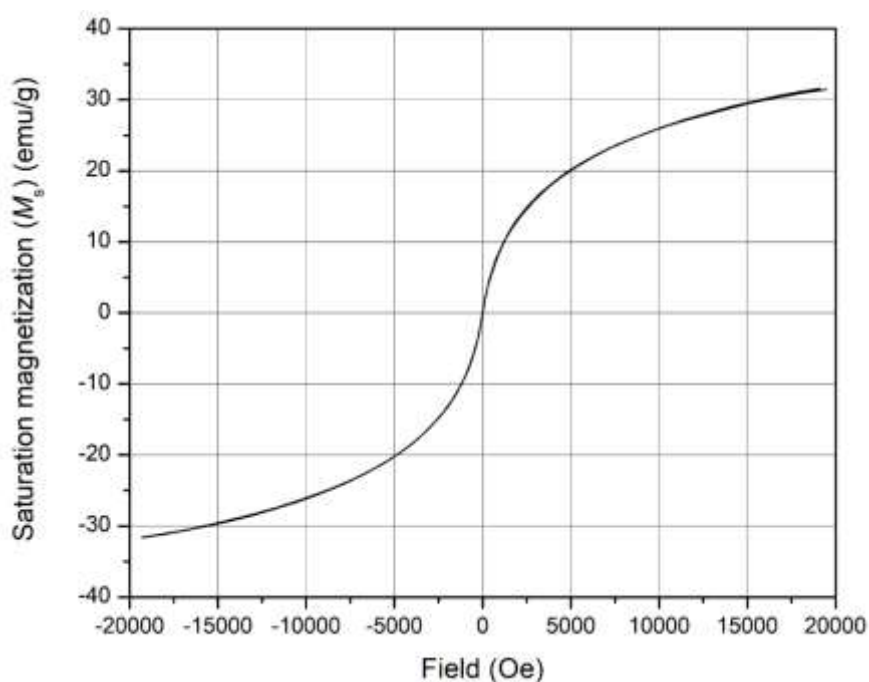


Figure 11: Magnetization hysteresis of the as-prepared magnetite nanoparticles (MNPs)

3.2 Characterization of Different Surface Coating Materials

MNPs have a large surface-to-volume ratio and therefore possess high surface energies. Consequently, they tend to aggregate to minimize these energies. Moreover, the pristine MNPs have high chemical activity and are easily oxidized in air, generally resulting in loss of magnetism and dispersibility (Wu et al., 2008). Furthermore, in biomedical applications neat MNPs undergo non-specific interactions with the serum proteins *in vivo* leading to their rapid elimination from the body (Santos et al., 2016). To address this limitation the surfaces of the MNPs need to be hydrophilic for the NPs to be stable and have a prolonged circulation inside the body.

In this study, we chose two different types of organic coatings both known for their use in various biomedical applications. PEG and CS are both biocompatible and biodegradable. Applying the organic coating onto the surfaces of MNPs was done in two different methods. For the case of CS, we followed an in-situ approach where the synthesis of MNPs was carried out in the presence of CS. This was done due to the weak solubility of CS in aqueous and basic media. Initially, CS solutions containing up to 1% by weight were prepared by dissolving the corresponding weights of chitosan in 0.2 % acetic acid solution. The $\text{Fe}^{2+}/\text{Fe}^{3+}$ salts were dissolved separately in an equal volume of the chitosan solutions. Then vigorously mixed to form $\text{Fe}^{2+}/\text{Fe}^{3+}$ mixture solution, after that injected into the NaOH solution. At the end of the addition, extra chitosan was washed out by consecutive cycles of washing and decantation using deionized water. The formed CS-MNPs were separated by decantation, centrifuged, washed, and then dried before being characterized for their composition, morphology, and magnetic properties.

For PEG we followed an ex-situ approach via the direct immersion method. We treated the freshly prepared MNPs in solutions with PEG at different weight percentages, up to 18.5%. MNPs immersed in PEG were left to stir overnight to ensure a full coating of the MNPs. The next day excess PEG was washed out by cycles of washing and decantation with deionized water. The formed PEG-MNPs were separated by decantation, centrifuged, washed, and then dried before being characterized for their composition.

In the current study, the use of PEG and CS at different percentages were investigated in detail to choose the optimum conditions to be used in the further immobilization of crocetin onto the organic-coated MNPs for targeted drug delivery applications. The following sections discuss the characterization of CS- and PEG-coated MNPs in terms of their composition, morphology, and magnetic properties.

3.2.1 Characterization of PEG-Coated MNPs

3.2.1.1 XRD Analysis of PEG-Coated MNPs

Figure 12 shows the XRD patterns of all PEG-coated MNPs as a function of the proportion of PEG used during the preparation. Compared with the XRD pattern of pure MNPs, all XRD patterns of the PEG-coated MNPs showed the consistent presence of pure MNPs with no signs of the presence of other non-magnetite phases. We observe the peaks in all concentrations are well defined which indicates the phase purity and crystallinity of MNPs were not affected by the PEG coating onto their surfaces. Moreover, the continued relative broadness of the XRD peaks indicates the presence of the PEG-coated MNPs in the form of nanoscale particulates.

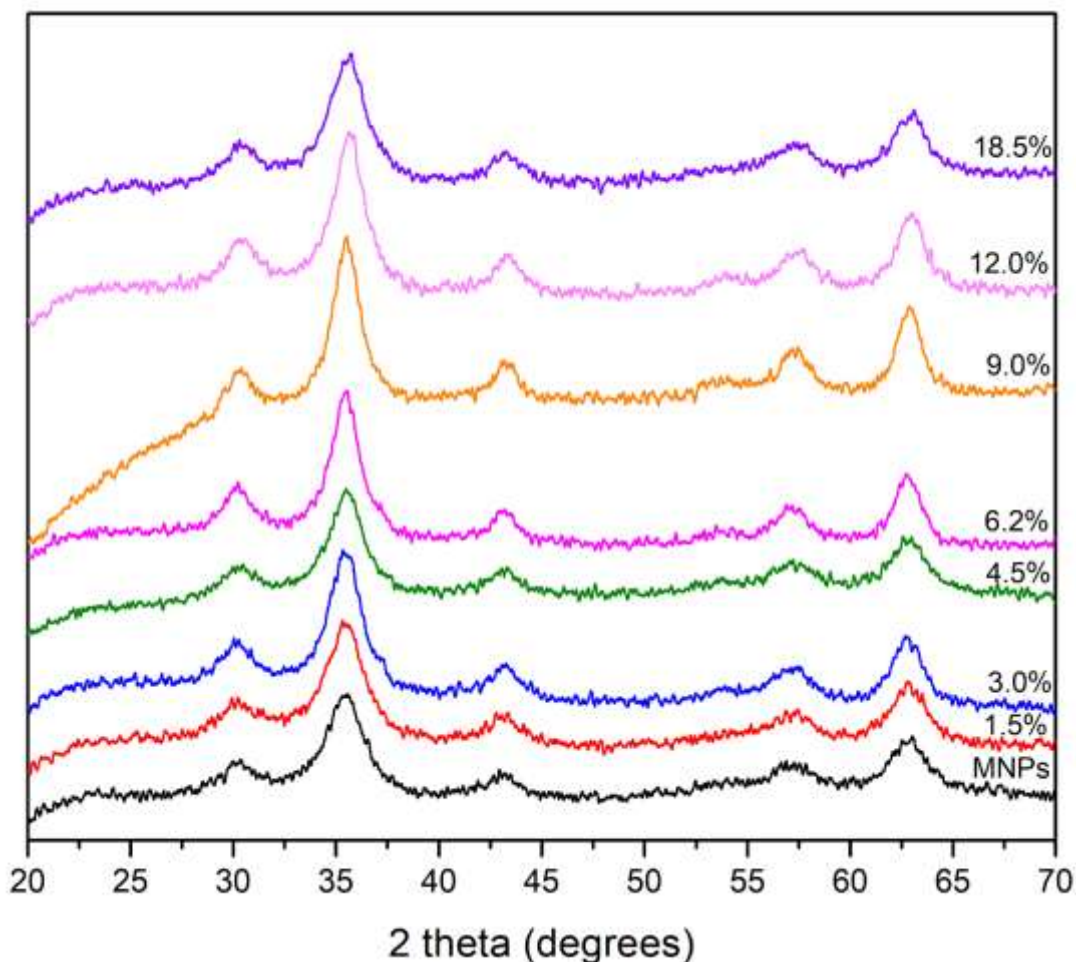


Figure 12: XRD patterns of the PEG-coated MNPs as a function of the concentration of PEG

3.2.1.2 FTIR Analysis of PEG-Coated MNPs

Figure 13 shows the FTIR spectra of PEG-coated MNPs as a function of the initial proportion of PEG during the preparation, and as compared with the FTIR spectrum of the as-prepared pure MNPs phase. Moreover, a spectrum of pure PEG is also shown in the respective spectra for comparison. In all spectra, magnetite is represented by its bands at 430, 584, and 622 cm^{-1} , with band intensities, decreasing and shifting to lower wavenumbers with all the PEG-MNPs percentages. This can be possibly due to chemical interactions between the PEG and the MNPs surfaces. The

FTIR for the PEG-coated MNPs shows a shoulder absorption band at 951 cm^{-1} corresponds to -CH out-of-plane bending vibration of the PEG coating. Furthermore, the presence of PEG as a coating onto the surfaces of MNPs is confirmed with the appearance of a new peak at 1100 cm^{-1} which is a signature peak of the C-O-C bond of PEG. The IR band at 2860 cm^{-1} corresponds to -C-H asymmetric stretching vibration, especially in the spectra of samples containing $\geq 4.6\%$ of PEG. Moreover, the signature peaks at 3402 cm^{-1} due to hydroxyl stretching is overlapping with water OH stretching vibrations in all samples, which could be also attributed to the physically adsorbed water molecules. Taken together, these findings confirm the presence of PEG as a coating onto the surfaces of MNPs (Sarkar et al., 2016).

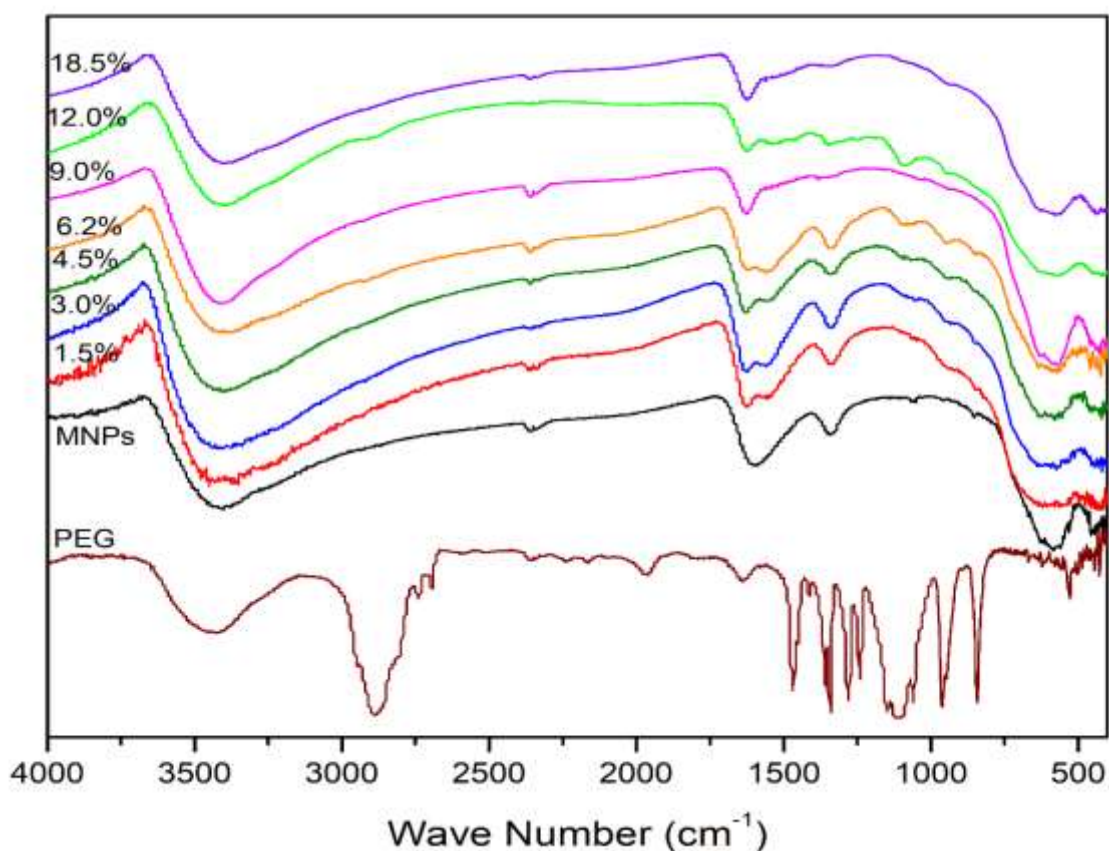


Figure 13: FTIR spectra of the PEG-coated MNPs as a function of the concentration of PEG

3.2.1.3 TGA Analysis of PEG-Coated MNPs

Pure MNPs showed an average weight loss of 6%, as was previously shown in Figure 9. This was attributed to the removal of physically adsorbed water molecules. Figures 14 show the TGA thermograms of PEG-coated MNPs as the function of the proportion of PEG initially added during preparation. For comparison, the TGA thermogram of pure PEG was also included in Figure 15. Pure PEG showed an overall 100% weight loss around 250°C, which is attributed to the thermal and oxidative decomposition as well as the combustion of the PEG chains. On the other hand, TGA thermograms of PEG-coated MNPs shown in Figure 14 indicated the presence of two stages of weight loss. The first event of weight loss accounts for the evaporation of physically and chemically adsorbed water; around 100°C. The second event of weight loss was observed around 250±10°C and is attributed to the degradation of PEG linked onto the surfaces of the MNPs.

With the increasing percentage of PEG, we observe an increase in the weight loss around 100°C attributed to the physically and chemically adsorbed water on the surface of PEG. This weight loss is then slowly stretched until the second major thermal event takes place around 250°C, which corresponds to the degradation and thermal decomposition of PEG coating. This stretch could be due to the increase in the thickness of the PEG coating layer as a result of the development of intermolecular forces, such as H-bonding and dispersion forces, amongst PEG molecules. As a consequence, we observe with the higher percentage of PEG, a greater weight loss around 250°C which indicates multilayer formation of PEG on top MNPs. The multilayers formed to contribute to the increase in physically and chemically adsorbed

water molecules. A schematic representation of the PEG coating onto the surfaces of MNPs as well as the formation of a hydrated layer is represented in Figure 16.

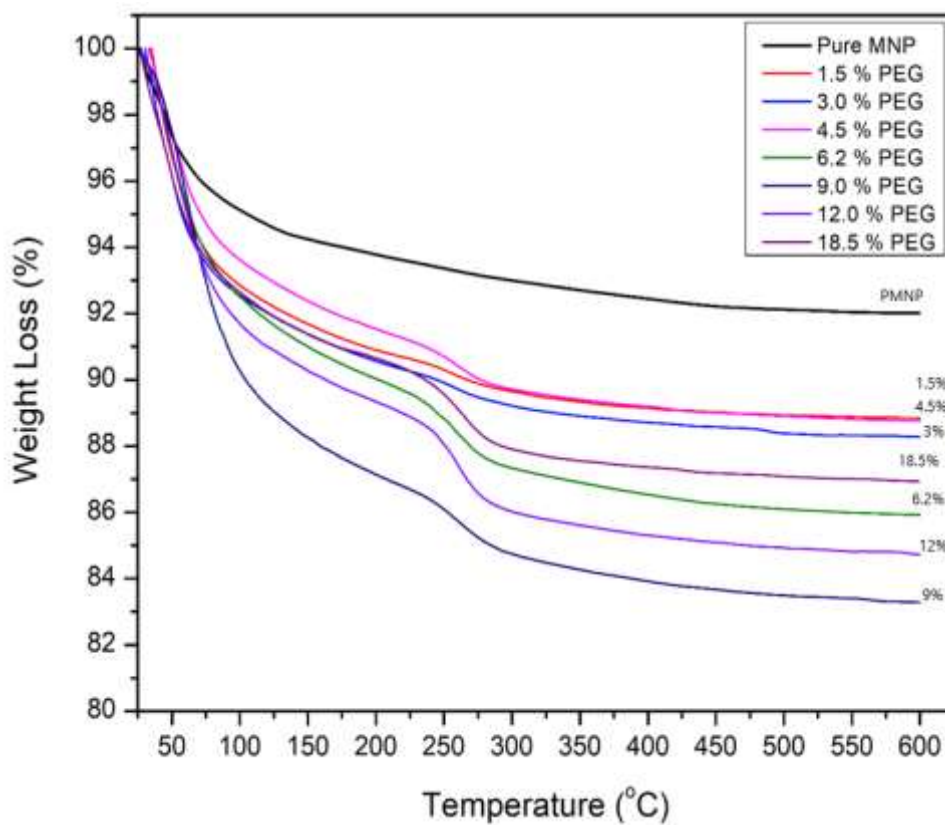


Figure 14: TGA thermograms of the PEG-coated MNPs as a function of the concentration of PEG

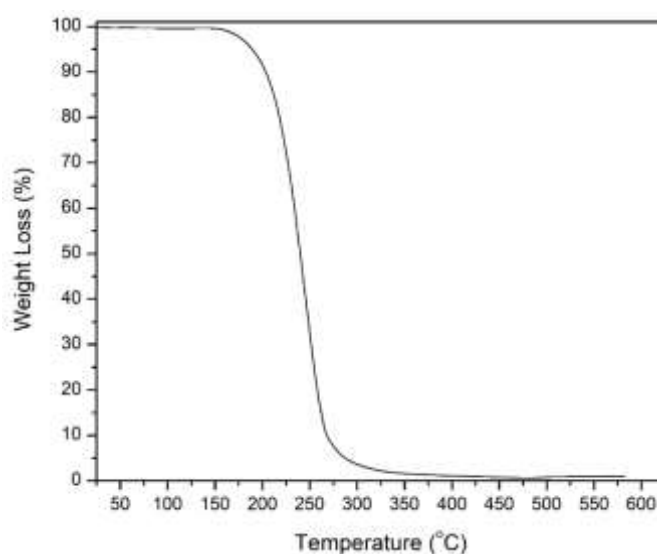


Figure 15: TGA thermogram of a pure PEG powder sample

Based on these discussions, Figure 17 shows a summary of the TGA weight loss as a function of the percentage of PEG added to MNPs. A maximum loading was observed with 12% PEG-MNP, which was considered an optimum proportion to be used for the further immobilization of crocetin molecules.

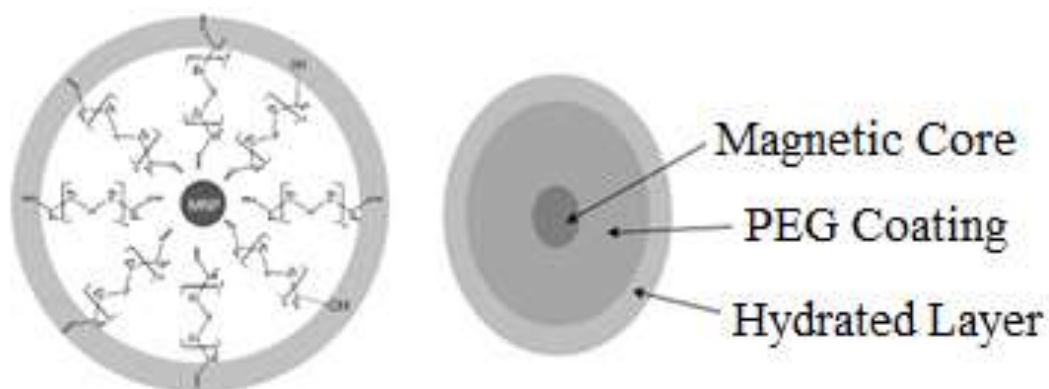


Figure 16: A schematic diagram showing the formation of PEG and hydrated layers onto MNPs surfaces

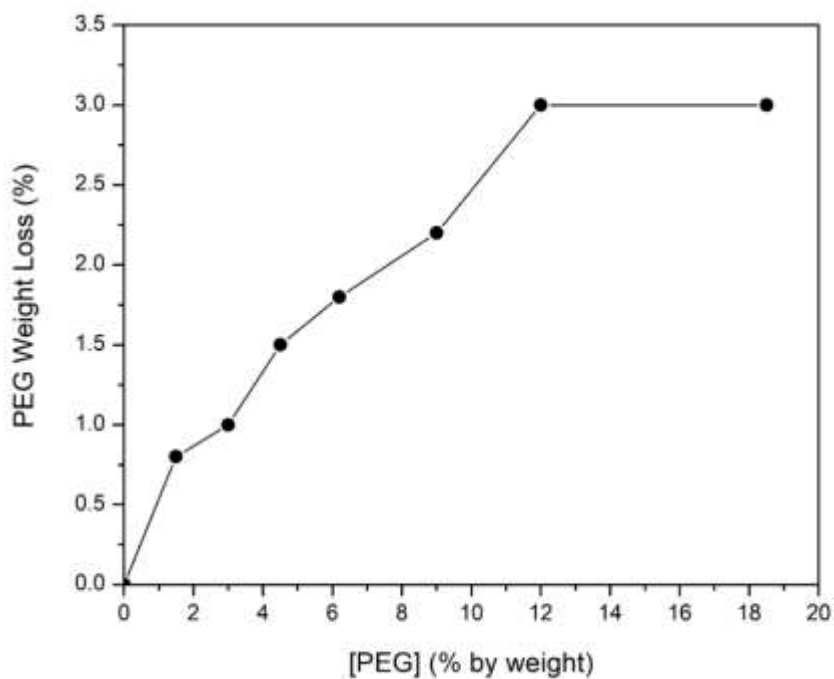


Figure 17: The extent of coating of MNPs with PEG as depicted from their TGA thermograms

3.2.1.4 Morphological TEM Analysis of PEG-Coated MNPs

Figure 18 shows the TEM imaging of PEG-coated MNPs at different concentrations of PEG. Overall, we observe the presence of the coating reduced the extent of agglomeration compared to pure magnetite previously shown in Figure 10. The coated MNPs retained the round shape with a homogeneous size distribution. The size of the particles increased slightly with the increasing PEG thickness. Compared to pure MNPs with size 4.4 ± 5 nm, 1.5% PEG-MNPs had a size of 5.1 ± 5 nm while 9% had a size of 6.8 ± 5 nm and finally 18.5% size was around 7.5 ± 5 nm. The agglomeration observed in some regions can be due to the immersion coating method. The PEG coating was added after the MNPs formation which could give room to some extent for MNPs agglomeration before the PEG coating is formed.

3.2.1.5 Magnetic Properties of PEG-Coated MNPs

To enhance the physiologic characteristics of MNPs, a biocompatible coating onto the surfaces of MNPs is desired, as part of their objective to be used as successful drug delivery vehicles. However, the presence of a non-magnetic layer on a magnetic MNPs core has been always believed to result in a decrease in the magnetic properties of the coated MNPs, hence decreasing their potential for biomedical applications (El-Kharrag et al., 2017; Kayal & Ramanujan, 2010; Maltas et al., 2015; Molina et al., 2013). In the current study, however, the magnetization results shown in Figure 19 for the PEG-coated MNPs as a function of the concentration of PEG indicate a variable behavior. A saturation magnetization of 31 emu/g was observed for the as-prepared neat MNPs; Figure 11. The presence of PEG as a coating onto the surfaces of MNPs resulted in a general increase in the magnetization values compared to pure MNPs,

especially at a higher proportion of PEG. An increasing pattern was observed, where the presence of PEG in the coating resulted in an increase in the magnetization of the PEG-coated MNPs. For example, magnetization saturation values were 42.7, 37.2 and 34.4 for PEG-coated MNPs containing 9%, 12% and 18.5%, respectively. This could be attributed to the role of PEG in reducing the agglomeration of MNPs, resulting in smaller particle size and hence more magnetization compared to the pure MNPs sample where magnetization was minimized due to the decreased surface area because of agglomeration. Santos and his research group observed the same effect of increased magnetization of PEG-GHS-MNPs (67 emu/g) compared to GHS-MNPs (44 emu/g) (Santos et al., 2016). It was attributed that the PEG binding modified the electronic structure of MNPs on the surface which increased magnetization (Santos et al., 2016).

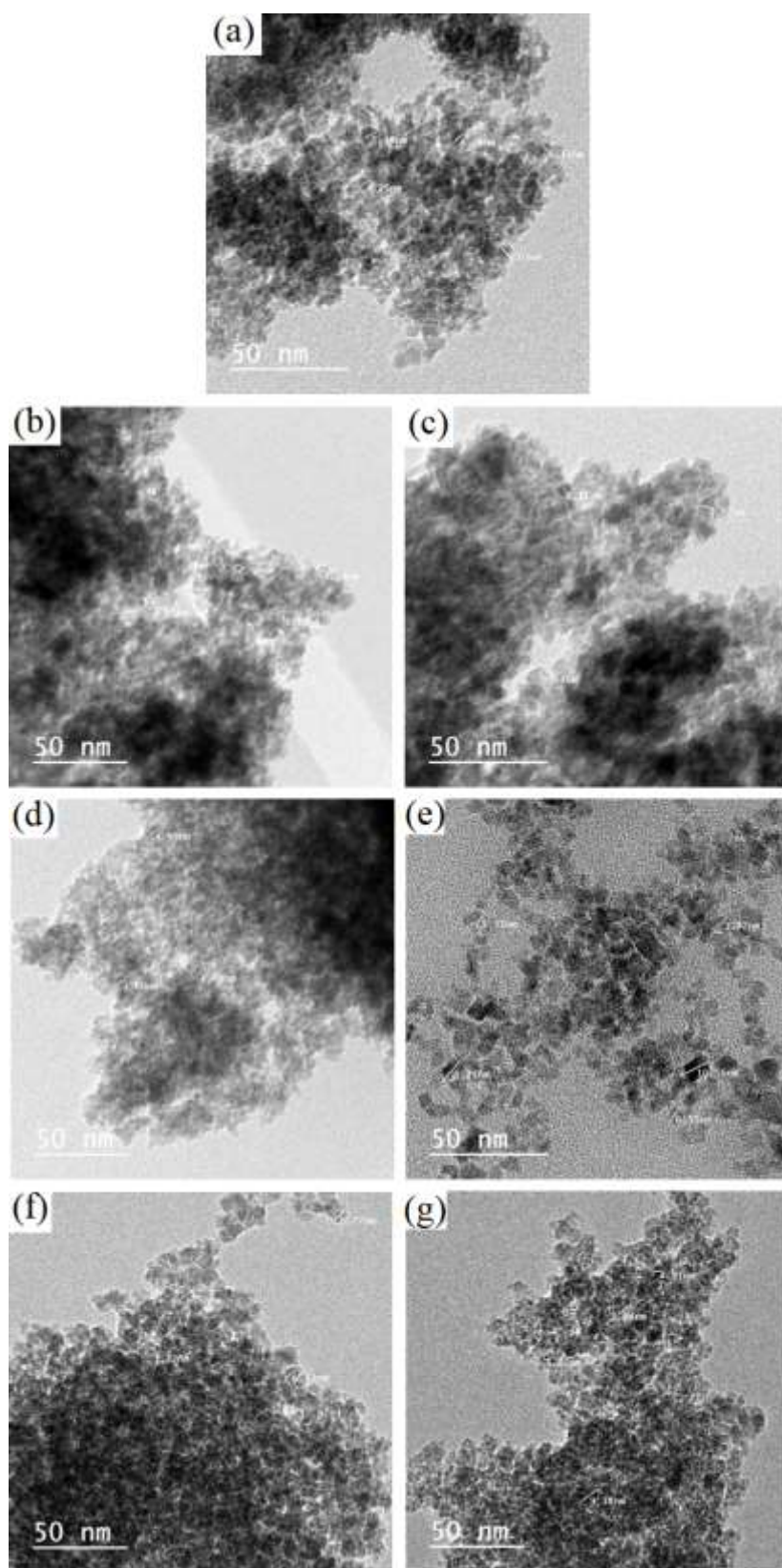


Figure 18: TEM micrographs of PEG-coated MNPs as a function of [PEG]: a) 1.5 %, b) 3.0%, c) 4.5%, d) 6.2%, e) 9.0%, f) 12.0%, and g) 18.5% by weight

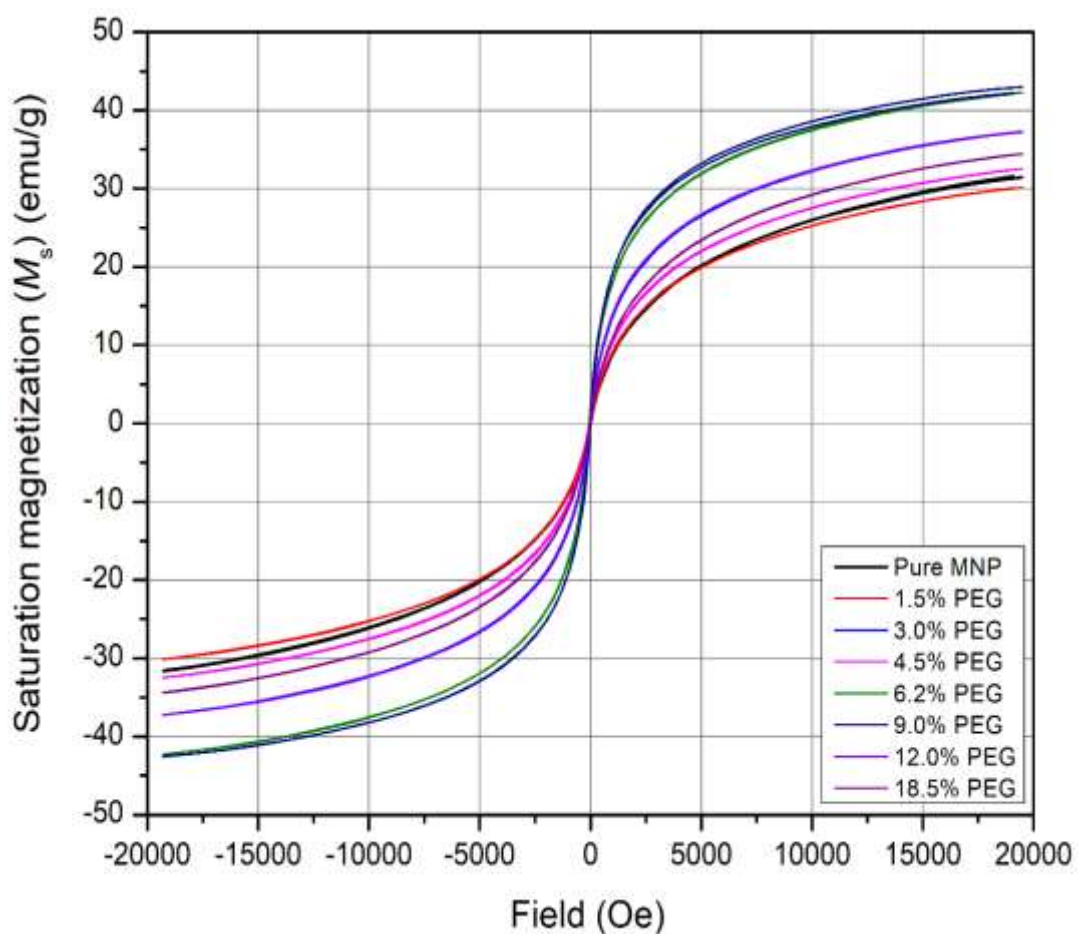


Figure 19: Magnetization hysteresis of the as-prepared PEG-coated MNPs as a function of the concentration of PEG

3.2.1.6 Selection of Optimum [PEG] in PEG-Coated MNPs

Based on the previous results, MNPs coated with 12% by weight of PEG were selected to be further functionalized by crocetin for drug delivery applications. This percentage showed the maximum loading capacity of PEG onto the surfaces of the MNPs, as was clearly indicated from the detailed analysis of their TGA results in Figure 17.

3.2.2 Characterization of Chitosan-coated MNPs

3.2.2.1 XRD of CS-Coated MNPs

Figure 20 shows the XRD patterns of CS-coated MNPs as a function of the concentration of CS. All patterns confirmed the phase purity and crystallinity of MNPs, indicating that the presence of CS did not affect the composition and phase purity of MNPs. All the different percentages of chitosan show the same pattern as pure magnetite. However, an increase in the sharpness of the MNPs XRD peaks was observed by increasing the initial concentration of the chitosan in the coating. This could be attributed to the improved crystallinity of the precipitated MNPs.

3.2.2.2 FTIR of CS-Coated MNPs

The FTIR spectra of CS-coated MNPs with the different weight percentages (up to 1 % by weight) are shown in Figure 21. A spectrum of pure chitosan was also included for comparison. In all spectra, MNPs are characterized by their significant bands at 430, 584, and 622 cm^{-1} , with band intensities decreasing with the increasing chitosan coating. This is attributed to possible chemical interaction between the multi-functional groups in chitosan with the MNPs binding surface. In addition, the presence of CS as a coating onto the surfaces of MNPs diminishes the contribution of absorption of the magnetic core to the spectra. Moreover, the bands of chitosan are shown to dominate the spectra with their increasing concentration. Several characteristic bands of pure chitosan are present in the CS-coated MNPs, as shown in Figure 21. Those bands appeared at 1082, 1382, and 1655 cm^{-1} , and are attributed to the absorption of C-O, C-N, and C=O groups, respectively. The intensity of those bands increased with the increasing percentage of chitosan which could confirm the increasing thickness of

chitosan coating onto the surfaces of the MNPs. In addition, weak-medium intensity broadband appeared at 2848 cm^{-1} , which is attributed to the asymmetric stretching of the C–H bridge. This band was more evident in CS-coated MNPs containing higher concentrations of CS ($\geq 0.7\%$). Another characteristic peak of chitosan was observed at 3432 cm^{-1} corresponding to the stretching vibrations of both O–H and N–H groups, as shown in the chemical structure of chitosan in Figure 2. However, this peak is not clear in the chitosan-coated MNPs due to the overlap with the OH stretching of absorbed water. The evident appearance of chitosan characteristic bands in the coated MNPs confirms the presence of chitosan onto the surfaces of the MNPs. The intensity of those bands increased with increasing the percentages of chitosan, which indicates a higher amount of chitosan coating. This will be further confirmed by TGA thermograms.

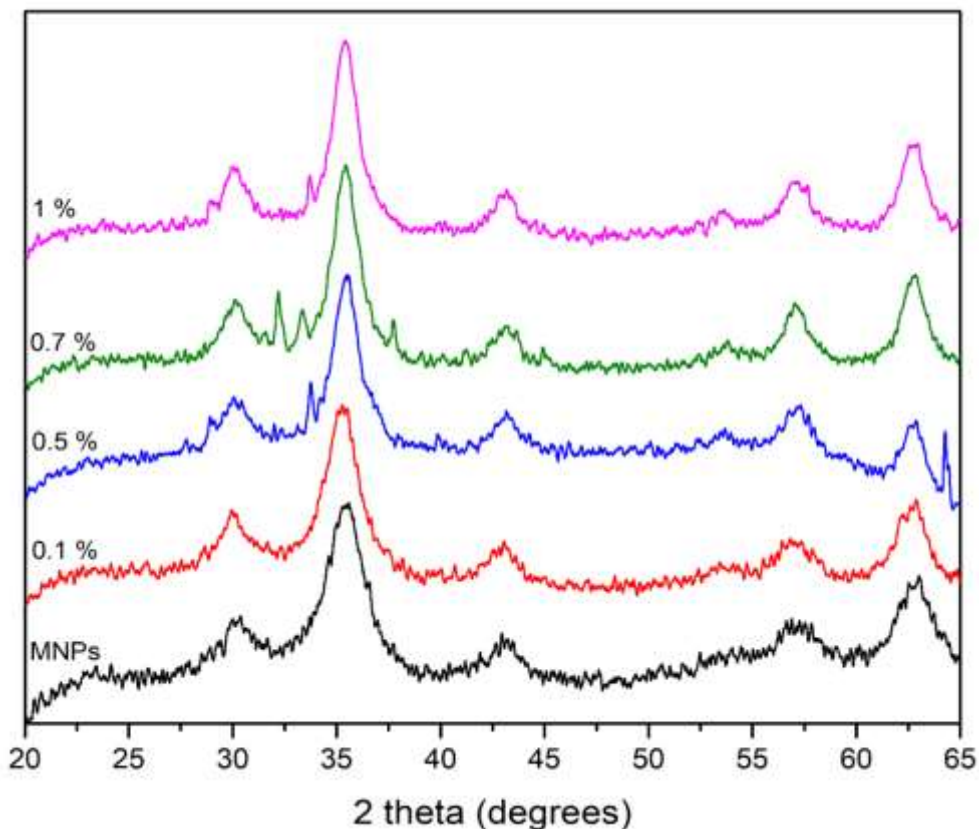


Figure 20: XRD patterns of the chitosan-coated MNPs as a function of the concentration of chitosan

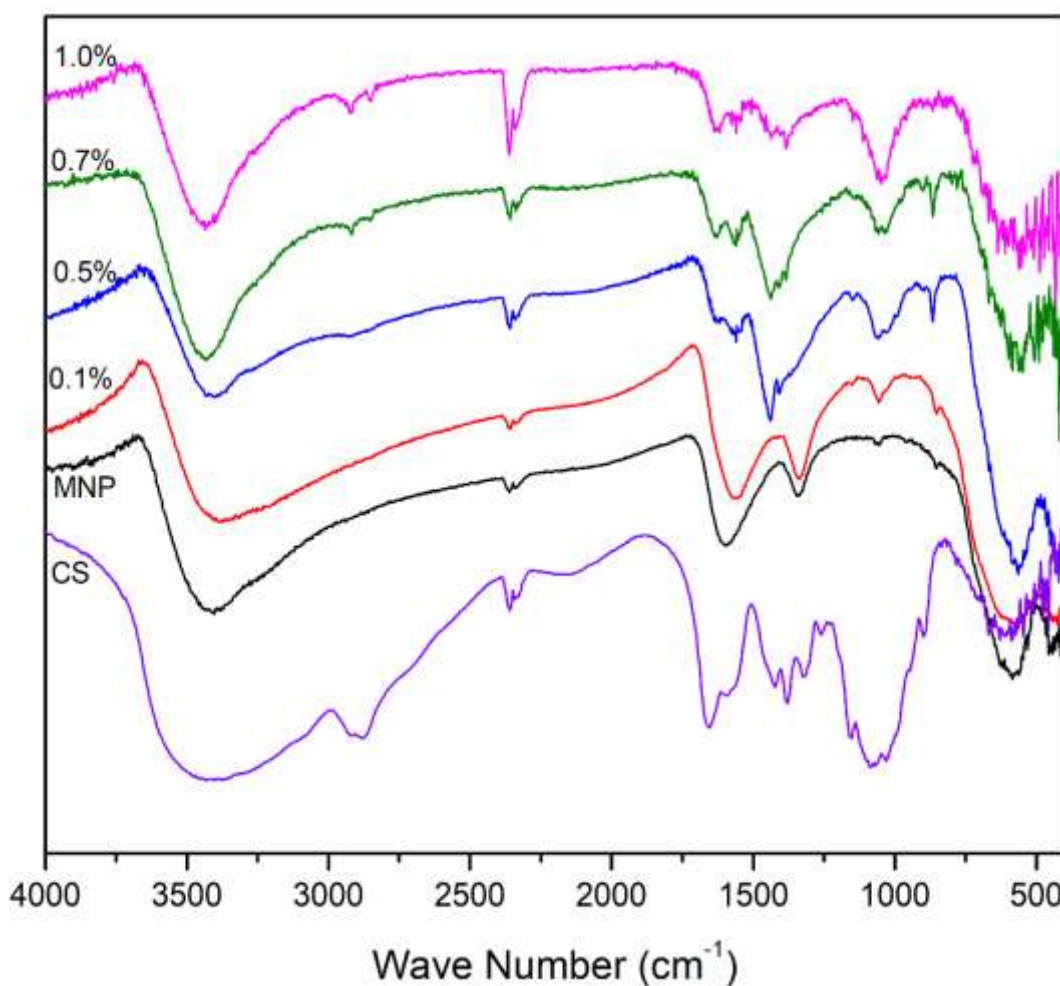


Figure 21: FTIR spectra of the chitosan-coated MNPs as a function of the concentration of chitosan

3.2.2.3 TGA Analysis of CS-Coated MNPs

Figure 22 shows the TGA thermogram of all CS-coated MNPs as a function of the concentration of CS (up to 1% by weight). The TGA thermograms of the as-obtained CS are also shown in Figure 23 for comparison. Pure CS sample shows a complete weight loss after heating it to 600°C in the form of two events. The first event was observed at 100°C and is attributed to the removal of physically and chemically adsorbed water molecules. This was followed by the second major weight loss around 300°C due to the degradation of chitosan that takes place through thermal and oxidative decomposition. Similarly, TGA thermograms of CS-MNPs indicate the

presence of two stages of weight loss. The first event of weight loss accounts for the evaporation of physically and chemically adsorbed water; around 100°C, while the second event took place at 300±10°C and is attributed to the degradation of chitosan linked onto the surfaces of the MNPs.

The thermograms of CS-MNPs compared to pure MNPs showed a lower extent of weight loss due to the evaporation of physically and chemically adhered water molecules, with increasing the concentration of CS. In the presence of 1% chitosan, the lowest weight loss was obtained, as compared with CS-coated MNPs containing other proportions of CS. It should be mentioned that all CS-coated MNPs experienced less weight loss around 100°C vs pure MNPs. This means the amount of water adsorbed onto the MNPs was largely reduced by the presence of CS, and that this amount slightly decreased concurrently with the increase of concentration of CS in the coating. This could be due to extensive hydrogen bonding and dispersion forces between the CS chains, while the existing water forms a layer on the CS coating. A schematic representation of the hydrated layer in CS-MNPs is presented in Figure 24.

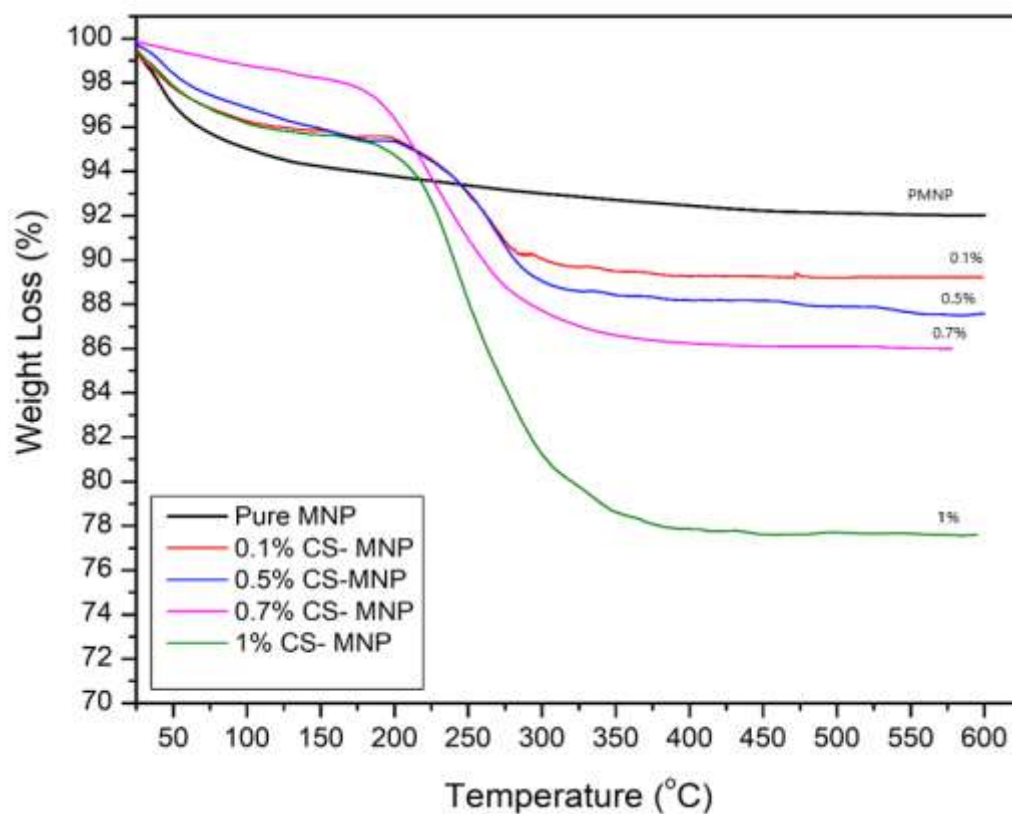


Figure 22: TGA thermograms of the chitosan-coated MNPs as a function of the concentration of chitosan

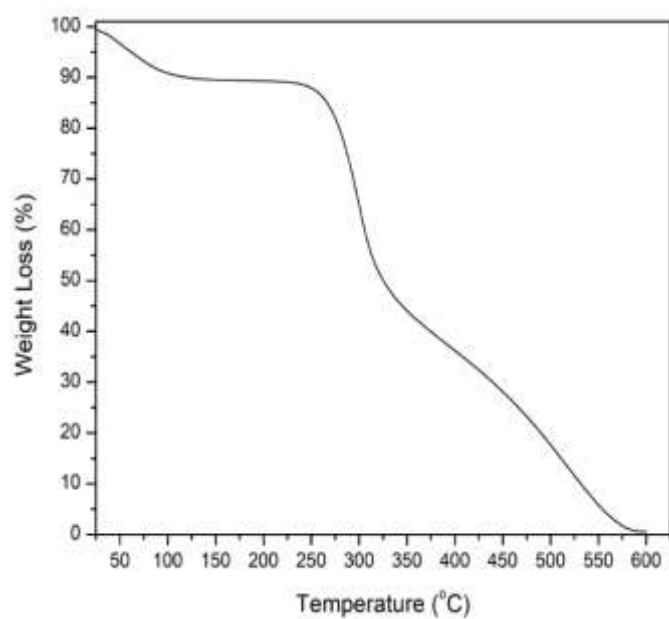


Figure 23: TGA thermogram of pure chitosan

The overall weight loss of the CS-coated MNPs was also shown to increase with increasing the concentration of CS initially added. This could be attributed to the development of secondary forces of interaction, such as H-bonding and dispersion forces, between the CS chains in the coating. These forces, therefore, account for the increase in the thickness of the CS coating layer. It is therefore believed that a double layer is formed onto the surfaces of the MNPs, where the first layer that is in direct contact with the MNPs core is chitosan, while the external layer contains the attached water molecules. This also justifies the removal of water, as a first event, from the surfaces of the chitosan-coated NPs, followed by the removal of the chitosan coating, as shown in the TGA thermograms. Figure 25 shows the optimized weight loss data as depicted from the TGA thermograms of the CS-coated MNPs, and indicates the optimum concentration of 0.5 % of CS as a coating onto the MNPs surfaces. It should be mentioned that this percentage was selected to minimize the effect of the high viscosity of the chitosan medium on the dispersion and eventual injectability of the coated MNPs.

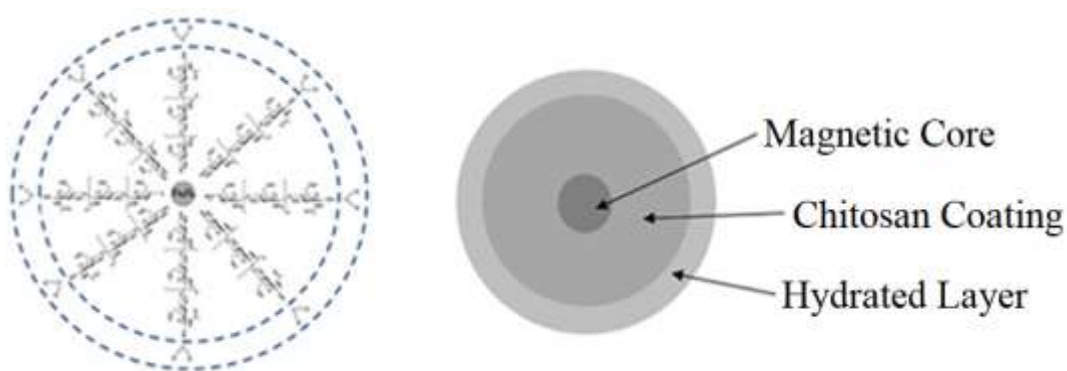


Figure 24: A schematic diagram showing the formation of Chitosan and hydrated layers onto MNPs surfaces

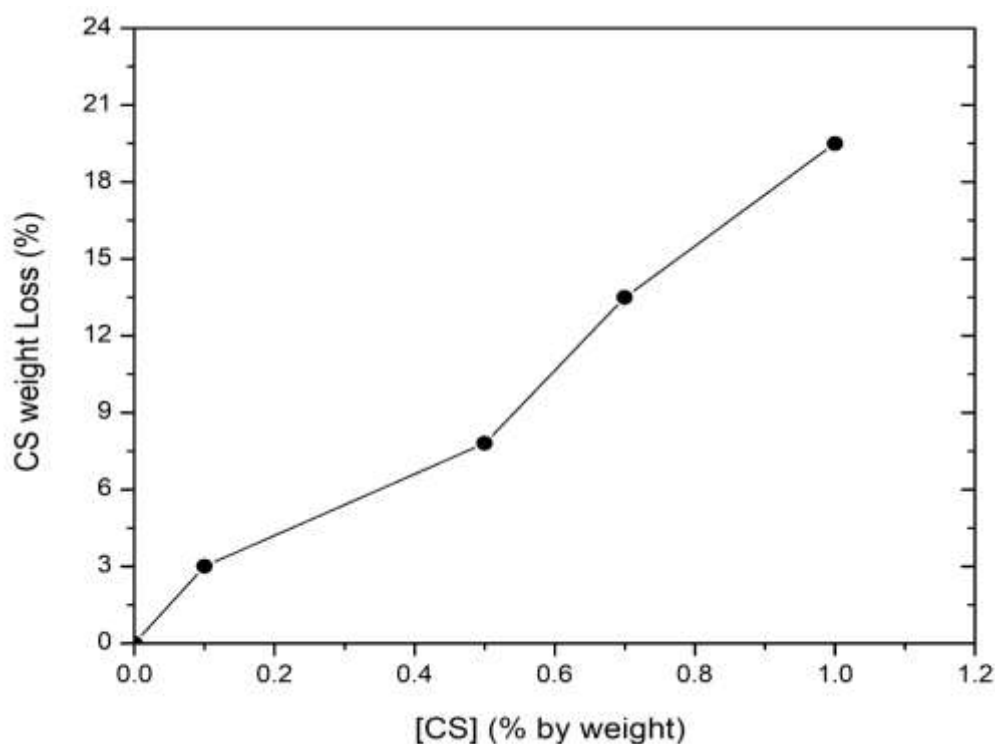


Figure 25: The extent of coating of MNPs with CS as depicted from their TGA thermograms

3.2.2.4 Morphology TEM Analysis of CS-Coated MNPs

The morphology of chitosan-coated MNPs was studied using TEM imaging in Figure 26. All the TEM graphs show homogeneity and uniform size distribution. An overall reduction in the extent of agglomeration of the MNPs was observed and is attributed to the presence of chitosan when compared to pure MNPs. The average size of the NPs increased with the increase in coating thickness. Compared to pure MNPs with an average size of 4.4 ± 5 nm, the size of 0.5% chitosan-coated MNPs was an average 7 ± 5 nm and for 1% chitosan, the average size was 7.9 ± 5 nm. Furthermore, the agglomeration observed in some regions can be due to the intermolecular force between chitosan polymer chains forming hydrogen bonding and dispersion forces.

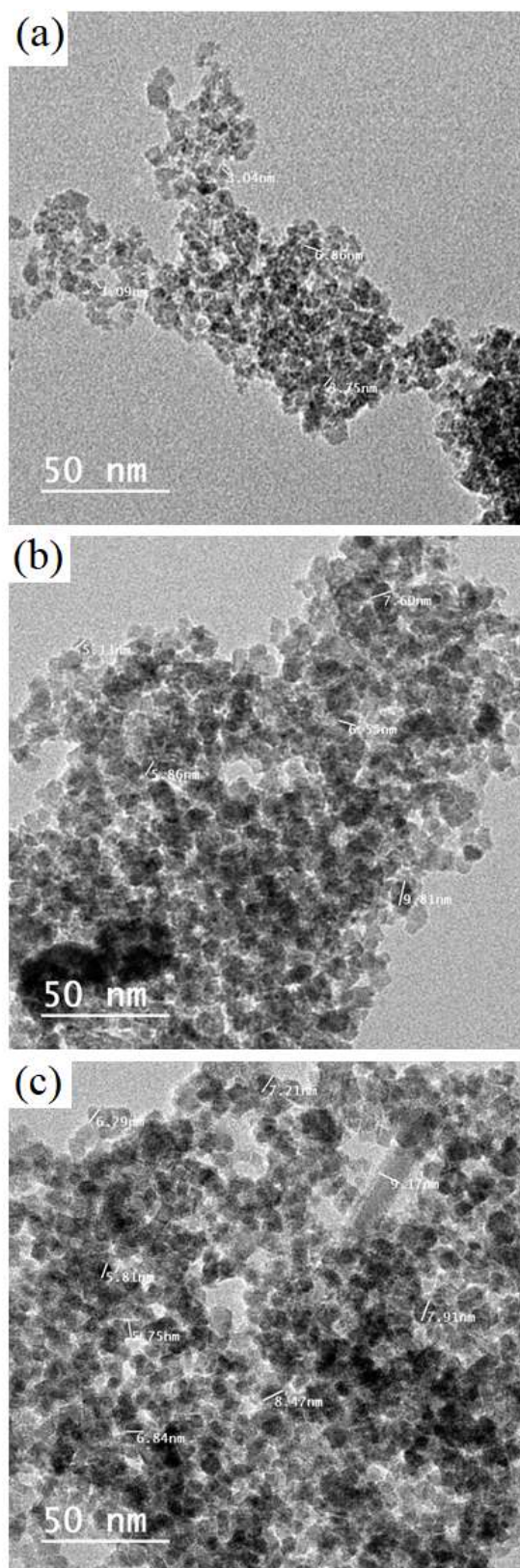


Figure 26: TEM micrographs of CS-coated MNPs as a function of [CS]: a) 0.1 %, b) 0.5 %, and c) 1.0 % by weight

3.2.2.5 Magnetic Properties of CS-Coated MNPs

The magnetization hysteresis of all CS-coated MNPs are shown in Figure 27. The presence of CS as a coating onto the surfaces of the MNPs is shown to enhance the saturation magnetization of the CS-coated MNPs. Saturation magnetization values of 38.3, 37.8 and 34.0 emu/g were obtained for 0.5%, 0.7% and 1% of CS-coated MNPs, respectively. Compared to pure MNPs magnetization of 31.6 emu/g, the observed increase in the saturation magnetization indicates the reduced agglomeration of MNPs as a result of CS coating, as compared to pure MNPs. On the other hand, with the increasing concentration of chitosan, a reduction in the saturation magnetization was observed, which could be due to the increase in the thickness of the CS coating layer.

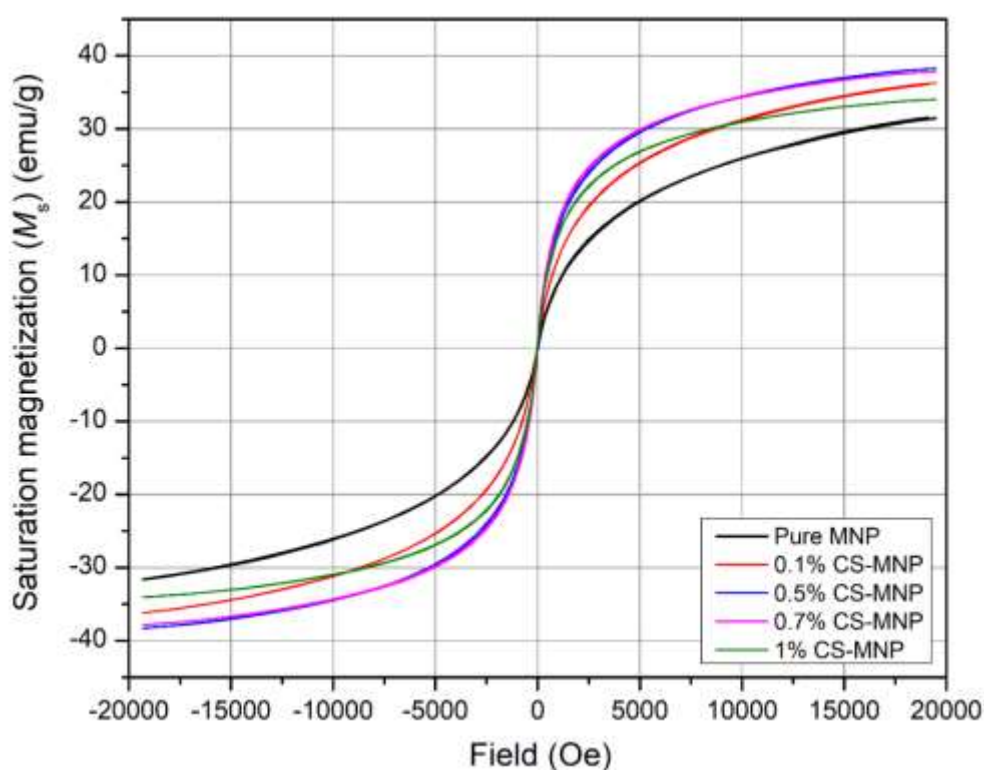


Figure 27: Magnetization hysteresis of the chitosan-coated MNPs as a function of the concentration of chitosan

3.2.2.6 Selection of Optimum [CS] in CS-Coated MNPs

The presence of CS as a coating onto the surfaces of MNPs was shown to result in stable aqueous suspensions from which the CS-coated MNPs were not separated. These features could be related to the increased hydrophilic nature of the CS-coated MNPs, which is expected to result in an extensive H-bonding between the CS-coated MNPs and the surrounding aqueous medium. These considerations are expected to result in a persistent stable suspension that resists forced precipitation by centrifugal forces. These features were more evident with increasing the concentration of CS in the coating. Accordingly, a CS-MNPs in which [CS] amounted to 0.5 wt% was selected for further functionalization with crocetin, which was confirmed by a detailed analysis of their weight loss data, as shown in Figure 25.

3.3 Crocetin Loading Characterization

Crocetin was chemically attached to the optimally prepared PEG- and CS-coated MNPs using EDCI-HCl as a crosslinker. Due to the sensitivity of the binding reaction to moisture, both crocetin and EDCI were added in excess of 20, 10, and 5 times more than the theoretically calculated concentration of crocetin needed to bind to the functional groups available on the surface of both 0.5% CS-coated MNPs and the 12% PEG-coated MNPs. The amount of available functional groups was calculated based on the amount of polymer loaded onto the surfaces of the MNPs. This amount was, in turn, estimated from the weight loss results of the optimally prepared PEG- and CS-coated MNPs, using their TGA thermograms, as shown in Figures 17 and 25, respectively. Therefore, the functionalization of both coated MNPs systems was attempted using three different concentrations of crocetin. Accordingly, PEG-coated MNPs were further functionalized by 5x, 10x, and 20x, giving rise to the

corresponding sample identifications: 5X-Cro-PEG-MNPs, 10X-Cro-PEG-MNPs, and 20X-Cro-PEG-MNPs. Similarly, the functionalization of CS-coated MPNs was also attempted using the same percentages of crocetin, giving rise to the corresponding sample identifications: 5X-Cro-CS-MNPs, 10X-Cro-CS-MNPs, and 20X-Cro-CS-MNPs. The following sections study the proposed binding mechanism of crocetin to both systems and the characterization of the crocetin-functionalized CS- and PEG-coated MNPs.

3.3.1 Characterization of Cro-Functionalized PEG-Coated MNPs

The FT-IR spectra of all Cro-functionalized PEG-coated MNPs are presented in Figure 28. A spectrum of pure crocetin was also included for comparison. Bands appearing at 430, 584, and 622 cm^{-1} in all spectra, that are attributed to the MNPs, were observed with decreased intensities than those of pure MNPs. This could be attributed to the effect of increased coating thickness on the IR absorption of the magnetic core. In addition, the FT-IR spectrum of pure crocetin showed several characteristic bands including. A band was observed at 3432 cm^{-1} , which is attributed to the hydroxyl group of crocetin. Other bands at 2921, 1463, and 1376 cm^{-1} for -CH, 1728 cm^{-1} band for carbonyl group (C=O), 1623 cm^{-1} for C=C group, and 1071 cm^{-1} for C-O sugar groups (Mir et al., 2020). In the crocetin functionalized PEG-coated MNPs we observed the appearance of the band corresponding to C=C at 1071 cm^{-1} , which confirms the presence of crocetin on PEG-MNPs, while other bands were not observed. This could be attributed to the thinning of the crocetin layer on the coating.

The TGA thermograms of the Cro-functionalized PEG-coated MNPs are shown in Figure 29, where two major thermal events were observed. The first weight-loss event was observed at around 100°C corresponding to the loss of physically and

chemically absorbed water, while the second thermal event was observed at around 250°C, and is attributed to the thermal decomposition of PEG. In contrast, the TGA thermogram of pure crocetin showed two major thermal events, the first about 200 ± 10 °C and the second around 300 ± 10 °C, as shown in Figure 30. These events are attributed to the degradation and decomposition of the crocetin molecule, respectively. The weight loss of crocetin overlaps with that of PEG and was thus reflected as a single thermal event in the thermograms of the crocetin-functionalized PEG-coated MNPs. Moreover, since all 20X, 10X, and 5X were prepared from the same batch of 12% PEG-MNPs and by assuming all MNPs are coated with the same amount of PEG, in this case, the difference in weight loss we observe in Figure 29 is attributed to the different loaded amounts of crocetin functionality of the PEG-coated MNPs. In addition, it was observed that the overall weight loss was linearly increased with increasing the proportion of crocetin in the sample. It has been proven, therefore, that the sample containing 20X concentration of crocetin contained the highest amount of crocetin loading followed by 10X and lastly 5X.

The possible binding mechanism of crocetin to PEG is illustrated in Figure 31. Crocetin will first react with EDC.HCl to activate the carboxylic acid group in crocetin. The carbonyl in the carboxylic acid targets the carbodiimide in EDC to form an active O-acylisourea intermediate that is easily displaced by a nucleophilic attack. The hydroxyl group in the PEG will serve that purpose and act as a nucleophile which will then bind to crocetin and give urea as a byproduct. In addition to this mechanism, it is also postulated that crocetin and PEG have the affinity to interact with each other through the formation of H-bonding across their functional groups.

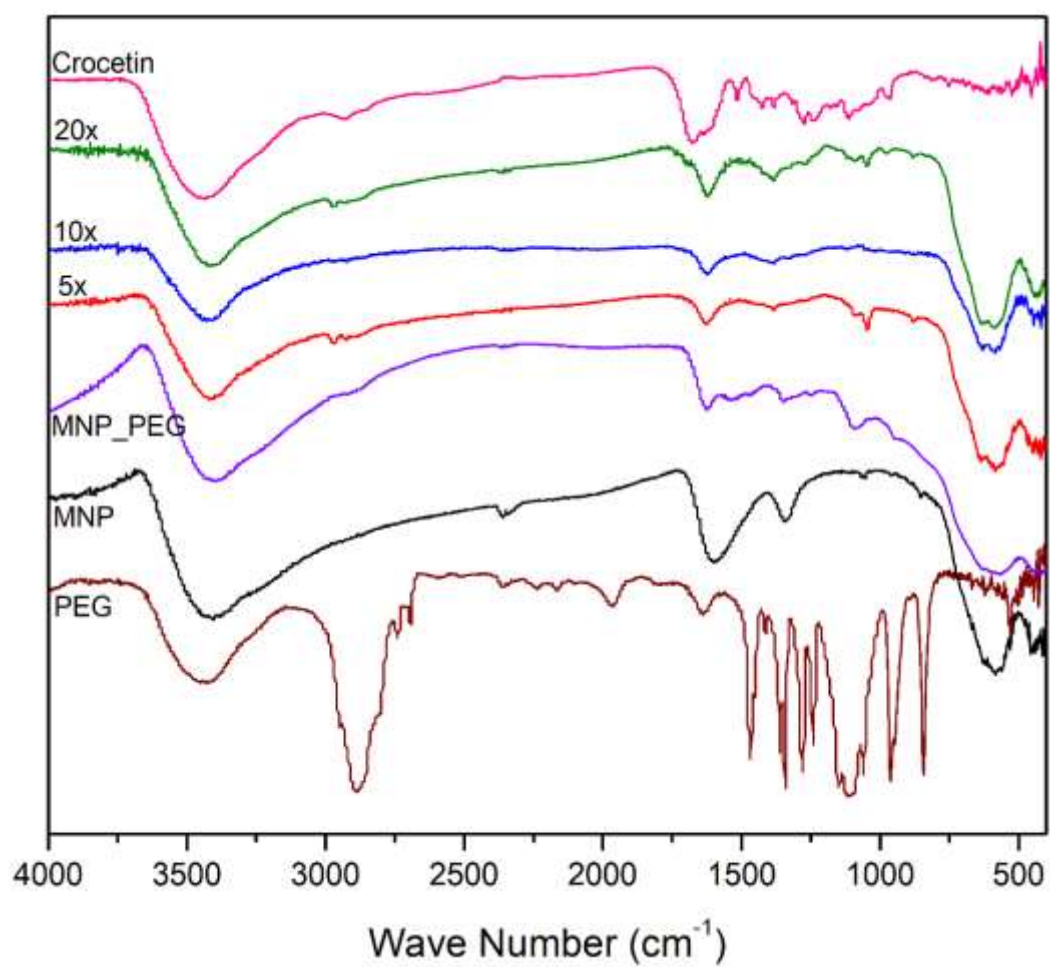


Figure 28: FTIR spectra of the crocetin-functionalized PEG-coated MNPs as a function of the concentration of crocetin

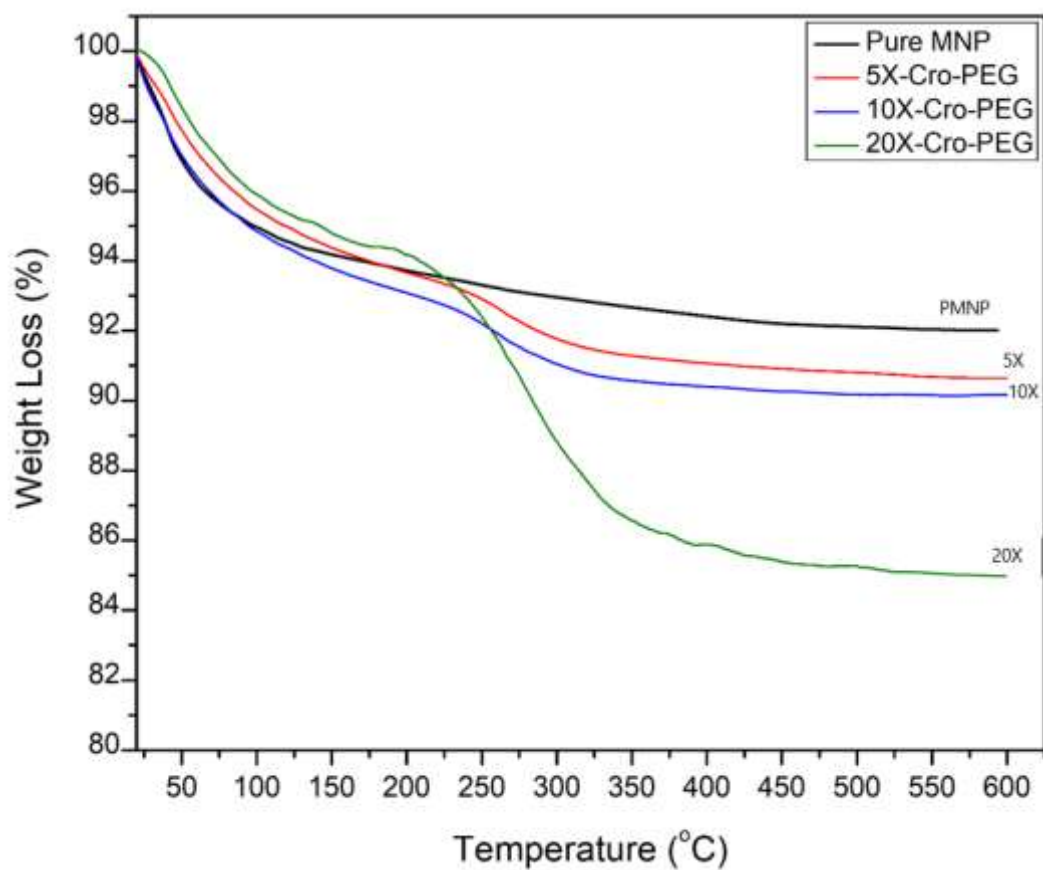


Figure 29: TGA thermograms of the crocetin-functionalized PEG-coated MNPs as a function of the concentration of crocetin

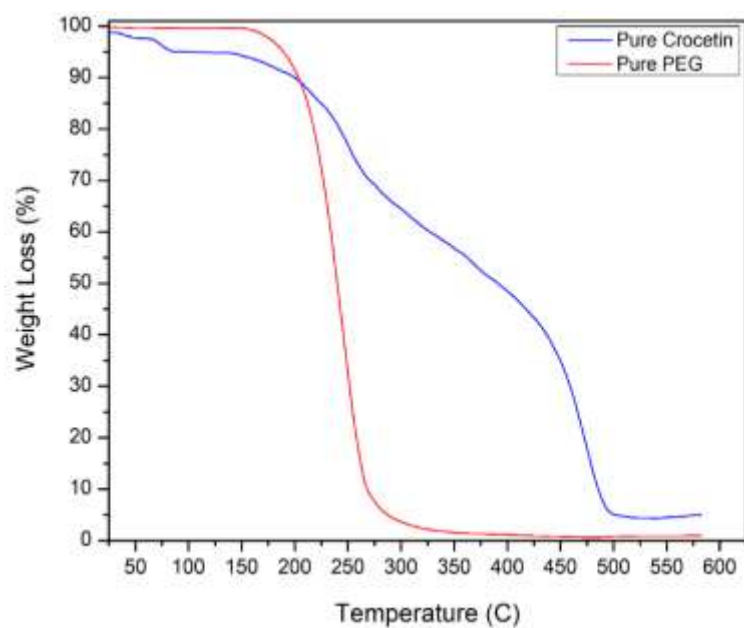


Figure 30: TGA thermograms of pure PEG and pure crocetin

The loading capacity of crocetin was derived from the amount of unbound crocetin in the aliquot of the crocetin binding procedure. The aliquot was collected and diluted with a known amount of DMSO then analyzed by UV-Visible spectrophotometer at 430 nm to estimate the remaining un-bound crocetin. A calibration curve of crocetin in DMSO was used to calculate the amount of unbound crocetin. By calculating the difference of the initial amount of crocetin added to PEG-coated MNPs and the amount in the aliquot, we have an estimate of the loading capacity, as presented in Table 1.

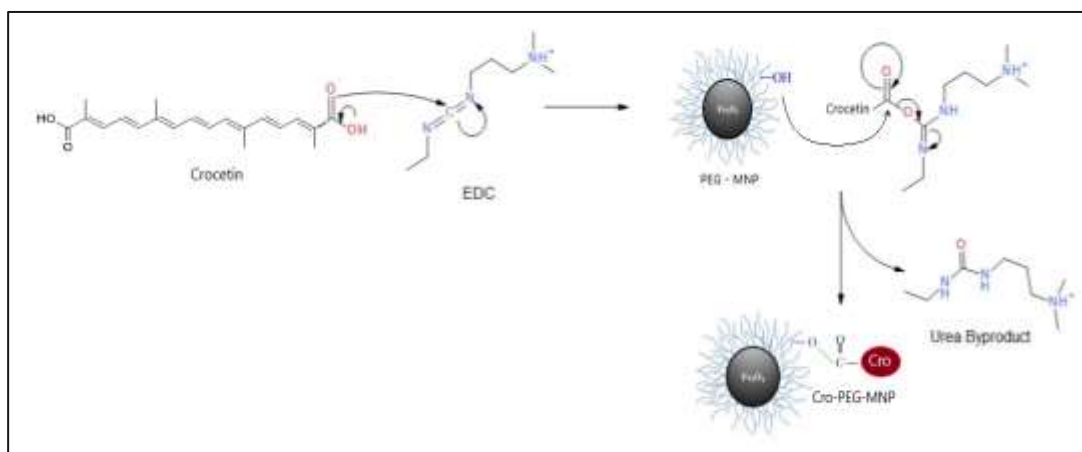


Figure 31: Schematic representation of the possible binding mechanism of crocetin to PEG-MNPs

Table 1: Loading capacity of Crocetin functionalized PEG-MNPs

Cro-PEG-MNP	Initial Amount of Crocetin	Amount of Crocetin Loaded	Loading Capacity (%)
5X-Cro-PEG-MNP	4.9 mg	4.7155 mg	96
10X-Cro-PEG-MNP	9.8 mg	8.57 mg	87
20X-Cro-PEG-MNP	19.6 mg	17.7 mg	90

3.3.2 Characterization of Cro-Functionalized CS-Coated MNPs

The FT-IR spectra of crocetin functionalized CS-coated MNPs are presented in Figure 32. In addition, spectra of 0.5% CS-MNPs, pure MNPs, pure chitosan, and pure crocetin were added for comparison. The effect of crocetin on the CS-coated MNPs is evident in the shifting of C=O bending vibrations from 1655 cm^{-1} in CS-MNPs to 1728 cm^{-1} . This could be due to the interaction between chitosan and crocetin, possibly through H-bonding formation. Another evidence of crocetin coating is the formed shoulder band at 1082 cm^{-1} that corresponds to crocetin C-O. Moreover, a weak band was observed at 1382 cm^{-1} that represents C-N bending vibrations in Cro-functionalized CS-coated MNPs. The shifting and weak intensity of chitosan and crocetin peaks in crocetin functionalized CS-coated MNPs samples indicate the physical and chemical interaction between the functional groups in chitosan and crocetin.

The TGA thermograms in Figure 33 illustrate the thermal events of the crocetin-functionalized CS-coated MNPs. A thermogram of pure MNPs was also added for comparison. In addition, Figure 34 shows TGA thermograms of pure chitosan and crocetin for comparison. Two major thermal events were observed. The first thermal event was observed around 100°C and corresponds to the removal of the physically and chemically absorbed water. It should be mentioned that the amount of water removed from pure MNPs was higher than that observed in the functionalized MNPs. This can be a result of the presence of CS and crocetin layers onto the MNPs, which delay the extent of the formation of a hydrated layer. The second major thermal event was observed around $250\pm 50^{\circ}\text{C}$ and is attributed to the degradation and thermal decomposition of both crocetin and chitosan coatings. By comparing the final weight

loss of all three Cro-functionalized CS-coated MNPs samples, a greater weight loss was observed for the 20X and 10X compared to the 5X. From that, it has been concluded that the amount of loaded crocetin in the 20X and 10X is more than 5X. Furthermore, the weight loss difference between 20X and 10X is not significant, indicating the maximum amount of crocetin loading onto the CS coating was 10X.

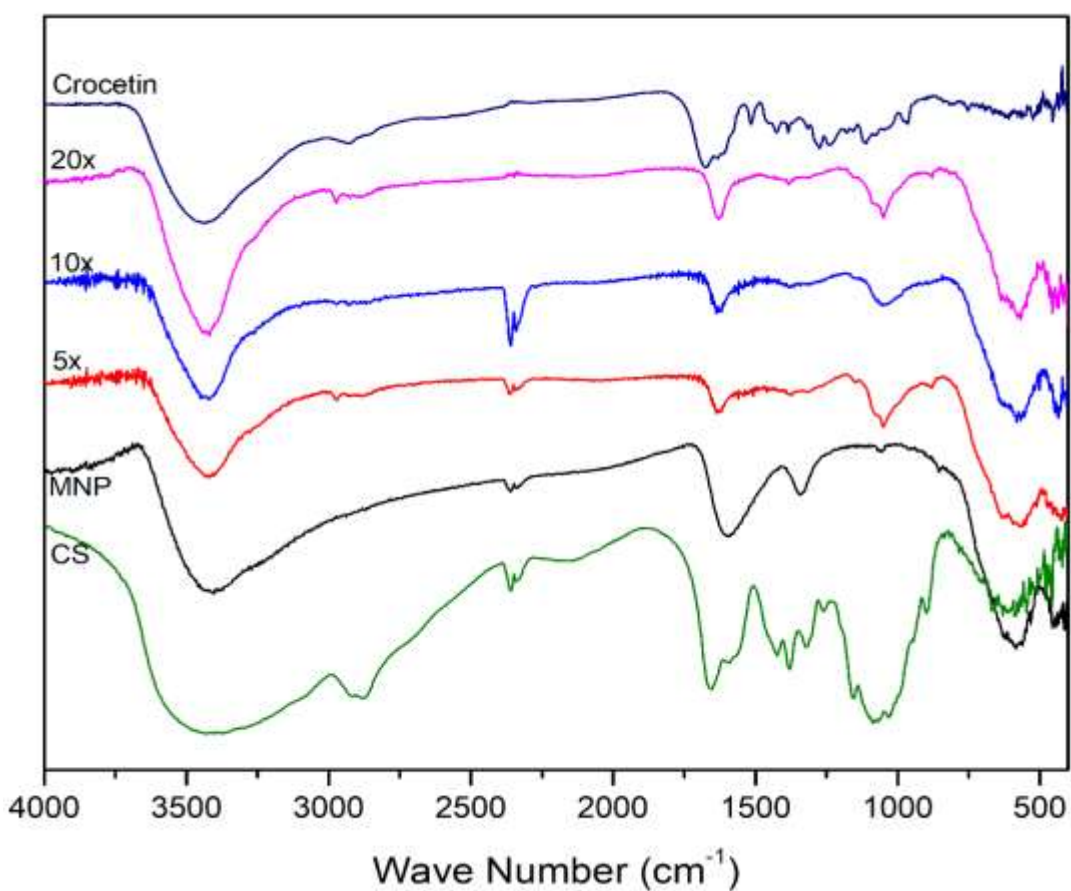


Figure 32: FTIR spectra of the crocetin-functionalized chitosan-coated MNPs as a function of the concentration of crocetin

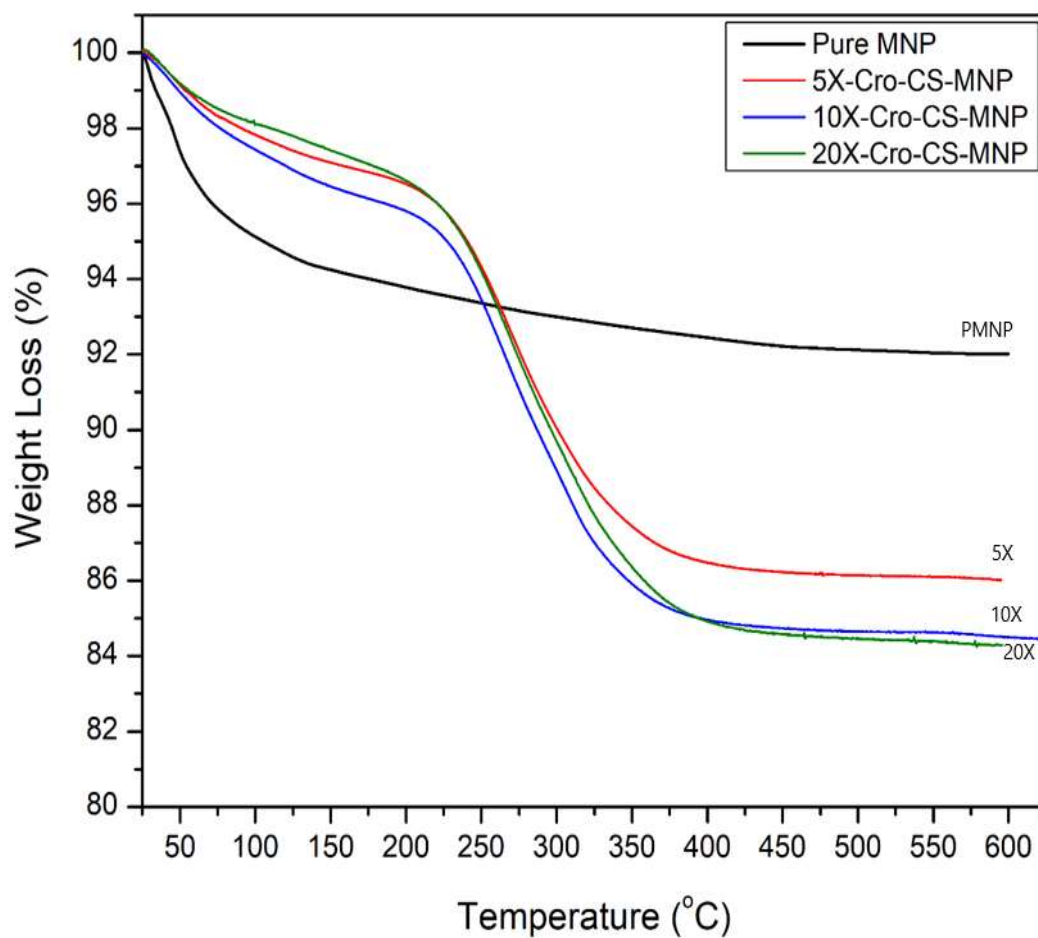


Figure 33: TGA thermograms of the crocetin-functionalized chitosan-coated MNPs as a function of the concentration of crocetin

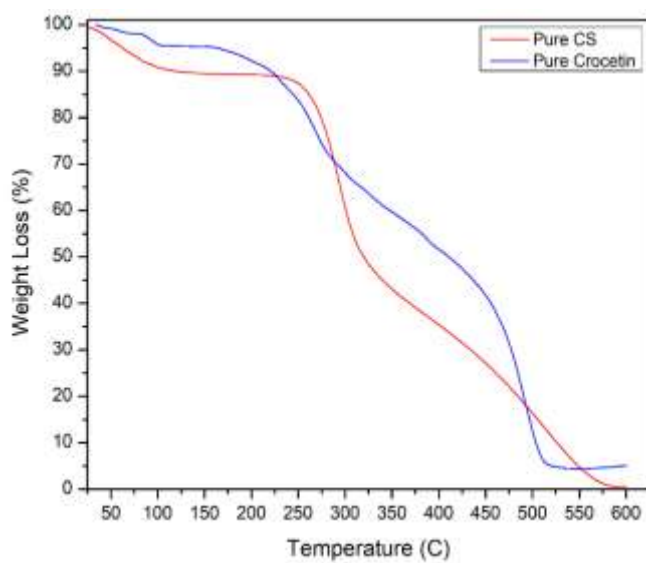


Figure 34: TGA thermograms of pure chitosan and pure crocetin

The possible binding mechanism of crocetin to chitosan is illustrated in Figure 35. As mentioned in the previous section, crocetin is expected to initially react with EDC.HCl to activate the carboxylic acid group in crocetin. The carbonyl in the carboxylic acid targets the carbodiimide in EDC to form an active O-acylisourea intermediate that is easily displaced by a nucleophilic attack. There are several functional groups in chitosan that can act as a nucleophile. These include primary and secondary hydroxyl groups as well as the amino group. Each of the mentioned groups can form a bond with the carboxylic acid to give crocetin-functionalized CS-coated MNPs. The priority of bond formation will favor the amide bond formation followed by secondary hydroxyl because it's more terminal which means less steric hindrance and finally the primary hydroxyl. The byproduct of this reaction is urea. Other possible binding interactions will include hydrogen bonding between the hydrophilic groups along with the chitosan coating and the terminal carboxyl groups in the crocetin functionality.

The loading capacity percentages shown in Table 2 confirm those observed from the TGA thermograms of the same samples. The loading capacity of both 5X and 10X was above 90%, while the loading capacity of the 20X loading capacity was around 70%, indicating 30% of the crocetin added was in the aliquot.

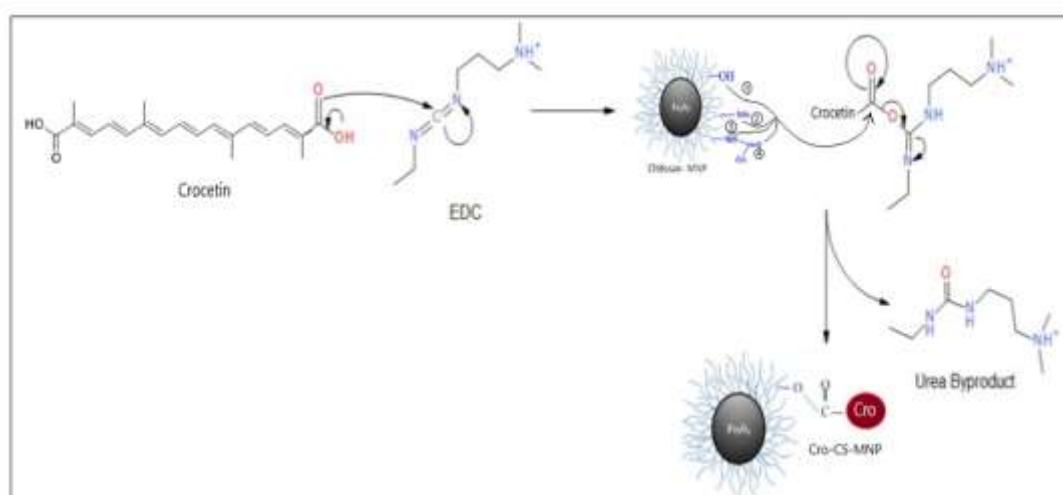


Figure 35: Schematic representation of the possible binding mechanism of crocetin to Chitosan-MNPs

Table 2: Loading capacity of Crocetin functionalized CS-MNPs

Cro-CS-MNP	Initial Amount of Crocetin	Amount of Crocetin Loaded	Loading Capacity (%)
5X-Cro-CS-MNP	0.787mg	0.715mg	94
10X-Cro-CS-MNP	1.57mg	1.426mg	91
20X-Cro-CS-MNP	3.14mg	2.21 mg	70

3.4 Kinetic Release Study of Crocetin

The cumulative release of crocetin from the prepared PEG- and CS-coated MNPs was investigated at pH values of 5.6 and 7.4, while both were kept at a physiologic temperature of 37°C. The lower pH value of 5.6 was selected to simulate the slightly acidic nature of a cancer site, while the pH of 7.4 was selected to simulate the physiologic environment. The cumulative drug release was expressed as the percentage of detached crocetin from the PEG- and CS-coated MNPs as released to the surrounding aqueous media as a function of time. The drug release activity depends

on many characteristics of the NPs, such as surface characteristics and forces of interaction between crocetin and the underlying coating onto the surfaces of the MNPs.

Figures 36-38 show the cumulative release (%) of crocetin from the crocetin-functionalized PEG-coated MNPs at pH 7.4 and pH 5.6 as a function of the concentration of crocetin. Figure 36 shows the 5X-Cro-PEG-MNPs cumulative release. A burst effect was observed in the first 6 hours, as was previously reported in the literature (Hafezi Ghahestani et al., 2017; Soltani et al., 2017). Within the first 6 hours, 25% of crocetin was released at pH 7.4, while 22% of crocetin was released at pH 5.6. This stage was followed by a slower release stage at both pH values. At the end of the 3 days testing period, the total release of crocetin for pH 5.6 was 38% while the total release was 50% at pH 7.4. Figure 37 shows the release of 10X crocetin functionalized PEG-coated MNPs. At this concentration, a different trend was observed as a function of the pH of the medium. A burst effect was also observed within the first 6 hours for pH 5.6 with a release of 25% of crocetin, while at pH 7.4, 60% was released. This stage was also followed by a slower stage at both pH values.

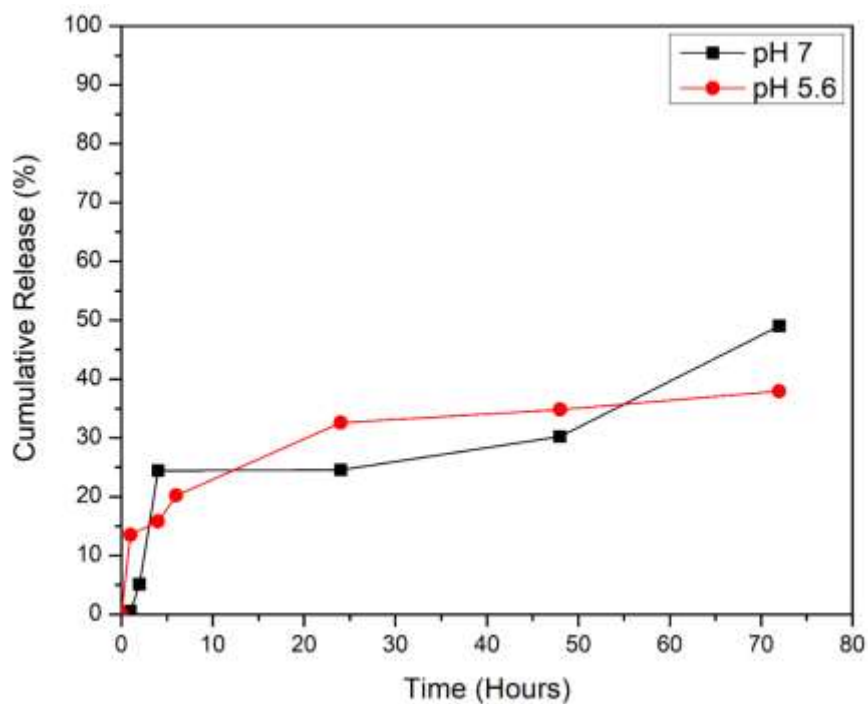


Figure 36: Cumulative release study of crocetin (5x) from crocetin-functionalized PEG-coated MNPs at different pH values

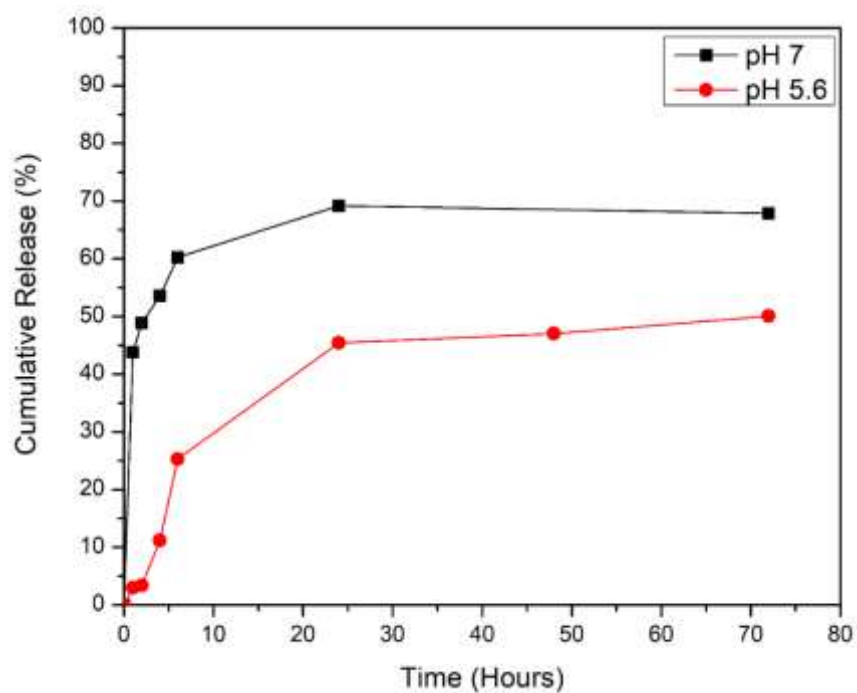


Figure 37: Cumulative release study of crocetin (10x) from crocetin-functionalized PEG-coated MNPs at different pH values

At the end of the 72 hours testing period the total cumulative release for pH 5.6 was 48% and for pH 7.4 was 70%. Similarly, Figure 38 presents the release of 20X crocetin-functionalized PEG-coated MNPs. The burst effect reached the maximum after 6 hours with pH 7.4 almost 100% of crocetin was released. On the other hand, only 47% was released of crocetin for the same period at pH 5.6. At the end of the testing period, 72% of crocetin was released at pH 5.6 and 100% of crocetin was released at pH 7.4.

For crocetin functionalized CS-coated MNPs samples, no release was observed for all tested samples including 20X, 10X, and 5X at both pH 5.6 and 7.4 values even at the end of the 72 hours testing period. This can be due to multiple bonds formation between crocetin and the underlying chitosan structure. Figure 39 shows a comparison of the percentage cumulative release of all samples at pH 5.6. All Cro-PEG-MNPs samples experience burst release in the first 6 hours. This could be due to the loss of hydrogen bonding and dispersion forces between crocetin and the underlying PEG coating, resulting in the release of crocetin into PBS. After that, the release becomes slower and more stable. We observe higher amounts of crocetin released corresponding to the higher amount initially present in the crocetin functionalized PEG-coated MNPs. For example, the total percentage of crocetin released in pH 5.6 for the 20X is 72% compared to 48% for the 10X and finally 25% for the 5X. While for CS-coated MNPs we observe no release in all three samples. Figure 40 shows a comparison between the different samples at pH 7.4. We observe a higher release of crocetin from the PEG-coated MNPs in 20X than 10X, as compared to that of the 5X sample. Overall, it is evident that the burst effect is consistent in the first 6 hours, and at the end of the 72 hours testing period almost 100% was released from the 20X

sample, 70% released from the 10X, and 50% released from the 5X. On the contrary, crocetin bound to the CS-coated MNPs showed no release for all the tested samples.

The release of crocetin was generally higher in pH 7.4 than pH 5.6. This might be attributed to the increase of cleavage or hydrolysis of carboxylic esters linkage bond between crocetin and PEG at pH 7.4 compared to pH 5.6. In acidic conditions, we have a higher concentration of H^+ , which may indicate a weaker probability of hydrophilic attacks on the carboxylic ester group between crocetin and the underlying PEG coating. This indicates a lower extent of hydrolysis, hence less crocetin was released.

It should be mentioned that the release of crocetin is followed by the degradation of the PEG coating and the subsequent degradation of the MNPs into free iron ions that bind to ferritin protein in the cells. Because of the leaky and pre-mature blood vessels of cancer tissues, the chance of crocetin-functionalized PEG-coated MNPs accumulating inside these tissues by passive targeting will be higher than normal tissues. Consequently, this will increase the hydrolysis and release of crocetin to the cancer microenvironment. Based on these results, crocetin-functionalized PEG-coated MNPs were selected for the study of their *in vitro* cytotoxicity against hepatocellular carcinoma cells.

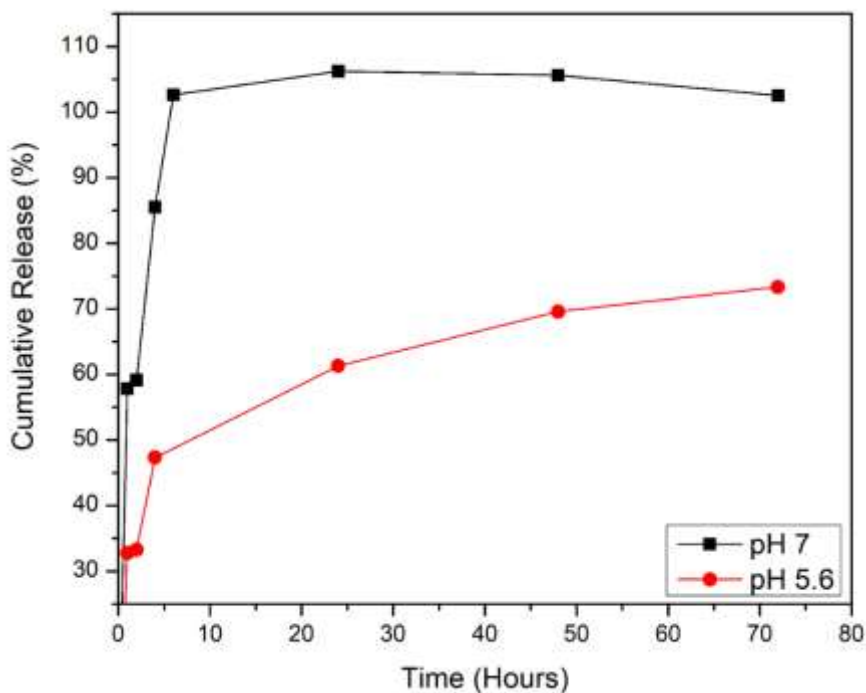


Figure 38: Cumulative release study of crocetin (20x) from crocetin-functionalized PEG-coated MNPs at different pH values

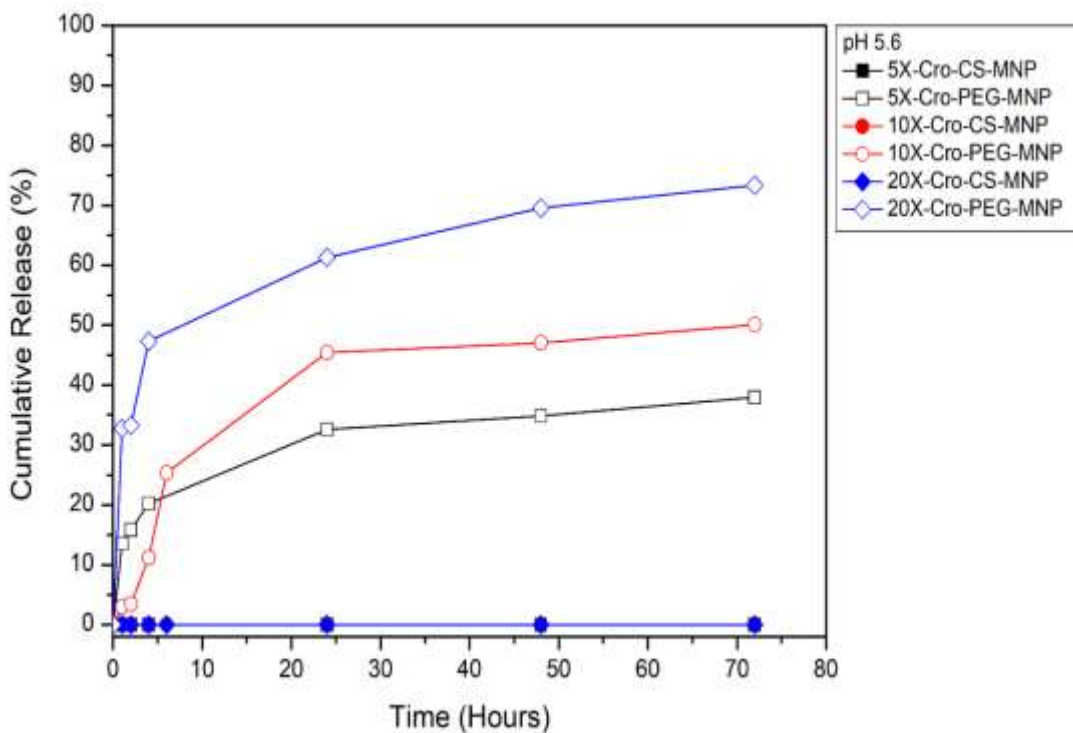


Figure 39: Cumulative release study of crocetin (5x) from crocetin-functionalized chitosan-coated and PEG-coated MNPs at pH 5.6

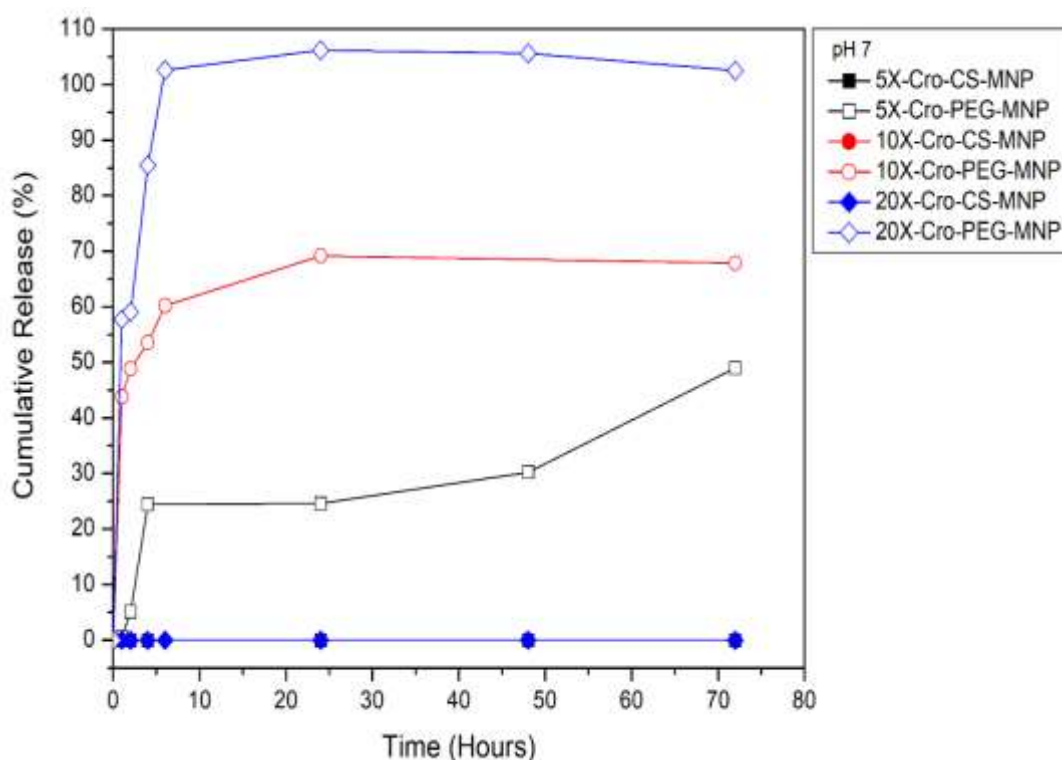


Figure 40: Cumulative release study of crocetin (5x) from crocetin-functionalized chitosan-coated and PEG-coated MNPs at pH 7.0

3.5 Preliminary In-Vitro Cytotoxicity

In this study, a human hepatocellular carcinoma cell line HepG2 was selected as a model of cancer cells for the preliminary *in vitro* study. Cell proliferation and viability were evaluated by MTT assay. HepG2 cells were incubated for 24 and 72 hours at 4 different concentrations of 20X, 10X, and 5X crocetin-functionalized PEG-coated MNPs including 0.05, 0.5, 3, and 5 mg/ml as well as free crocetin as the control.

Figures 41-42 show the MTT assay after 24 and 72 hours of HepG2 cells treated with free crocetin. Results show a reduction in the cell viability with increasing the concentration of crocetin. Furthermore, Figures 43-44 shows the cell viability results of crocetin functionalized PEG-coated MNPs at different concentrations

including 0.05, 0.07, 0.09 and 0.1 mg/ml. Pure MNPs and PEG-MNPs were also tested as control samples. In the 24 hours cell viability assay, the as-prepared MNPs exhibited a toxic effect reducing the cell viability, as compared with PEG-coated MNPs. The reduced toxicity in PEG-MNPs can indicate that coating has limited the nonspecific cell interactions, as compared to the as-prepared MNPs (Santos et al., 2016). The same observation was also observed in the 72 hours incubation period. In general, the proliferation of HepG2 cells showed a decrease with the increasing dose of each Cro-PEG-MNPs concentration.

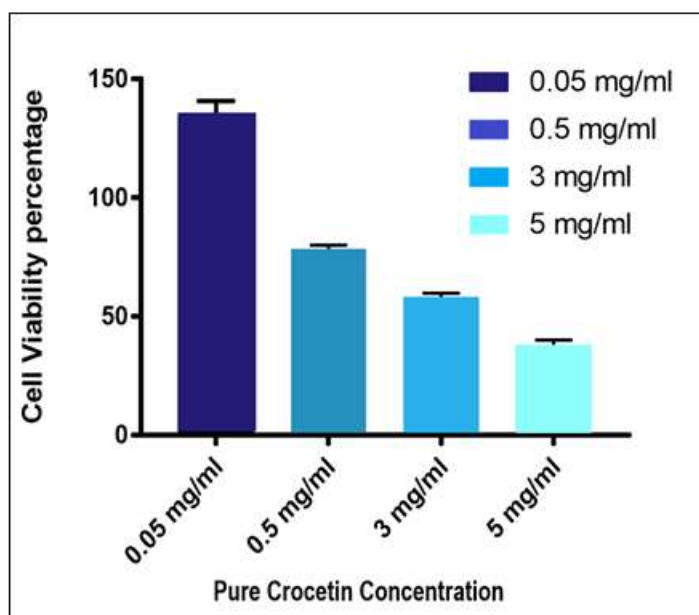


Figure 41: Cell viability of HepG2 cells against pure crocetin as a function of the concentration of crocetin after 24 hours of culture at 37°C

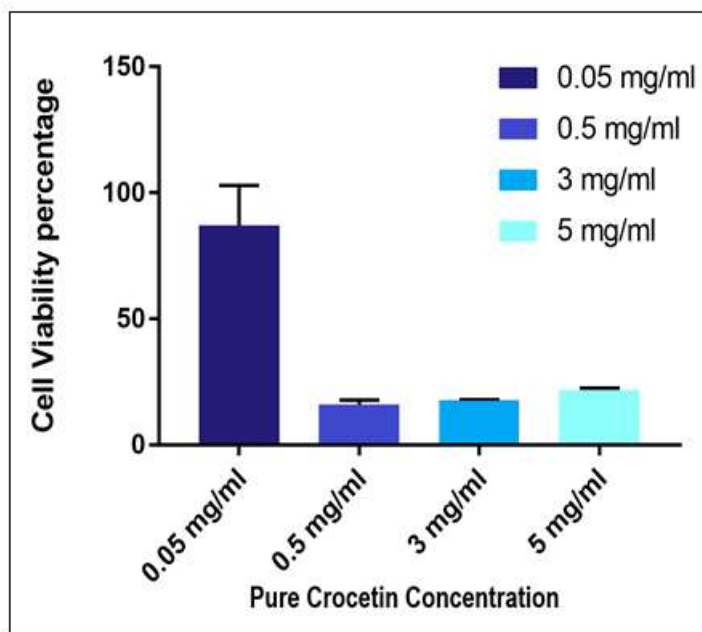


Figure 42: Cell viability of HepG2 cells against pure crocetin as a function of the concentration of crocetin after 72 hours of culture at 37°C

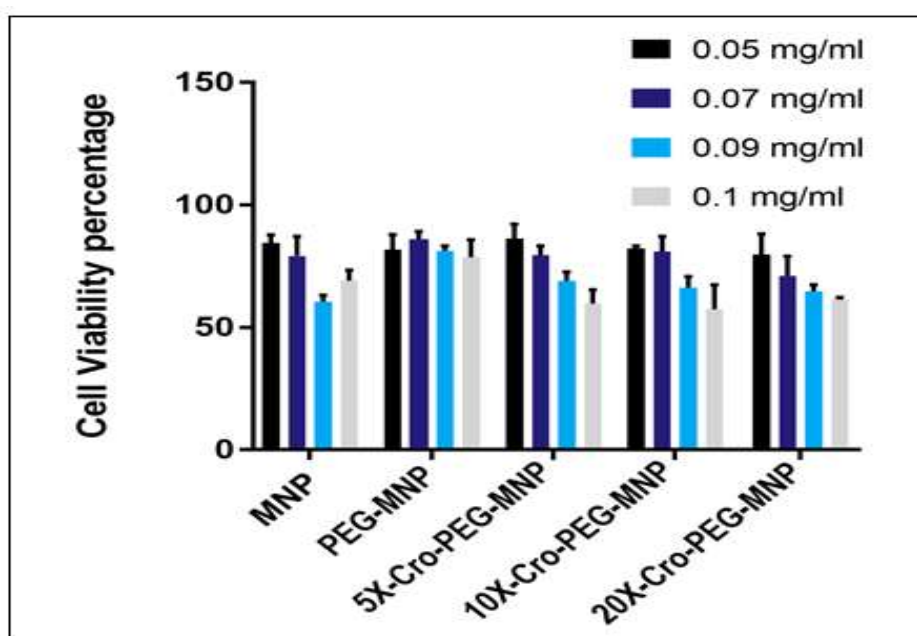


Figure 43: Cell viability of HepG2 cells against crocetin-functionalized PEG-coated MNPs as a function of the concentration of crocetin after 24 hours of culture at 37°C

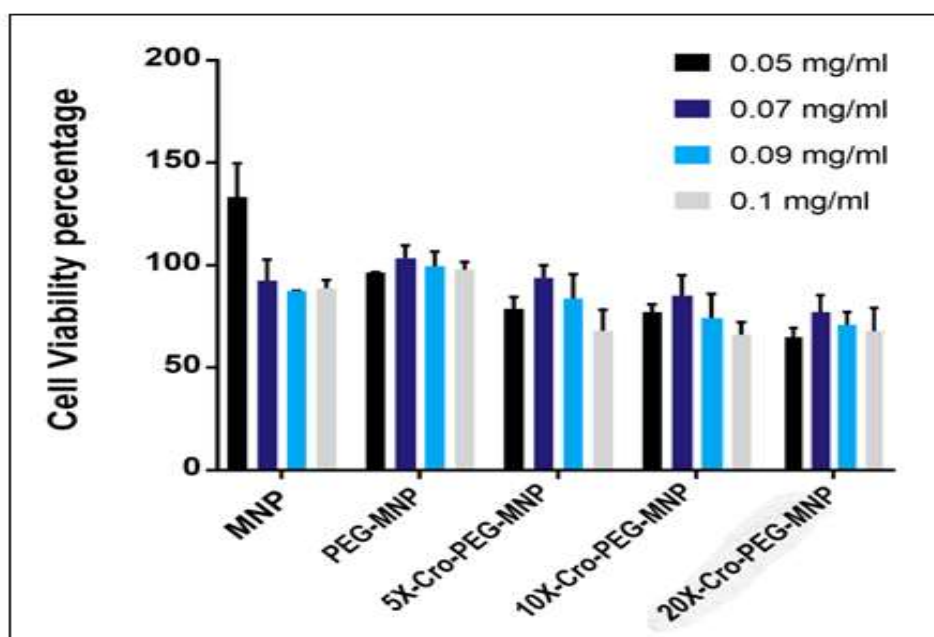


Figure 44: Cell viability of HepG2 cells against crocetin-functionalized PEG-coated MNPs as a function of the concentration of crocetin after 72 hours of culture at 37°C

Chapter 4: Conclusion

Cancer is the number one enemy of life. HCC to this day is considered one of the most difficult cancers to treat. This creates the need for more research to be done in the diagnostics and treatment of HCC. Targeted therapy via nanoscience offers many possibilities which could enhance the conventional way of diagnosing and treating cancer. In this thesis, we present the fabrication of a targeted nanoparticle system for the treatment of HCC, the most common type of liver cancer. The carrier system is composed of crocetin functionalized PEG-coated magnetite nanoparticles. Crocetin is a natural extract of Saffron known for its anti-cancer activity. PEG is a synthetic polymer known for its biocompatibility and biodegradability. The core of this system is magnetite nanoparticles known for its many desirable qualities including superparamagnetism which makes the targeting possible via an external magnet. Together they form a delivery system that shows good release kinetics in tumor acidic media based on the in-vitro release kinetics results and have the potential to reduce cell proliferation of HepG2 liver cancer cell line based on the preliminary in-vitro cytotoxicity results.

Chapter 5: Future Work and Limitations

Future work would be testing the designed Cro-PEG-MNPs *in vivo*. The nanodrug carrier system will be injected *in vivo*. The tumor will be subjected to a localized magnetic field to retain the delivery system inside the tumor microenvironment. After the drug is released the bare MNPs will be used for further treatment with hyperthermia. Another plan is to see the synergistic effect of crocetin conjugated with a commercial cancer drug.

References

- Ali, E. M. M., Elashkar, A. A., El-Kassas, H. Y., & Salim, E. I. (2018). Methotrexate loaded on magnetite iron nanoparticles coated with chitosan: Biosynthesis, characterization, and impact on human breast cancer MCF-7 cell line. *International Journal of Biological Macromolecules*, *120*, 1170–1180. <https://doi.org/10.1016/j.ijbiomac.2018.08.118>
- Anirudhan, T. S., & Binusreejayan. (2016). Dextran based nanosized carrier for the controlled and targeted delivery of curcumin to liver cancer cells. *International Journal of Biological Macromolecules*, *88*, 222–235. <https://doi.org/10.1016/j.ijbiomac.2016.03.040>
- Arachchige, M. P., Laha, S. S., Naik, A. R., Lewis, K. T., Naik, R., & Jena, B. P. (2017). Functionalized nanoparticles enable tracking the rapid entry and release of doxorubicin in human pancreatic cancer cells. *Micron*, *92*, 25–31. <https://doi.org/10.1016/j.micron.2016.10.005>
- Baig, B., Halim, S. A., Farrukh, A., Greish, Y., & Amin, A. (2019). Current status of nanomaterial-based treatment for hepatocellular carcinoma. In *Biomedicine and Pharmacotherapy* (Vol. 116, p. 108852). Elsevier Masson SAS. <https://doi.org/10.1016/j.biopha.2019.108852>
- Bhandari, P. R. (2015). Crocus sativus L. (saffron) for cancer chemoprevention: A mini review. In *Journal of Traditional and Complementary Medicine* (Vol. 5, Issue 2, pp. 81–87). <https://doi.org/10.1016/j.jtcme.2014.10.009>
- Bialecki, E. S., & Di Bisceglie, A. M. (2005). Diagnosis of hepatocellular carcinoma. *Hpb*, *7*(1), 26–34. <https://doi.org/10.1080/13651820410024049>
- Boskabady, M., & Farkhondeh, T. (2016). Antiinflammatory, Antioxidant, and Immunomodulatory Effects of Crocus sativus L. and its Main Constituents. *Phytotherapy Research*, *30*(7), 1072–1094.
- Brigger, I., Dubernet, C., & Couvreur, P. (2012). Nanoparticles in cancer therapy and diagnosis. *Advanced Drug Delivery Reviews*, *64*(SUPPL.), 24–36. <https://doi.org/10.1016/j.addr.2012.09.006>
- Capek, I. (2019). Nanotechnology and nanomaterials. *Nanocomposite Structures and Dispersions*, 1–93. <https://doi.org/10.1016/b978-0-444-63748-2.00001-8>
- Cerqueira, B. B. S., Lasham, A., Shelling, A. N., & Al-Kassas, R. (2017). Development of biodegradable PLGA nanoparticles surface engineered with hyaluronic acid for targeted delivery of paclitaxel to triple negative breast cancer cells. *Materials Science and Engineering C*, *76*, 593–600. <https://doi.org/10.1016/j.msec.2017.03.121>
- Chakraborty, S., & Rahman, T. (2012). The difficulties in cancer treatment. *Ecancermedicalscience*, *6*, ed16. <https://doi.org/10.3332/ecancer.2012.ed16>

- Chin, A. B., & Yaacob, I. I. (2007). Synthesis and characterization of magnetic iron oxide nanoparticles via w/o microemulsion and Massart's procedure. *Journal of Materials Processing Technology*, 191(1–3), 235–237. <https://doi.org/10.1016/j.jmatprotec.2007.03.011>
- Dudley, A. C. (2012). Tumor endothelial cells. *Cold Spring Harbor Perspectives in Medicine*, 2(3), 1–18. <https://doi.org/10.1101/cshperspect.a006536>
- Dyawanapelly, S., Jagtap, D. D., Dandekar, P., Ghosh, G., & Jain, R. (2017). Assessing safety and protein interactions of surface-modified iron oxide nanoparticles for potential use in biomedical areas. *Colloids and Surfaces B: Biointerfaces*, 154, 408–420. <https://doi.org/10.1016/j.colsurfb.2017.03.050>
- El-Kharrag, R., Amin, A., Hisaindee, S., Greish, Y., & Karam, S. M. (2017). Development of a therapeutic model of precancerous liver using crocin-coated magnetite nanoparticles. *International Journal of Oncology*, 50(1), 212–222. <https://doi.org/10.3892/ijo.2016.3769>
- Escobar Zapata, E. V., Martínez Pérez, C. A., Rodríguez González, C. A., Castro Carmona, J. S., Quevedo Lopez, M. A., & García-Casillas, P. E. (2012). Adherence of paclitaxel drug in magnetite chitosan nanoparticles. *Journal of Alloys and Compounds*, 536(SUPPL.1), S441–S444. <https://doi.org/10.1016/j.jallcom.2011.12.150>
- Faraji, M., Yamini, Y., & Rezaee, M. (2010). Magnetic nanoparticles : synthesis , stabilization , functionalization , characterization , and applications. *JOURNAL OF THE Iranian Chemical Society*, 7(1), 1–37.
- Ferreira, R. V., Silva-Caldeira, P. P., Pereira-Maia, E. C., Fabris, J. D., Cavalcante, L. C. D., Ardisson, J. D., & Domingues, R. Z. (2016). Bio-inactivation of human malignant cells through highly responsive diluted colloidal suspension of functionalized magnetic iron oxide nanoparticles. *Journal of Nanoparticle Research*, 18(4). <https://doi.org/10.1007/s11051-016-3400-7>
- Fu, J., Jiang, X., Han, W., & Cao, Z. (2021). Enhancing the Cycling Stability of Transition-Metal-Oxide-Based Electrochemical Electrode via Pourbaix Diagram Engineering. *Energy Storage Materials*, 42(July), 252–258. <https://doi.org/10.1016/j.ensm.2021.07.037>
- Gans, J. H., Lipman, J., Golowa, Y., Kinkhabwala, M., & Kaubisch, A. (2019). Hepatic Cancers Overview: Surgical and Chemotherapeutic Options, How Do Y-90 Microspheres Fit in? *Seminars in Nuclear Medicine*, 49(3), 170–181. <https://doi.org/10.1053/j.semnuclmed.2019.01.001>
- Gonzalez-valdivieso, J., Girotti, A., Schneider, J., & Javier, F. (2021). Advanced nanomedicine and cancer : Challenges and opportunities in clinical translation. *International Journal of Pharmaceutics*, 599, 120438. <https://doi.org/10.1016/j.ijpharm.2021.120438>

- Griffin, S., Masood, M. I., Nasim, M. J., Sarfraz, M., Ebokaiwe, A. P., Schäfer, K. H., Keck, C. M., & Jacob, C. (2018). Natural nanoparticles: A particular matter inspired by nature. *Antioxidants*, 7(1), 1–21. <https://doi.org/10.3390/antiox7010003>
- Hafezi Ghahestani, Z., Alebooye Langroodi, F., Mokhtarzadeh, A., Ramezani, M., & Hashemi, M. (2017). Evaluation of anti-cancer activity of PLGA nanoparticles containing crocetin. *Artificial Cells, Nanomedicine and Biotechnology*, 45(5), 955–960. <https://doi.org/10.1080/21691401.2016.1198359>
- Han, Y., Gao, Y., Cao, X., Zangeneh, M. M., Liu, S., & Li, J. (2020). Ag NPs on chitosan-alginate coated magnetite for synthesis of indazolo[2,1-b]phthalazines and human lung protective effects against α -Guttiferin. *International Journal of Biological Macromolecules*, 164, 2974–2986. <https://doi.org/10.1016/j.ijbiomac.2020.08.183>
- Handali, S., Moghimipour, E., Rezaei, M., Ramezani, Z., Kouchak, M., Amini, M., Angali, K. A., Saremy, S., & Dorkoosh, F. A. (2018). A novel 5-Fluorouracil targeted delivery to colon cancer using folic acid conjugated liposomes. *Biomedicine and Pharmacotherapy*, 108(July), 1259–1273. <https://doi.org/10.1016/j.biopha.2018.09.128>
- Jović Orsini, N., Babić-Stojić, B., Spasojević, V., Calatayud, M. P., Cvjetićanin, N., & Goya, G. F. (2018). Magnetic and power absorption measurements on iron oxide nanoparticles synthesized by thermal decomposition of Fe(acac)₃. *Journal of Magnetism and Magnetic Materials*, 449, 286–296. <https://doi.org/10.1016/j.jmmm.2017.10.053>
- Kang, H., Hu, S., Cho, M. H., Hong, S. H., Choi, Y., & Choi, H. S. (2018). Theranostic nanosystems for targeted cancer therapy. *Nano Today*, 23, 59–72. <https://doi.org/10.1016/j.nantod.2018.11.001>
- Kayal, S., & Ramanujan, R. V. (2010). Doxorubicin loaded PVA coated iron oxide nanoparticles for targeted drug delivery. *Materials Science & Engineering C*, 30(3), 484–490. <https://doi.org/10.1016/j.msec.2010.01.006>
- Kesharwani, P., Banerjee, S., Padhye, S., Sarkar, F. H., & Iyer, A. K. (2015). Parenterally administrable nano-micelles of 3,4-difluorobenzylidene curcumin for treating pancreatic cancer. *Colloids and Surfaces B: Biointerfaces*, 132, 138–145. <https://doi.org/10.1016/j.colsurfb.2015.05.007>
- Khan, I., Saeed, K., & Khan, I. (2019). Nanoparticles: Properties, applications and toxicities. *Arabian Journal of Chemistry*, 12(7), 908–931. <https://doi.org/10.1016/j.arabjc.2017.05.011>
- Khmara, I., Molcan, M., Antosova, A., Bednarikova, Z., Zavisova, V., Kubovcikova, M., Jurikova, A., Girman, V., Baranovicova, E., Koneracka, M., & Gazova, Z. (2020). Bioactive properties of chitosan stabilized magnetic nanoparticles – Focus on hyperthermic and anti-amyloid activities. *Journal of Magnetism and Magnetic Materials*, 513(April), 167056. <https://doi.org/10.1016/j.jmmm.2020.167056>

- Kim, J., Hong, J., Lee, J., Lahiji, S. F., & Kim, Y.-H. (2021). Recent advances in tumor microenvironment-targeted nanomedicine delivery approaches to overcome limitations of immune checkpoint blockade-based immunotherapy. *Journal of Controlled Release*, 332(February), 109–126. <https://doi.org/10.1016/j.jconrel.2021.02.002>
- Kim, S. H., Lee, J. M., Kim, S. C., Park, C. B., & Lee, P. C. (2014). Proposed cytotoxic mechanisms of the saffron carotenoids crocin and crocetin on cancer cell lines. *Biochemistry and Cell Biology*, 92(2), 105–111. <https://doi.org/10.1139/bcb-2013-0091>
- Kim, T. H., Jiang, H. H., Youn, Y. S., Park, C. W., Tak, K. K., Lee, S., Kim, H., Jon, S., Chen, X., & Lee, K. C. (2011). Preparation and characterization of water-soluble albumin-bound curcumin nanoparticles with improved antitumor activity. *International Journal of Pharmaceutics*, 403(1–2), 285–291. <https://doi.org/10.1016/j.ijpharm.2010.10.041>
- Köçkar, H., Karaagac, O., & Özel, F. (2019). Effects of biocompatible surfactants on structural and corresponding magnetic properties of iron oxide nanoparticles coated by hydrothermal process. *Journal of Magnetism and Magnetic Materials*, 474(November 2018), 332–336. <https://doi.org/10.1016/j.jmmm.2018.11.053>
- Kubíčková, L., Koktan, J., Kořínková, T., Klementová, M., Kmječ, T., Kohout, J., Weidenkaff, A., & Kaman, O. (2020). Zn-substituted iron oxide nanoparticles from thermal decomposition and their thermally treated derivatives for magnetic solid-phase extraction. *Journal of Magnetism and Magnetic Materials*, 498(July 2019), 166083. <https://doi.org/10.1016/j.jmmm.2019.166083>
- Kuchma, E., Kubrin, S., & Soldatov, A. (2018). The local atomic structure of colloidal superparamagnetic iron oxide nanoparticles for theranostics in oncology. *Biomedicines*, 6(3). <https://doi.org/10.3390/biomedicines6030078>
- Kumar, S., Malik, M. M., & Purohit, R. (2018). Synthesis of high surface area mesoporous silica materials using soft templating approach. *Materials Today: Proceedings*, 5(2), 4128–4133. <https://doi.org/10.1016/j.matpr.2017.11.673>
- Lazaro-Carrillo, A., Filice, M., Guillén, M. J., Amaro, R., Viñambres, M., Tabero, A., Paredes, K. O., Villanueva, A., Calvo, P., del Puerto Morales, M., & Marciello, M. (2020). Tailor-made PEG coated iron oxide nanoparticles as contrast agents for long lasting magnetic resonance molecular imaging of solid cancers. *Materials Science and Engineering C*, 107(June 2019), 110262. <https://doi.org/10.1016/j.msec.2019.110262>
- Lei, Y., Tang, L., Xie, Y., Xianyu, Y., Zhang, L., Wang, P., Hamada, Y., Jiang, K., Zheng, W., & Jiang, X. (2017). Gold nanoclusters-assisted delivery of NGF siRNA for effective treatment of pancreatic cancer. *Nature Communications*, 8, 1–15. <https://doi.org/10.1038/ncomms15130>
- Li, J., Wang, S., Shi, X., & Shen, M. (2017). Aqueous-phase synthesis of iron oxide nanoparticles and composites for cancer diagnosis and therapy. *Advances in Colloid and Interface Science*, 249, 374–385. <https://doi.org/10.1016/j.cis.2017.02.009>

- Li, S., Jiang, S., Jiang, W., Zhou, Y., Shen, X. Y., Luo, T., Kong, L. P., & Wang, H. Q. (2015). Anticancer effects of crocetin in human esophageal squamous cell carcinoma KYSE-150 cells. *Oncology Letters*, 9(3), 1254–1260. <https://doi.org/10.3892/ol.2015.2869>
- Limeres, M. J., Moreton, M. A., Bernabeu, E., & Chiappetta, D. A. (2019). Thinking small , doing big : Current success and future trends in drug delivery systems for improving cancer therapy with special focus on liver cancer. *Materials Science & Engineering C*, 95(April 2018), 328–341. <https://doi.org/10.1016/j.msec.2018.11.001>
- Liu, Y., Zhou, J., Li, Q., Li, L., Jia, Y., Geng, F., Zhou, J., & Yin, T. (2021). Tumor Microenvironment Remodeling-Based Penetration Strategies to Amplify Nanodrug Accessibility to Tumor Parenchyma. *Advanced Drug Delivery Reviews*. <https://doi.org/10.1016/j.addr.2021.02.019>
- Magesh, V., Vijeya Singh, J. P., Selvendiran, K., Ekambaram, G., & Sakthisekaran, D. (2006). Antitumour activity of crocetin in accordance to tumor incidence, antioxidant status, drug metabolizing enzymes and histopathological studies. *Molecular and Cellular Biochemistry*, 287(1–2), 127–135. <https://doi.org/10.1007/s11010-005-9088-0>
- Mahmoudi, M., Sant, S., Wang, B., Laurent, S., & Sen, T. (2011). Superparamagnetic iron oxide nanoparticles (SPIONs): Development, surface modification and applications in chemotherapy. *Advanced Drug Delivery Reviews*, 63(1–2), 24–46. <https://doi.org/10.1016/j.addr.2010.05.006>
- Majidi, S., Sehrig, F. Z., Farkhani, S. M., Goloujeh, M. S., & Akbarzadeh, A. (2016). Current methods for synthesis of magnetic nanoparticles. *Artificial Cells, Nanomedicine and Biotechnology*, 44(2), 722–734. <https://doi.org/10.3109/21691401.2014.982802>
- Maltas, E., Malkondu, S., Uyar, P., & Ozmen, M. (2015). Fluorescent labelling of DNA on superparamagnetic nanoparticles by a perylene bisimide derivative for cell imaging. *Materials Science & Engineering C*, 48, 86–93. <https://doi.org/10.1016/j.msec.2014.11.057>
- Maluccio, M., & Covey, A. (2012). Recent Progress in Understanding , Diagnosing , and Treating Hepatocellular Carcinoma. *Cancer Journal for Clinicians*, 62(6), 394–399. <https://doi.org/10.3322/caac.21161>.
- Massaro, S., & Lorenzoni, G. (2021). Nanomedicine : a socio-technical system. *Technological Forecasting & Social Change*, 173(July), 121066. <https://doi.org/10.1016/j.techfore.2021.121066>
- Mei, L., Zhang, Z., Zhao, L., Huang, L., Yang, X. L., Tang, J., & Feng, S. S. (2013). Pharmaceutical nanotechnology for oral delivery of anticancer drugs. *Advanced Drug Delivery Reviews*, 65(6), 880–890. <https://doi.org/10.1016/j.addr.2012.11.005>

- Meijer, E., Kromhout, H., & Heederik, D. (2001). Respiratory effects of exposure to low levels of concrete dust containing crystalline silica. *American Journal of Industrial Medicine*, 40(2), 133–140. <https://doi.org/10.1002/ajim.1080>
- Melnyk, J. P., Wang, S., & Marcone, M. F. (2010). Chemical and biological properties of the world's most expensive spice: Saffron. *Food Research International*, 43(8), 1981–1989. <https://doi.org/10.1016/j.foodres.2010.07.033>
- Mir, M. A., Ganai, S. A., Mansoor, S., Jan, S., Mani, P., Masoodi, K. Z., Amin, H., Rehman, M. U., & Ahmad, P. (2020). Isolation, purification and characterization of naturally derived Crocetin beta-D-glucosyl ester from *Crocus sativus* L. against breast cancer and its binding chemistry with ER-alpha/HDAC2. *Saudi Journal of Biological Sciences*, 27(3), 975–984. <https://doi.org/10.1016/j.sjbs.2020.01.018>
- Molina, M. M., Seabra, A. B., Oliveira, M. G. De, Itri, R., & Haddad, P. S. (2013). Nitric oxide donor superparamagnetic iron oxide nanoparticles. *Materials Science & Engineering C*, 33(2), 746–751. <https://doi.org/10.1016/j.msec.2012.10.027>
- Moros, M., Hernáez, B., Garet, E., Dias, J. T., Sáez, B., Grazú, V., González-Fernández, Á., Alonso, C., & De La Fuente, J. M. (2012). Monosaccharides versus PEG-functionalized NPs: Influence in the cellular uptake. *ACS Nano*, 6(2), 1565–1577. <https://doi.org/10.1021/nn204543c>
- Nair, S. C., Panikkar, K. R., & Parthod, R. K. (1993). Protective effects of crocetin on the bladder toxicity induced by cyclophosphamide. *Cancer Biotherapy*, 8(4), 339–344. <https://doi.org/10.1089/cbr.1993.8.339>
- Nakamura, Y., Mochida, A., Choyke, P. L., & Kobayashi, H. (2016). Nanodrug Delivery: Is the Enhanced Permeability and Retention Effect Sufficient for Curing Cancer? *Bioconjugate Chemistry*, 27(10), 2225–2238. <https://doi.org/10.1021/acs.bioconjchem.6b00437>
- Nkurikiyimfura, I., Wang, Y., Safari, B., & Nshingabigwi, E. (2020). Temperature-dependent magnetic properties of magnetite nanoparticles synthesized via coprecipitation method. *Journal of Alloys and Compounds*, 846. <https://doi.org/10.1016/j.jallcom.2020.156344>
- Pang, Y. L., Lim, S., Ong, H. C., & Chong, W. T. (2016). Research progress on iron oxide-based magnetic materials: Synthesis techniques and photocatalytic applications. *Ceramics International*, 42(1), 9–34. <https://doi.org/10.1016/j.ceramint.2015.08.144>
- Park, Y. C., Smith, J. B., Pham, T., Whitaker, R. D., Sucato, C. A., Hamilton, J. A., Bartolak-Suki, E., & Wong, J. Y. (2014). Effect of PEG molecular weight on stability, T2 contrast, cytotoxicity, and cellular uptake of superparamagnetic iron oxide nanoparticles (SPIONs). *Colloids and Surfaces B: Biointerfaces*, 119, 106–114. <https://doi.org/10.1016/j.colsurfb.2014.04.027>

- Parvanian, S., Mostafavi, S. M., & Aghashiri, M. (2017). Multifunctional nanoparticle developments in cancer diagnosis and treatment. *Sensing and Bio-Sensing Research*, 13, 81–87. <https://doi.org/10.1016/j.sbsr.2016.08.002>
- Perry, S. C., Gateman, S. M., Stephens, L. I., Lacasse, R., Schulz, R., & Mauzeroll, J. (2019). Pourbaix Diagrams as a Simple Route to First Principles Corrosion Simulation. *Journal of The Electrochemical Society*, 166(11), C3186–C3192. <https://doi.org/10.1149/2.0111911jes>
- Premkumar, K., Thirunavukkarasu, C., Abraham, S. K., Santhiya, S. T., & Ramesh, A. (2006). Protective effect of saffron (*Crocus sativus* L.) aqueous extract against genetic damage induced by anti-tumor agents in mice. *Human and Experimental Toxicology*, 25(2), 79–84. <https://doi.org/10.1191/0960327106ht589oa>
- Qi, Y., Ye, J., Zhang, S., Tian, Q., Xu, N., Tian, P., & Ning, G. (2019). Controllable synthesis of transition metal ion-doped CeO₂ micro/nanostructures for improving photocatalytic performance. *Journal of Alloys and Compounds*, 782, 780–788. <https://doi.org/10.1016/j.jallcom.2018.12.111>
- Rahimi, M., Charmi, G., Matyjaszewski, K., Banquy, X., & Pietrasik, J. (2021). Recent developments in natural and synthetic polymeric drug delivery systems used for the treatment of osteoarthritis. *Acta Biomaterialia*, 123, 31–50. <https://doi.org/10.1016/j.actbio.2021.01.003>
- Ramimoghadam, D., Bagheri, S., & Hamid, S. B. A. (2014). Progress in electrochemical synthesis of magnetic iron oxide nanoparticles. *Journal of Magnetism and Magnetic Materials*, 368, 207–229. <https://doi.org/10.1016/j.jmmm.2014.05.015>
- Saleh, T. A. (2020). Nanomaterials: Classification, properties, and environmental toxicities. *Environmental Technology and Innovation*, 20, 101067. <https://doi.org/10.1016/j.eti.2020.101067>
- Samarghandian, S., & Borji, A. (2014). Anticarcinogenic effect of saffron (*Crocus sativus* L.) and its ingredients. *Pharmacognosy Research*, 6(2), 99–107. <https://doi.org/10.4103/0974-8490.128963>
- Samrot, A. V., Sahithya, C. S., Selvarani A, J., Purayil, S. K., & Ponnaiah, P. (2021). A review on synthesis, characterization and potential biological applications of superparamagnetic iron oxide nanoparticles. *Current Research in Green and Sustainable Chemistry*, 4(September 2020), 100042. <https://doi.org/10.1016/j.crgsc.2020.100042>
- Sanna, V., Pala, N., & Sechi, M. (2014). Targeted therapy using nanotechnology: Focus on cancer. *International Journal of Nanomedicine*, 9(1), 467–483. <https://doi.org/10.2147/IJN.S36654>
- Santos, M. C., Seabra, A. B., Pelegrino, M. T., & Haddad, P. S. (2016). Synthesis , characterization and cytotoxicity of glutathione- and PEG-glutathione-superparamagnetic iron oxide nanoparticles for nitric oxide delivery. *Applied Surface Science*, 367, 26–35. <https://doi.org/10.1016/j.apsusc.2016.01.039>

- Sarkar, T., Rawat, K., Bohidar, H. B., & Solanki, P. R. (2016). Electrochemical immunosensor based on PEG capped iron oxide nanoparticles. *Journal of Electroanalytical Chemistry*, 783, 208–216. <https://doi.org/10.1016/j.jelechem.2016.11.019>
- Sathishkumar, P., Li, Z., Govindan, R., Jayakumar, R., Wang, C., & Long Gu, F. (2021). Zinc oxide-quercetin nanocomposite as a smart nano-drug delivery system: Molecular-level interaction studies. *Applied Surface Science*, 536(September 2020), 147741. <https://doi.org/10.1016/j.apsusc.2020.147741>
- Sharma, R. (2020). *Descriptive epidemiology of incidence and mortality of primary liver cancer in 185 countries : evidence from GLOBOCAN 2018*. 00(00), 1–11. <https://doi.org/10.1093/jjco/hyaa130>
- Shende, P., & Gupta, H. (2020). Formulation and comparative characterization of nanoparticles of curcumin using natural , synthetic and semi-synthetic polymers for wound healing. *Life Sciences*, 253(December 2019), 117588. <https://doi.org/10.1016/j.lfs.2020.117588>
- Sodipo, B. K., & Aziz, A. A. (2016). Recent advances in synthesis and surface modification of superparamagnetic iron oxide nanoparticles with silica. *Journal of Magnetism and Magnetic Materials*, 416, 275–291. <https://doi.org/10.1016/j.jmmm.2016.05.019>
- Soltani, F., Ramezani, M., Amel Farzad, S., Mokhtarzadeh, A., & Hashemi, M. (2017). Comparison study of the effect of alkyl-modified and unmodified PAMAM and PPI dendrimers on solubility and antitumor activity of crocetin. *Artificial Cells, Nanomedicine and Biotechnology*, 45(7), 1356–1362. <https://doi.org/10.1080/21691401.2016.1236805>
- Sonju, J. J., Dahal, A., Singh, S. S., & Jois, S. D. (2021). Peptide-functionalized liposomes as therapeutic and diagnostic tools for cancer treatment. *Journal of Controlled Release*, 329(September 2020), 624–644. <https://doi.org/10.1016/j.jconrel.2020.09.055>
- Stephen, Z. R., Kievit, F. M., & Zhang, M. (2011). Magnetite nanoparticles for medical MR imaging. *Materials Today*, 14(7–8), 330–338. [https://doi.org/10.1016/S1369-7021\(11\)70163-8](https://doi.org/10.1016/S1369-7021(11)70163-8)
- Sun, M., Zhu, A., Zhang, Q., & Liu, Q. (2014). A facile strategy to synthesize monodisperse superparamagnetic OA-modified Fe₃O₄ nanoparticles with PEG assistant. *Journal of Magnetism and Magnetic Materials*, 369, 49–54. <https://doi.org/10.1016/j.jmmm.2014.06.013>
- Sung, H., Ferlay, J., Siegel, R. L., Laversanne, M., Soerjomataram, I., Jemal, A., & Bray, F. (2021). Global cancer statistics 2020: GLOBOCAN estimates of incidence and mortality worldwide for 36 cancers in 185 countries. *CA: A Cancer Journal for Clinicians*, 0(0), 1–41. <https://doi.org/10.3322/caac.21660>
- Takami, S., Sato, T., Mousavand, T., Ohara, S., Umetsu, M., & Adschiri, T. (2007). Hydrothermal synthesis of surface-modified iron oxide nanoparticles. *Materials Letters*, 61(26), 4769–4772. <https://doi.org/10.1016/j.matlet.2007.03.024>

- Teja, A. S., & Koh, P. Y. (2009). Synthesis, properties, and applications of magnetic iron oxide nanoparticles. *Progress in Crystal Growth and Characterization of Materials*, 55(1–2), 22–45. <https://doi.org/10.1016/j.pcrysgrow.2008.08.003>
- Tonbul, H., Sahin, A., Tavukcuoglu, E., Ultav, G., Akbas, S., Aktas, Y., Esendagli, G., & Capan, Y. (2021). Folic Acid Decoration of Mesoporous Silica Nanoparticles to Increase Cellular Uptake and Cytotoxic Activity of Doxorubicin in Human Breast Cancer Cells. *Journal of Drug Delivery Science and Technology*, 102535. <https://doi.org/10.1016/j.jddst.2021.102535>
- Trabulo, S., Aires, A., Aicher, A., Heeschen, C., & Cortajarena, A. L. (2017). Multifunctionalized iron oxide nanoparticles for selective targeting of pancreatic cancer cells. *Biochimica et Biophysica Acta - General Subjects*, 1861(6), 1597–1605. <https://doi.org/10.1016/j.bbagen.2017.01.035>
- Tseng, T. H., Chu, C. Y., Huang, J. M., Shiow, S. J., & Wang, C. J. (1995). Crocetin protects against oxidative damage in rat primary hepatocytes. *Cancer Letters*, 97(1), 61–67. [https://doi.org/10.1016/0304-3835\(95\)03964-X](https://doi.org/10.1016/0304-3835(95)03964-X)
- Virlan, M. J. R., Miricescu, D., Radulescu, R., Sabliov, C. M., Totan, A., Calenic, B., & Greabu, M. (2016). Organic nanomaterials and their applications in the treatment of oral diseases. *Molecules*, 21(2), 1–23. <https://doi.org/10.3390/molecules21020207>
- Wongwailikhit, K., & Horwongsakul, S. (2011). The preparation of iron (III) oxide nanoparticles using W / O microemulsion. *Materials Letters*, 65(17–18), 2820–2822. <https://doi.org/10.1016/j.matlet.2011.05.063>
- Wu, Wei, Quanguo He, and C. J. (2008). Magnetic Iron Oxide Nanoparticles Synthesis and Surface Functionalization Strategies. *Nanoscale Research Letters*, 3(11), 397–415.
- Wu, T., & Dai, Y. (2017). Tumor microenvironment and therapeutic response. *Cancer Letters*, 387, 61–68. <https://doi.org/10.1016/j.canlet.2016.01.043>
- Yallapu, M. M., Foy, S. P., Jain, T. K., & Labhasetwar, V. (2010). PEG-functionalized magnetic nanoparticles for drug delivery and magnetic resonance imaging applications. *Pharmaceutical Research*, 27(11), 2283–2295. <https://doi.org/10.1007/s11095-010-0260-1>
- Yang, M., Li, J., Gu, P., & Fan, X. (2021). The application of nanoparticles in cancer immunotherapy: Targeting tumor microenvironment. *Bioactive Materials*, 6(7), 1973–1987. <https://doi.org/10.1016/j.bioactmat.2020.12.010>
- Yousefi, E., Eskandari, A., Gharavi, M., & Khademvatan, S. (2014). In vitro activity and Cytotoxicity of Crocus sativus Extract against Leishmania Major (MRHO/IR/75/ER). *Infectious Disorders - Drug Targets*, 14(1), 56–60. <https://doi.org/10.2174/1871526514666140827101901>
- Zhang, G., Liao, Y., & Baker, I. (2010). Surface engineering of core/shell iron/iron oxide nanoparticles from microemulsions for hyperthermia. *Materials Science and Engineering C*, 30(1), 92–97. <https://doi.org/10.1016/j.msec.2009.09.003>

- Zhao, H., Saatchi, K., & Ha, U. O. (2009). Preparation of biodegradable magnetic microspheres with poly (lactic acid) -coated magnetite. *Journal of Magnetism and Magnetic Materials*, 321, 1356–1363.
<https://doi.org/10.1016/j.jmmm.2009.02.038>
- Zhong, Y. J., Shi, F., Zheng, X. L., Wang, Q., Yang, L., Sun, H., He, F., Zhang, L., Lin, Y., Qin, Y., Liao, L. C., & Wang, X. (2011). Crocetin induces cytotoxicity and enhances vincristine-induced cancer cell death via p53-dependent and -independent mechanisms. *Acta Pharmacologica Sinica*, 32(12), 1529–1536.
<https://doi.org/10.1038/aps.2011.109>

